

1-1-2008

## Magnetohydrodynamics in microchannels and adhesion properties of nanoporous alumina films

Hussameddine Kabbani  
*University of Nevada, Las Vegas*

Follow this and additional works at: <https://digitalscholarship.unlv.edu/rtds>

---

### Repository Citation

Kabbani, Hussameddine, "Magnetohydrodynamics in microchannels and adhesion properties of nanoporous alumina films" (2008). *UNLV Retrospective Theses & Dissertations*. 2844.  
<http://dx.doi.org/10.25669/ao5k-rxd1>

This Dissertation is protected by copyright and/or related rights. It has been brought to you by Digital Scholarship@UNLV with permission from the rights-holder(s). You are free to use this Dissertation in any way that is permitted by the copyright and related rights legislation that applies to your use. For other uses you need to obtain permission from the rights-holder(s) directly, unless additional rights are indicated by a Creative Commons license in the record and/or on the work itself.

This Dissertation has been accepted for inclusion in UNLV Retrospective Theses & Dissertations by an authorized administrator of Digital Scholarship@UNLV. For more information, please contact [digitalscholarship@unlv.edu](mailto:digitalscholarship@unlv.edu).

MAGNETOHYDRODYNAMICS IN MICROCHANNELS AND  
ADHESION PROPERTIES OF NANOPOROUS  
ALUMINA FILMS

by

Hussameddine Kabbani

Masters of Science  
American University of Beirut, Lebanon  
May 2005

A dissertation submitted in partial fulfillment  
of the requirements for the

**Doctor of Philosophy in Mechanical Engineering**  
**Department of Mechanical Engineering**  
**Howard R. Hughes College of Engineering**

**Graduate College**  
**University of Nevada, Las Vegas**  
**December 2008**

UMI Number: 3352176

## INFORMATION TO USERS

The quality of this reproduction is dependent upon the quality of the copy submitted. Broken or indistinct print, colored or poor quality illustrations and photographs, print bleed-through, substandard margins, and improper alignment can adversely affect reproduction.

In the unlikely event that the author did not send a complete manuscript and there are missing pages, these will be noted. Also, if unauthorized copyright material had to be removed, a note will indicate the deletion.

**UMI**<sup>®</sup>

---

UMI Microform 3352176

Copyright 2009 by ProQuest LLC.

All rights reserved. This microform edition is protected against unauthorized copying under Title 17, United States Code.

ProQuest LLC  
789 E. Eisenhower Parkway  
PO Box 1346  
Ann Arbor, MI 48106-1346



**Dissertation Approval**  
The Graduate College  
University of Nevada, Las Vegas

August 20, 2008

The Dissertation prepared by

Hussameddine Kabbani

Entitled

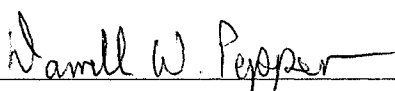
Magnetohydrodynamics in Microchannels and Adhesion Properties of  
Nanoporous Alumina Films

is approved in partial fulfillment of the requirements for the degree of

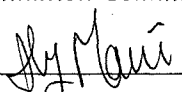
Doctor of Philosophy in Mechanical Engineering

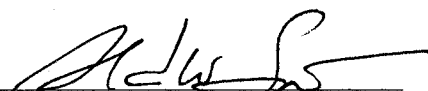
  
Examination Committee Co-Chair

  
Examination Committee Chair

  
Examination Committee Member

  
Examination Committee Member

  
Graduate College Faculty Representative

  
Dean of the Graduate College

## ABSTRACT

### **Magnetohydrodynamics in Microchannels and Adhesion Properties of Nanoporous Alumina Films**

by

Hussameddine Kabbani

Dr. Brendan O'Toole, Examination Committee Chair  
Assistant Professor of Mechanical Engineering  
University of Nevada Las Vegas

and

Dr. Biswajit Das, Examination Committee Chair  
Professor of Electrical Engineering  
University of Nevada Las Vegas

In the first part of this dissertation, RedOx-based magnetohydrodynamic (MHD) flows in three-dimensional (3D) microfluidic channels are investigated theoretically with a coupled mathematical model consisting of the Nernst-Planck equations for the concentrations of ionic species, the local electroneutrality condition of the electric potential, and the Navier-Stokes equations for the flow field. The induced currents and flow rates in 3D planar channels are compared with the experimental data obtained from the literature and those obtained from the previous two-dimensional mathematical model. Then a new approximate closed form solution for the velocity profile of steady incompressible MHD flows in a rectangular micro-channel is proposed. It can be used to optimize the dimensions of the channel and to determine the magnitudes and polarities of the prescribed currents in MHD networks so as to achieve the desired flow patterns and flow rates.

In the second part of the dissertation, the adhesive properties of thin nanoporous alumina templates are investigated. Such templates are important in fabricating an array of nanopores that will be used in the “Lab on a Chip” technology

## TABLE OF CONTENTS

ABSTRACT.....	iii
LIST OF FIGURES .....	vii
LIST OF TABLES .....	ix
ACKNOWLEDGEMENTS .....	x
CHAPTER 1 INTRODUCTION.....	1
1.1 Background.....	1
1.2 Dissertation Structure.....	13
CHAPTER 2 MODELING REDOX-BASED MHD in 3D CHANNELS.....	14
2.1 Introduction.....	14
2.2 Mathematical Model.....	16
2.2.1 Mathematical Model for the Fluid Motion .....	18
2.2.2 The Model for Multi-Ion Mass Transport.....	19
2.3 Solver Validation and Mesh Choice .....	22
2.4 Results and Discussions.....	23
CHAPTER 3 ANALYSIS OF MHD MICROPUMPS AND NETWORKS.....	43
3.1 Introduction.....	43
3.2 Mathematical Model .....	44
3.2.1 The Mathematical Model for the Fluid Motion in DC MHD .....	46
3.2.2 The Mathematical Model for the Fluid Motion in AC MHD .....	50
3.3 Results and Discussion .....	51
3.3.1 Validation of the Closed Form Solution with DC MHD .....	52
3.3.2 Validation of the Closed Form Solution with AC MHD .....	63
CHAPTER 4 ADHESION PROPERTIES OF NANOPOROUS ALUMINA FILMS ..	68
4.1 Abstract.....	68
4.2 Introduction.....	69
4.3 Preliminary Work.....	71
4.4 Experimental Procedure.....	73
4.5 Scratch Test Procedure .....	77
4.6 Results and Discussion .....	78
CHAPTER 5 CONCLUSIONS AND OUTLOOK.....	93
5.1 Conclusions.....	94
5.2 Outlook .....	96

BIBLIOGRAPHY .....	98
VITA .....	113



## LIST OF FIGURES

Figure 1.1	The velocity profile of MHD flows in microchannels .....	3
Figure 1.2	The interaction between the magnetic field and induced current.....	4
Figure 1.3	Alumina thin film after anodiation.....	10
Figure 2.1	Schematic of a 3D straight microconduit .....	17
Figure 2.2	The resulting current as function of applied potential difference.....	25
Figure 2.3	The average velocity as functions of height and channel.....	29
Figure 2.4	The flow rate as a function of the height of the channel .....	30
Figure 2.5	The average velocity as function of applied potential difference.....	31
Figure 2.6	The maximum velocity as a function of the current.....	33
Figure 2.7	The average velocity as a function of the current.....	34
Figure 2.8	The flow rate as a function of the width of the channel .....	35
Figure 2.9	The resulting current as a function of applied potential difference.....	36
Figure 2.10	The average velocity as a function of the resulting current.....	37
Figure 2.11	The limiting current as a function of the concentration .....	38
Figure 2.12	The average velocity as a function of the concentration .....	39
Figure 2.13	The limiting current as a function of the magnetic flux density.....	40
Figure 2.14	The average velocity as a function of the magnetic flux density .....	42
Figure 3.1	Schematic diagram of the apparatus.....	45
Figure 3.2	The average velocity as a function of the channel width .....	53
Figure 3.3	The average velocity within the channel as a function of current.....	54
Figure 3.4	A schematic diagram of the network used in Bau's paper .....	55
Figure 3.5	The equivalent network of Bau's channel .....	56
Figure 3.6	A schematic diagram of the micro loop used by Affani et al .....	58
Figure 3.7	Comparison between the pressure of the micro loop .....	59
Figure 3.8	The mean velocity as a function of the channels height.....	60
Figure 3.9	The mean velocity as a function of the channels height and width.....	61
Figure 3.10	The mean velocity as a function of current and pressure drop.....	62
Figure 3.11	Comparison with Lemoff's work .....	64
Figure 3.12	The mean velocity as a function of the phase angle .....	65
Figure 3.13	The time averaged velocity as function of phase angle and current.....	66
Figure 3.14	The time averaged velocity as function of angle and pressure.....	67
Figure 4.1	Alumina thin film after anodization .....	70
Figure 4.2	The PSIA XE100 system.....	72
Figure 4.3	A cracked substrate sample .....	73
Figure 4.4	The anodization setup used .....	74
Figure 4.5	The anodization apparatus used.....	75
Figure 4.6	The power supply used.....	76
Figure 4.7	The potential difference across the electrodes.....	79
Figure 4.8	The principle behind the testing apparatus.....	80

Figure 4.9	The first sample adhesive test results .....	82
Figure 4.10	The second sample adhesive test results .....	83
Figure 4.11	The third sample adhesive test results .....	84
Figure 4.12	The fourth sample adhesive test results.....	85
Figure 4.13	The fifth sample adhesive test results.....	86
Figure 4.14	The sixth sample adhesive test results.....	87
Figure 4.15	The seventh sample adhesive test results .....	88
Figure 4.16	The eighth sample adhesive test results.....	89
Figure 4.17	The ninth sample adhesive test results .....	90

## LIST OF TABLES

Table 1.1	Comparison between MHD and other pumping techniques.....	5
Table 1.2	The advantages and disadvantages of DC and AC MHD.....	6
Table 1.3	Properties considered while fabricating LOC and their advantages.....	8
Table 1.4	The advantages and disadvantages of AAO as LOC fabricating material ....	10
Table 1.5	Comparison between MA and HA processes .....	11
Table 3.1	Comparison between the experimental results done by Bau and our closed form solution.....	57
Table 4.1	The nine different scenarios to be studied .....	80
Table 4.2	The ultimate force corresponding to different scenarios .....	82

## ACKNOWLEDGEMENTS

I would sincerely thank Dr. Shizhi Qian who helped me a lot throughout my studies. He was my formal advisor and work supervisor before his resignation. He was really supportive to me. He has guided me throughout much of this work. I have learnt a lot from him such as hard working, dedication, and enjoying what I am doing. He was more than an older brother to me. It was a pleasure for me working with him. Also, I would like to thank Dr. Brendan O'toole who accepted to be my committee chair one week before my defense. He helped me a lot in this short period of time. Also, I would like to thank Dr. Biswajit Das my advisor and committee co-chair for his support and guidance. I would like to thank Dr. Darrell Pepper, Dr. William Culbreth, and Dr. Aly Said for serving as my dissertation committee. Special thanks go to my family, specially my mom, Fariha Al-Laham Kabbani, who has supported me emotionally throughout all the difficulties I faced during my course of work. Also, I like to thank Mr. Shaher Al-Laham, my cousin and close friend, who supported me throughout my studies and the bad times I have faced. He was really a man of honor. Special thanks for Mrs. Joan Conway, our department secretary, who helped me a lot during my studies.

## CHAPTER 1

### INTRODUCTION

#### 1.1 Background

Biological applications in engineering are becoming an interesting field of study for different research groups. The applications vary from circulating blood samples, testing biological samples, and detecting the presence of DNA and RNA chains (Jensen, 1999; Legally et al., 2001; Yang et al., 2002; Yamamoto et al., 2002; Prinz et al., 2002; Galanina et al., 2003; Carlo et al., 2003; Verpoorte, 2002; and Huikko et al., 2003).

To perform such operations a new technology has flourished. This technology is called Lab-on-a-Chip (LOC). LOC can handle many procedures done in real labs such as filtering, mixing, and separating. Such processes have been investigated recently by Boedicker et al. (2008) who designed and fabricated a novel LOC to detect bacteria and Terao et al. (2008) who tested a LOC device to detect single chromosomal DNA.

LOC is composed from a network of micro or nano channels, so minute samples such as blood and saliva won't be diluted. Based on this fact, the design process for LOC faces two challenges: creating circulation within the channel and fabricating it in order to withstand huge forces.

Micro and nano channels need huge pumping force due to the fact that body forces increase rigorously at small dimensions. To overcome the pumping problem, many groups imposed, studied, and designed different methods to create flows within the channel.

Nittis et al. (2001) designed and fabricated a pressure gradient micropump. This pump depends on the pressure gradient developed between the inlet and outlet of the channel. This method was expensive and unreliable.

The idea of using electrokinetic forces to pump the fluid in minute channels has been recently investigated. There are two important methods to pump the fluid using electrokinetic means: electroosmosis and electrophoresis.

In electroosmotic flow, the flow is basically initiated by the formation of an electric double layer between the surface of the conduit and the electrolyte solution within. Usually, the surface of the conduit is charged. Ions will migrate from the electrolyte solution towards the oppositely charged wall. By applying a potential difference across the inlet and outlet of the conduit, the ions will flow to the oppositely charged electrode and transfer this motion to the inner layers of the fluid by shear forces and thus creating a flow.

In electrophoretic flow, charged particles are attracted to oppositely charged electrodes. Their motion drags fluid layers, thus, creating a flow. Many groups used electrokinetics to utilize a flow within the microchannel (Jacobson et al., 1994; Burns et al., 1998; Anderson et al., 2003; Weigl et al., 2003; and Qian et al., 2006). It was proved that this method needs high potential field to operate and gives relatively low flow rates.

RedOx magnetohydrodynamics (MHD) is becoming one of the most important means to pump fluid in microchannels since it is highly reliable, doesn't need any external moving parts, and works under low voltages (Lee et al., 2000; Bau et al., 2000; Bau et al., 2002; Ghaddar et al., 2002; West et al., 2002; Ghaddar et al., 2003; and Eijkel et al., 2004).

RedOx MHD is a technique that depends basically on creating a propulsive Lorentz force within the fluid itself (Henry et al., 1999; Reyes et al., 2002; and Haswell et al., 2003). This force will balance the pressure gradient and the viscous forces within the channel. The velocity profile in RedOx MHD flows is parabolic based on the assumptions that the flow is fully developed, steady state, and the fluid is incompressible. Figure 1.1 shows the velocity profile for RedOx MHD flow within a microchannel.

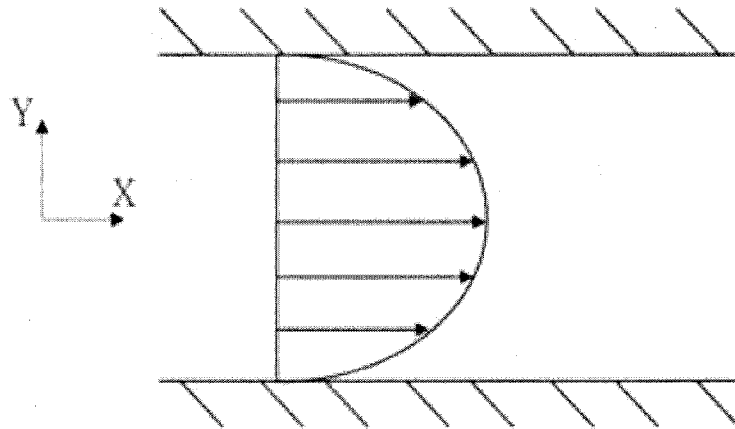


Figure 1.1: The velocity profile of MHD flows in microchannels.

A pair of electrodes must be installed on the opposite walls of the micro conduit to create a Lorentz force. Those electrodes are connected to an electric potential field.

Current flow will be originated between the two electrodes. This flow should be maintained by the presence of electrolyte solution. The interaction between the current flow and magnetic field will create a force that is perpendicular to both vectors. Figure 1.2 shows the interaction between the magnetic field and the induced current. Applying the right hand rule, the flow direction will be deduced.

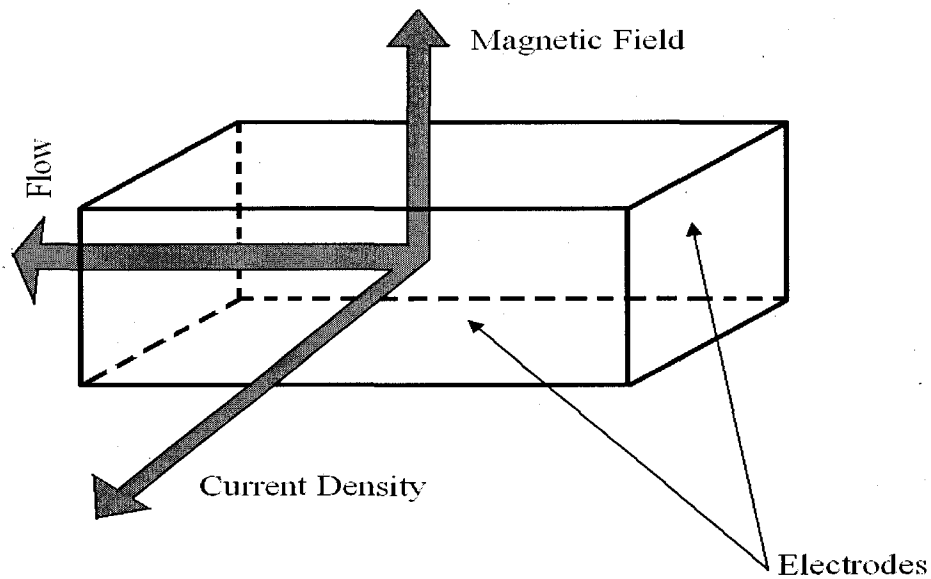


Figure 1.2: The interaction between the magnetic field and the induced current.

Pumping fluids using RedOx MHD has unique advantages: it is an inexpensive technique, it needs low potential field, it doesn't need any moving parts, it pumps high mass flow rates, it is reliable, it consumes less power, and the flow can be controlled easily (Qian et al., 2005; Homsy et al., 2005; and Anderson et al., 2006).

There are two draw backs for RedOx MHD flows. One of them is that, when high voltages are applied, the current will increase. As current increases in the presence of



ions, electrolysis process will start, and thus bubbles will be created and the flow will be retarded (Leventis et al., 2002)

Secondly, the electrodes have short life span, so they must be replaced occasionally (Qian et al., 2005). Table 1.1 shows the comparison between MHD and other pumping methods.

Table 1.1: Comparison between MHD and other pumping techniques

MHD	Other Pumping Means
1- Inexpensive	1- Relatively Expensive
2- Operate under low voltages	2- Needs high voltages
3- The flow can be controlled easily	3- The flow is difficult to controlled, also, loop circulation is impossible to be obtained
4- Easy to design	4- Many constraints that will affect the design

Many researchers were able to construct and develop micropumps that work with the principle of MHD. Jang et al. (2000) fabricated a micropump that works under low voltages. Lemoff et al. (2000) fabricated a sensor that is used to control the RedOx MHD pumping process. RedOx MHD micropumps could operate under either direct-current (DC) or alternating-current (AC). Table 1.2 shows the difference between both methods.

Table 1.2: The advantages and disadvantages of DC and AC MHD

Method	Advantages	Disadvantages
DC MHD	1- Low power Consumption 2- Inexpensive 3-Flow can be controlled easily	1- Short Electrode Life 2- Bubble Generation
AC MHD	1- Long electrode life 2- No bubble generation	1-Induction of eddy currents

In addition to fabrication, many groups tried to present a mathematical model for RedOx MHD flow in microchannels (Bau et al., 2001; Bau et al., 2003; Glesson et al., 2004; and Qian et al., 2005).

They considered the model as a 2D model and they were able to solve it numerically. The model consists of solving the Navier Stoke equation and the Nernst Planck equation.

In this work, the 2D RedOx MHD model is taken one step further by considering the full 3D model. The effect of the different physical variables contributing in this

model will be studied and analyzed. The inter relationship between those variables are mentioned and discussed. Then a closed form solution that will aid in the MHD LOC designing process will be derived and validated.

The previous mentioned work was conducted on micro channels. When the study and experimentation were performed on nano channels, it was found out that nano channels were not able to withstand the force created by MHD means. Also, it was found out that there is no published method to create a single nanopore. So, in the second part of this dissertation, light will be shed on the material selection to fabricate the LOC in nano channels.

The material should have special mechanical, electrical, and chemical properties (Kikutani et al., 2002; Hulme et al., 2002; Wang et al., 2004; Chen et al., 2004; and Wu et al., 2004). Table 1.3 states the vital properties to be considered for the selection of the LOC fabrication material.

Many groups have considered different materials to manufacture channels in LOC. Hofmann et al. (2001) used polydimethylsiloxine to fabricate a 3D sheath flow channel. He was able to have a device that resists corrosion with a sheath to sample flow rate ratio of 20 but the channel was not able to resist strong forces.

Jeong et al. (2001) used an insulated silicon substrate to fabricate channels. Although this substrate was able to operate under high temperature, silicon is a bad conductor of electricity and has poor electric properties.

Tuomikoski et al. (2002) took advantage of the good properties of the silicon substrate and ionized the substrate before manufacturing the device. This development enhanced the electrical properties of the substrate.

Table 1.3: Properties considered while fabricating LOC and their advantages

Type of Property	Property of the fabricating Material	Field of Application
Electrical	Dielectric	Electroosmotic Flow
	Uniformly distributed Charge	Diffuso electroosmotic flow
	Good Conductor	Magnetohydrodynamics
Chemical	Anti-corrosive	With fluids containing highly oxidizing agents
	Doesn't react with acids	In applications where acids are encountered
	Resists Chemical Reactions	In applications where multi-phase ions are encountered
Temperature	Must operate under variable temperatures	DNA detection and synthesis
Mechanical	Highly adhesive	In applications with large pumping forces
	Resists Fatigue	In applications that require high reliability
	High tensile strength	Overcoming large forces and pressure gradient developed across the walls of the channel

Yamamoto et al. (2002) used polydimethylsiloxane glass as a substrate and added a temperature control sensor. This device has very good electrical properties such as conductivity. Khademhosseini et al. (2004) fabricated channels using a polyethylene glycol microstructure. This device had a high reliability and life span due to the fact that polyethylene glycol can resist corrosion, but it was not able to withstand relatively high velocities.

Recently, many groups are using anodized alumina substrates to manufacture channels and nanopores ( Zhu et al., 2005; Garcia-Vergara et al., 2006; Cheng et al., 2006; Lee et al., 2007; Lee et al., 2008). The advantage of anodized alumina substrate over any other fabricating material is that it can resist corrosion and suitable for applications where the fluid has either basic or acidic properties. In addition, alumina substrates are good conductors of electricity so it is suitable for MHD and electrokinetic flows.

One of the important things to investigate is the mechanical properties of anodized alumina substrates. The anodization process, which is affected by variables such as the type of acid used and the current applied, can greatly affect the mechanical properties of the substrate under study. Table 1.4 shows the advantages and disadvantages of anodized alumina substrate.

Table 1.4: The advantages and disadvantages of anodized alumina substrate

Advantages	Disadvantages
1- Can be easily electrically charged	1- Design Limitations (Fluid volumetric flow rate)
2- Inexpensive to fabricate	
3- High reliability	
4- Anti-corrosion	2- Many variables in the anodization process that must be controlled
5- Can operate under various temperatures	
6- High life span	
7- Can resist stresses	

When aluminum substrate is oxidized under constant potential difference, the surface of the aluminum layer will be covered by a fine nanoporous oxide layer. Figure 1.3 shows the alumina substrate after anodization.

### Nanoporous Alumina Thin Film

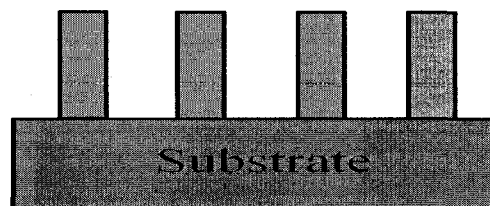


Figure 1.3: Alumina thin film after anodiation

There are two methods used in anodizing nanoporous alumina substrate. One of them is mild anodization (MA). This process is slow, expensive, and difficult to build (Li et al., 1998; Nicewarner-Pena et al., 2001; and Lee et al., 2002). The second one is hard anodization (HA). This process is relatively fast compared to MA (Lichtenberger-Bajza et al., 1960; and Csokan et al., 1962). The HA process is performed under certain conditions: low temperature (chillers to cool the acid must be used), high potential difference, and the usage of special acids (Murphy et al., 1961; Takahashi et al., 1973; Furneaux et al., 1989; and Li et al., 2006). The difference between MA and HA is stated in Table 1.5.

Table.1.5: Comparison between (MA) and the Hard Anodization (HA)

Method	Advantage	Disadvantage
Mild Anodization	1- Self-ordered nanopores 2- Smaller nanopore size 3- Lower temperatures	1- Very Slow Process 2- Low Reliability 3- Thinner Substrates
Hard Anodization	1- Fast Process 2- High Reliability 3- Inexpensive	1- Bigger Nanopores 2- Disordered nanopores

To improve the mechanical properties of AAO nanopores, a new technique has been implemented. It was found that changing the applied potential and the acid used will change the distribution and dimensions of the nanopores. Changing those two variables will lead to a change in the mechanical properties of the substrate. Changing the mechanical property of any substrate will change the classification of each sample and its area of application (Parkhutik et al., 1992; Ostrowski et al., 1999; Xia et al., 2004; Habazaki et al., 2004; Zhu et al., 2005; Gras et al., 2006; and Garcia-Vergara et al., 2007).

The anodization apparatus is easy and inexpensive to build. An alumina sample must be placed on the anode and a platinum substrate is placed in the cathode. Both electrodes are depicted in a beaker filled with acid. The electrodes are connected to a power supply: the voltage applied varies from 30V to 120V based on the acid used. The acid must be maintained at room temperature so a chiller must be installed. The chiller will aid in cooling the acid within the apparatus by convection means (Jessenky et al., 1998; Haruyama et al., 2001; Zhou et al., 2001; and Choi et al., 2003).

The current produced will etch the outer surface of the alumina substrate thus revealing the nanopores. The increase in timing will allow producing uniformly distributed nanopores with fine pore diameter. As time increases, the current will start dissolving the inner parts of the alumina substrate thus the anodization process should be stopped. The anodization process has an effect on the adhesive properties of the channels and nanopores produced. It is interesting to investigate the effect of the anodization setup on the fabricated nanopores.



## 1.2 Dissertation Structure

This dissertation is divided into two parts: in the first part, the RedOx MHD flow in microconduits will be studied. The relationship between the different contributing parameters (chapter 2) contributing in this flow will be investigated also. Also, a closed form solution will be imposed. It will act as a designing tool that will facilitate the calculation of the mean flow velocity within the microchannel (chapter 3).

In the second part of the dissertation, a study on the adhesive properties of AAO nanopores is performed. The effect of changing the anodization setup on those properties will be further investigated (chapter 4).

In chapter 5, the conclusions will be drawn concerning our work and future plans will be proposed.

## CHAPTER 2

# IMPLEMENTATION OF A THREE DIMENSIONAL REDOX MAGNETOHYDRODYNAMICS MODEL IN MICROFLUIDIC CHANNELS

### 2.1 Introduction

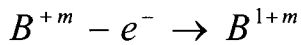
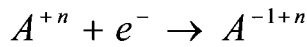
In this chapter, a model for RedOx MHD flows in 3D microchannel will be implemented and studied. As mentioned previously, Lorentz force is the pumping force in RedOx MHD flows. It is produced by the interaction between magnetic and electric fields.

Magnetic fields are produced by either permanent magnets (continual magnetic field) or electromagnets (magnetic field is produced by inductance due to current flow). The difference between both types of magnets is that in permanent magnets there is no heat produced while in electromagnets there is heat dissipated due to current flow. Another note to be considered is that usually the magnetic field produced by permanent magnets is stronger than that produced by electromagnets.

The electric field is produced by installing a pair of electrodes on the opposite walls of the microchannel under study. Those electrodes can be fabricated from good conducting material such as: gold sheets or aluminum sheets. This pair is connected to a power supply that can control the voltage and/or the current input. They can be either direct (time independent) or alternating (time dependent).

Since the current input and the polarity of the electrodes can be controlled, then the flow magnitude and direction can be controlled as well. For this reason, RedOx MHD is superior over all other flow means.

The term RedOx refers to the reduction and oxidation reaction that occurs on the opposite electrodes. As known, the fluid within the channel contains electrolyte ions. The current supplied by the electrodes will allow opposite ions to consume or release electrons. Usually the governing chemical equations are:



The first equation is the reduction equation whilst the second one is the oxidation reaction. The process of consuming and releasing electrons will enhance the current flow between the pair of electrodes.

The model consists of studying the flow within the channel: continuity equation and Navier-Stokes equations. The physical representation of the Lorentz force in the Navier Stoke equation is  $J \times B$ .  $B$  is the magnetic field magnitude and  $J$  is the faradic current density. This current depends on the electrolyte concentrations within the channel and it is found by solving the Nernst-Planck equation which consists of the migrative, diffusive, and conductive terms. As known, the conductive term depends on the velocity profile. Thus, it is clear that the model is coupled and can't be solved without the aid of commercial software. By applying the appropriate boundary conditions, this 3D model is solved. The power of such a model lies in the fact that it resembles the actual flow within any channel. This model will be validated by comparing it to experimental data obtained from the literature.

## 2.2 Mathematical Model

The numerical model of the problem presented above is divided into two main parts: the first one is solving for the velocity profile within the microchannel. This is done by considering the continuity and Navier-Stokes equation. The second one is solving for the faradic current within the microchannel which is done by considering the Nernst Planck (N-P) equation. N-P equation solves for the concentrations of both: electroactive species (those that goes through the RedOx reactions) and inert species (those that don't encounter RedOx reactions). In this work, the electroactive species are ferric and ferrous cyanide ions, while the inert species are potassium ions. It is important to mention here that the quasi-reversible RedOx reactions occur on the electrode surface.

This model was suggested with the help of Dr. Shizhi Qian. The schematic of this problem is extension from 2D to 3D of the model presented by Qian et al 2002. It consists of rectangular micro conduit whose length, width, and height are  $L$ ,  $W$ , and  $H$  respectively.

At this moment, the coordinate system to be used must be determined. It will be Cartesian with  $x$ ,  $y$ , and  $z$  acting as the principal axis. The origin will be located at one of the conduits corners. The dimensions of the conduit should satisfy the following relationship:  $0 \leq x \leq L$ ,  $0 \leq y \leq W$ , and  $0 \leq z \leq H$ .

To create a potential difference, a single pair of electrodes is deposited on one of the conduits opposite walls. The length of the electrode will be taken to be  $L_E$ . The distance from the origin to the edge of the electrode is  $L_I$  such that ( $L_I \leq x \leq L_I + L_E$ ,  $0 \leq z \leq H$ ,  $y=0$  and  $W$  respectively). It should be mentioned here that the walls of the conduit that are not covered by the electrodes, are considered to be dielectric. Figure 2.1 schematically

depicts the three-dimensional, straight, microconduit with electrodes deposited along the opposing walls. The conduit is filled with a dilute quasi-reversible RedOx electrolyte solution.

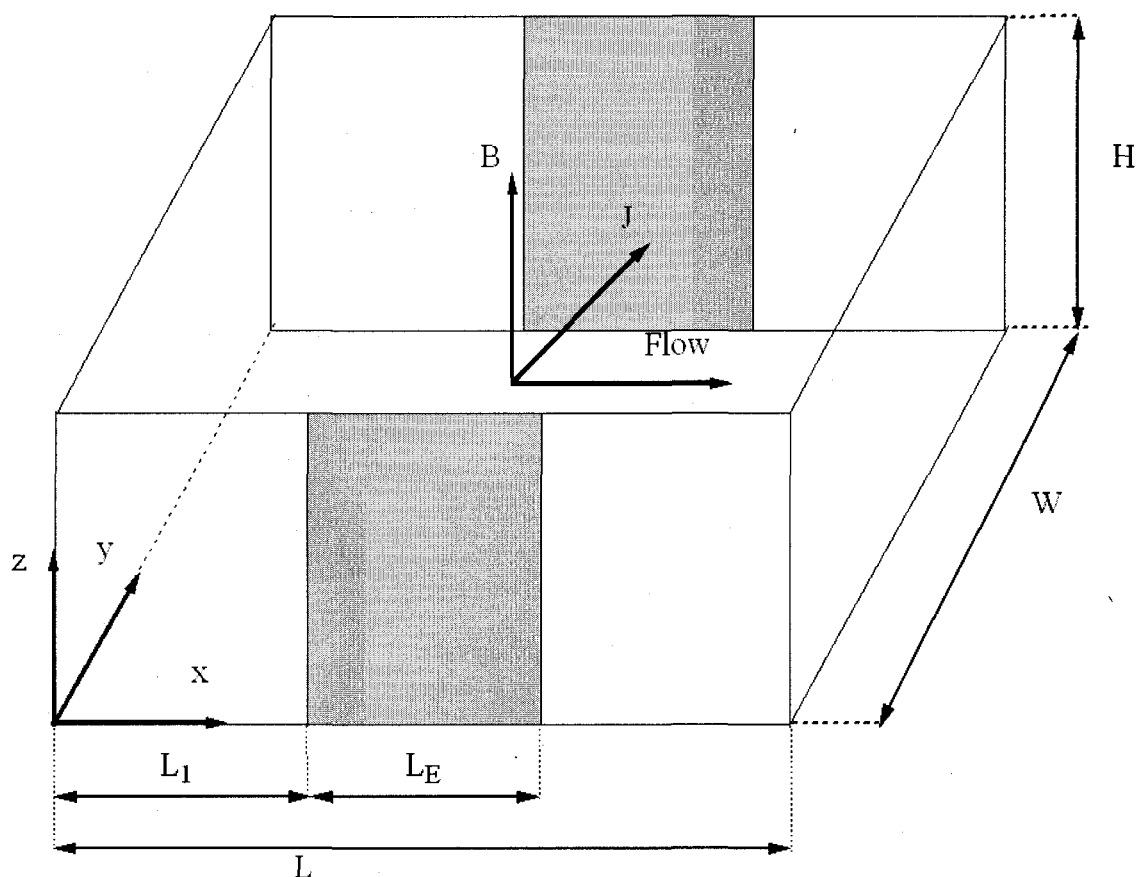


Figure 2.1: Schematics of a three-dimensional microconduit

As known, the imposed potential difference initiated and maintained by the electrodes deposited on the opposite walls of the micro conduit, will introduce an electric

current whose density is  $J$ . The conduit will be placed in a uniform magnetic field with a magnetic flux density  $\mathbf{B} = B\hat{\mathbf{e}}_z$  in the positive ( $z$ ) direction ( $\hat{\mathbf{e}}_z$  is a unit vector in the  $z$ -direction). The interaction between both the current density  $J$  and the magnetic field  $B$  will produce a Lorentz force  $\mathbf{J} \times \mathbf{B}$ .

### 2.2.1 The Mathematical Model for the Fluid Motion

The continuity and the Navier Stokes equation will shed light on the relationship between both the pressure gradient and the Lorentz force and the velocity field within the conduit:

$$\nabla \cdot \mathbf{u} = 0 \quad (1)$$

and

$$\rho \mathbf{u} \cdot \nabla \mathbf{u} = \mathbf{J} \times \mathbf{B} - \nabla p + \mu \nabla^2 \mathbf{u} \quad (2)$$

Equation (1) and (2) are based on the assumptions: i- The fluid is incompressible and ii- steady state flow.

In the above,  $p$  is the pressure;  $\rho$  and  $\mu$  denotes the liquid's density and viscosity respectively; and  $\mathbf{u} = u\hat{\mathbf{e}}_x + v\hat{\mathbf{e}}_y + w\hat{\mathbf{e}}_z$  is the fluid's velocity with  $u$ ,  $v$ , and  $w$  are the velocity components in the  $x$ -,  $y$ -, and  $z$ - directions respectively with unit vectors  $\hat{\mathbf{e}}_x$ ,  $\hat{\mathbf{e}}_y$ , and  $\hat{\mathbf{e}}_z$  respectively. The first term,  $\mathbf{J} \times \mathbf{B}$ , on the right hand side of equation (2) is the mathematical representation of the Lorentz force. In this work, three assumptions were taken: i- the natural convection induced by the density variations due to electrochemical reactions on the surfaces of electrodes does not play a major role (Qian et al 2006), ii- the paramagnetic forces due to the concentration gradients of paramagnetic species are

neglected (Ragsdale et al 1998), and finally iii- since the Reynolds number is very small the induced magnetic field is neglected (Qian et al 2006).

The boundary conditions that must be provided for the 3D model must satisfy the fact that the velocity at the surfaces of the conduit is zero, so it is no-slip boundary conditions. The boundary conditions used are mentioned below:

$$p(0, y, z) = P_1, \quad (3a)$$

$$\mathbf{t} \cdot \mathbf{u}(0, y, z) = 0, \quad (3b)$$

$$p(L, y, z) = P_2, \quad (3c)$$

In the above,  $\mathbf{t}$  is the unit vector tangent to the surface  $x = 0$  in (3b). The external pressure gradient is  $(P_1 - P_2)/L$ .

### 2.2.2 The Model for Multi-Ion Mass Transport

The most important thing to deal with in multi-ion mass transport is that the current flux at relatively high values is maintained. By doing this, the fluid flow will be maintained and the electrode corrosion and bubble formation will be avoided. To do so, a dilute quasi-reversible RedOx electrolyte solution is used. It was assumed that the RedOx electrolyte solution contains  $K$  dissolved ionic species ( $k=1, \dots, K$ ). The flux density of each dissolved ionic species due to convection, diffusion, and migration is given by:

$$\mathbf{N}_k = \mathbf{u} c_k - D_k \nabla c_k - z_k m_k F c_k \nabla V, \quad \text{with } k=1, \dots, K. \quad (4)$$

In the above,  $c_k$  is the molar concentration,  $D_k$  is the diffusion coefficient,  $z_k$  is the charge, and  $m_k$  is the electrical mobility of the  $k$ th ionic species.  $F$  is Faraday's constant ( $F=96484.6 \text{ C/mol}$ ), and  $V$  is the electric potential in the electrolyte solution. Based on

the order of magnitude analysis, the induction term  $\mathbf{u} \times \mathbf{B}$  is neglected in (4) (Qian et al 2006).

The mobility of species,  $m_k$ , is determined by the well known Nernst-Einstein relation. Equation (5) shows this relation:

$$m_k = \frac{D_k}{R T}. \quad (5)$$

Where  $D_k$  is the diffusion term,  $R$  is the universal gas constant, and  $T$  is the absolute temperature. The concentration of each species is governed by the mass conservation equation (Newmann 1991 and Bard 2000):

$$\nabla \cdot \mathbf{N}_k = 0, \quad k=1, \dots, K. \quad (6)$$

It is important to mention that there are no homogeneous reactions.

The set of equations (6) consist of  $K+1$  unknown variables: the concentrations of the  $K$  dissolved ionic species and the electric potential,  $V$ , in the electrolyte solution. The electroneutrality condition provides the  $(K+1)^{\text{th}}$  equation:

$$\sum_{k=1}^K z_k c_k = 0. \quad (7)$$

In equation (7), I neglected the electrical double layer next to the electrodes since the width of the microconduit is much larger than the thickness of the electrical double layer.

The current density  $\mathbf{J}$  in the electrolyte solution due to convection, diffusion, and migration is given by

$$\mathbf{J} = F \sum_{k=1}^K z_k \mathbf{N}_k. \quad (8)$$

The current density  $\mathbf{J}$  induces magnetic field  $\mathbf{b}$ . However, in most cases, the induced magnetic field  $\mathbf{b}$  can be neglected (Qian et al 2006).



The boundary condition for an inert species (no electrode reactions occur for that species) and for all species at insulated boundaries is

$$\mathbf{n} \cdot \mathbf{N}_k = 0, \quad (9)$$

where  $\mathbf{n}$  is the unit vector normal to the surface.

The concentrations of each species at the inlet cross-section ( $x=0$ ) are given by

$$c_k(0, y, z) = c_{k0}, \quad k=1, \dots, K, \quad (10a)$$

and obey the electroneutrality condition  $\sum_{k=1}^K z_k c_{k0} = 0$ .  $c_{k0}$  is determined from the bulk concentrations in the reservoir. Furthermore, far upstream of the electrodes, I assumed the electric field to be insignificant

$$\mathbf{n} \cdot \nabla V(0, y, z) = 0. \quad (10b)$$

The transport of species at the exit cross-section ( $x=L$ ) is dominated by convection due to sufficiently large Peclet numbers in the MHD flow (Qian et al 2006):

$$\mathbf{n} \cdot \mathbf{N}_k = \mathbf{n} \cdot (c_k \mathbf{u}), \quad k=1, \dots, K, \quad (10c)$$

and

$$\mathbf{n} \cdot \nabla V(L, y, z) = 0. \quad (10d)$$

For RedOx couple, the oxidation and reduction reactions occur, respectively, at the surfaces of the anode and cathode:



When the RedOx couple is  $\text{K}_4[\text{Fe}(\text{CN})_6]/\text{K}_3[\text{Fe}(\text{CN})_6]$  electrolyte solution, Ox and Red in the above electrochemical reaction correspond, respectively, to  $[\text{Fe}(\text{CN})_6]^{3-}$  and

$[\text{Fe}(\text{CN})_6]^{4-}$ , and  $n=1$  in (11). The Butler-Volmer equation describes the kinetics of the electrodes' reactions (Newman 1991 and Bard 2000):

$$\mathbf{n} \cdot \mathbf{N}_{\text{Red}} = -\mathbf{n} \cdot \mathbf{N}_{\text{Ox}} = k_0 \left( c_{\text{Ox}} e^{-\frac{\alpha n F}{RT} \eta} - c_{\text{Red}} e^{\frac{(1-\alpha) n F}{RT} \eta} \right), \quad (12)$$

where  $c_{\text{Ox}}$  and  $c_{\text{Red}}$  are the concentrations of the electroactive ions that are involved in the electrochemical reaction (11) at the edge of the electric double layer;  $\alpha$  is the charge transfer coefficient for the cathodic reaction, usually ranging from 0.0 to 1.0;  $n$  represents the number of electrons exchanged in the reaction;  $k_0$  is the reaction rate constant; and

$$\eta = \begin{cases} (U_{an} - V), & \text{along the surface of anode} \\ (U_{ca} - V), & \text{along the surface of cathode} \end{cases} \quad (13)$$

In the above,  $U_{an}$  and  $U_{ca}$  are, respectively, the imposed potential on the anode and cathode, and  $\Delta V = U_{an} - U_{ca}$  represents the potential difference applied to the opposing electrodes.

Witness that the momentum and mass transport equations are strongly coupled. The flow field affects the mass transport because of the convection term which affects the current density  $\mathbf{J}$ , which, in turn, affects the flow field through the Lorentz force  $\mathbf{J} \times \mathbf{B}$ . Therefore, one has to simultaneously solve the three-dimensional full mathematical model which consists of the continuity and Navier-Stokes equations (1)-(2), the mass conservation equations (6)-(7), and the generalized Butler-Volmer expression (12) for the MHD flow field, the ionic concentrations, and the current density.

### 2.3 Solver Validation and Mesh Choice

As previously mentioned, the model is strongly coupled. Thus, the commercial software COMSOL 3.3 was used. A 64 bit dual-processor workstation of 32 RAM was employed and this allowed me to create a finer mesh over the region under study. With a finer mesh, the results will be more reliable.

To validate the solver of this software, I used the paper published by Qian et al 2006. In this paper, two dimensional MHD flow with RedOx species analytical solution was deprived. The results of this solution and those predicted by COMSOL were in great agreement. Also, I compared those results with the results produced by FLUENT software and they were in good agreement as well.

The choice of the mesh to be used is so important so the results will be reliable. A non-uniform mesh with a larger number of elements next to the electrodes was used. This is because the boundary conditions are applied at the electrodes and the RedOx species are concentrated there. The mesh will be reduced in size as it approaches the middle of the conduit. To make sure that the mesh used is fine enough, I refined the mesh and compared it to the previous results produced by the previous mesh and I found out that there are 3% error in the readings and this made me confident about the mesh used.

### 2.4 Results and Discussions

First I simulated the RedOx-based MHD flow in a 3D planar microconduit of 18mm in length, 330  $\mu\text{m}$  in width, and 670  $\mu\text{m}$  in depth. The electrodes cover the entire side walls of the conduit (i.e.,  $L_I=0$ , and  $L_E=L$ ). The used RedOx electrolyte is a mixture of  $\text{K}_4[\text{Fe}(\text{CN})_6]/\text{K}_3[\text{Fe}(\text{CN})_6]$  in the absence of supporting electrolyte. The simulation

conditions are the same as those used in the experiments conducted by Aguilar et al. 2006. The electrolyte solution contains the three ions  $k^+$ ,  $Fe(CN)_6^{3-}$ , and  $Fe(CN)_6^{4-}$  with charges 1, -3, and -4, respectively. The diffusion coefficients at room temperature of  $k^+$ ,  $Fe(CN)_6^{3-}$ , and  $Fe(CN)_6^{4-}$  are, respectively,  $1.957 \times 10^{-9} m^2/s$ ,  $0.896 \times 10^{-9} m^2/s$ , and  $0.735 \times 10^{-9} m^2/s$  [36]. For the electrochemical reaction  $Fe(CN)_6^{3-} + e^- \Leftrightarrow Fe(CN)_6^{4-}$ , the reaction rate constant is  $k_0 \approx 1.0 \times 10^{-3} m/s$ , and the charge transfer coefficient is  $\alpha \approx 0.5$  (Bortels et al 1997). Since the Ferric cyanide and Ferrous cyanide system has a very high reaction rate constant, the results are not sensitive to values of  $k_0$  and  $\alpha$ . Since the RedOx electrolyte is dilute, the density and viscosity of the RedOx electrolyte are similar to those of water ( $\rho \sim 1000 kg/m^3$  and  $\mu \sim 10^{-3} Pa \cdot s$ ). In all my computations, the temperature  $T = 298K$ , and the inlet concentrations of the  $K_4[Fe(CN)_6]$  and  $K_3[Fe(CN)_6]$  are taken to be equal. I also assume that there is no pressure difference between the conduit's inlet and exit (i.e.,  $P_1 = P_2$ ).

The steady flow field and ionic concentration field under various potential differences ( $\Delta V$ ), RedOx species concentrations ( $C_0$ ), and magnetic flux densities ( $B$ ) are obtained by simultaneously solving the coupled full mathematical model described in section 2. Here I present the results of my numerical computations and compare them with the experimental data obtained by Aguilar et al. 2006. Fig 2.2 depicts the steady-state current transmitted through the electrolyte solution as a function of the imposed potential difference,  $\Delta V$ , across the electrodes in the absence (dashed line and circles) and presence (solid line and triangles) of magnetic field when the bulk concentrations of  $K_4[Fe(CN)_6]$  and  $K_3[Fe(CN)_6]$  are  $C_0 = 0.25M$ . In other words, the effect of magnetic field on the current is studied for two different magnetic flux densities, one at  $B = 0$  and

the other at  $B=0.44$  T under different potential differences. The circles ( $\bullet$ ) and triangles ( $\blacktriangle$ ) represent, respectively, the experimental data obtained from Aguilar et al. (2006) for  $B=0$  and  $B=0.44$  T, and the lines represent my theoretical predictions. The discrepancies between the theoretical predictions and the experimental data may be due to the differences between the actual and assumed diffusion coefficients of the electroactive species. When the applied potential difference is low, the resulting current nonlinearly increases with the applied potential difference. Once the potential difference exceeds a certain value, the current reaches the limiting current,  $I_{\text{limiting}}$ , and does not increase with the potential difference.

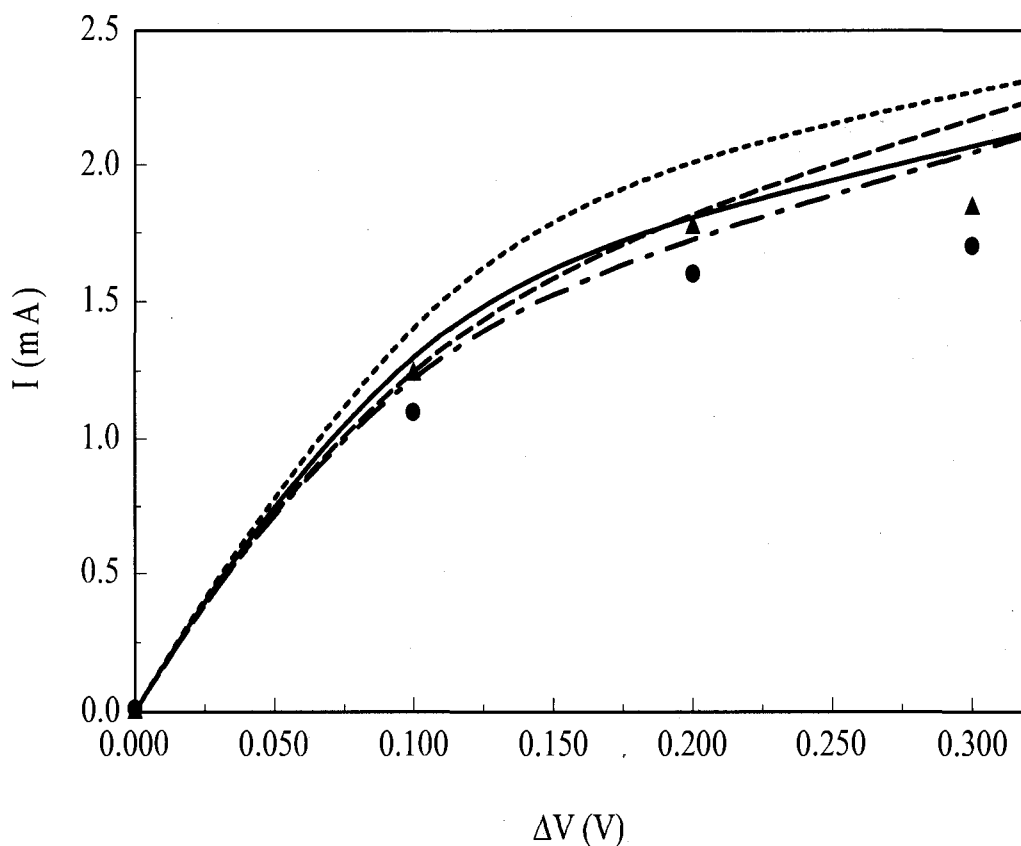


Figure 2.2: The resulting current as a function of the applied potential difference

The magnitude of the limiting current is, among other things, a function of the concentration of the RedOx species, the magnetic flux density, the dimensions of the electrodes and the conduit, and the diffusion coefficients of the electroactive species. In the presence of magnetic field, the interaction between the current density and magnetic field induces a Lorentz force which pumps the fluid from the reservoir located at the left end (i.e.,  $x=0$ ) to the reservoir positioned at the right end (i.e.,  $x=L$ ) of the channel. The induced fluid motion reduces the thickness of the concentration boundary layer formed next to the surfaces of the electrodes which, in turn, leads to an increase in the concentration gradient and current density along the surfaces of the electrodes. Consequently, the total current in the presence of the magnetic field is higher than that in the absence of magnetic field in which there is no fluid motion. But the effect of the magnetic field on the resulting current is not very significant under the above conditions.

In most regions of the planar microchannel, the current density  $\mathbf{J}$  is directed nearly normal to the electrodes' surfaces, and the Lorentz force  $\mathbf{J} \times \mathbf{B}$  is thus directed along the  $x$ -direction. Consequently, the velocity components in the  $y$ - and  $z$ -directions are at least two orders of magnitude lower than the velocity component in the  $x$ -direction. The  $x$ -component velocity is nearly independent of the coordinate  $x$ , and its profile looks like paraboloid (results are not shown here). Since the induced Lorentz force is a body force, the induced MHD flow is similar to a fully developed pressure-driven flow in a three-dimensional microchannel. The  $x$ -component velocity can be approximated with that of a fully developed duct flow with a rectangular section (White 2006):

$$u(y,z) = \frac{48\bar{U}}{\pi^3 \left[ 1 - \frac{192a}{\pi^5 b} \sum_{j=1,3,5,\dots}^{\infty} \frac{\tanh(j\pi b/2a)}{j^5} \right]} \sum_{i=1,3,5,\dots}^{\infty} (-1)^{\frac{i-1}{2}} \left[ \frac{\cosh\left(\frac{i\pi(z-b)}{2a}\right)}{\cosh\left(\frac{i\pi b}{2a}\right)} \right] \frac{\cos\left(\frac{i\pi(y-a)}{2a}\right)}{i^3}, \quad (13)$$

where  $a=W/2$ ,  $b=H/2$ , and  $\bar{U}$  is the average velocity. The series solution (13), which is not always practical for application, can be approximated with the following closed-form approximation with an error less than 1%:

$$u(y,z) = \bar{U} \left( \frac{m+1}{m} \right) \left( \frac{n+1}{n} \right) \left[ 1 - \left( \frac{|y-a|}{a} \right)^n \right] \left[ 1 - \left( \frac{|z-b|}{b} \right)^m \right]. \quad (14)$$

In the above,

$$m = 1.7 + 0.5 \left( \frac{b}{a} \right)^{-1.4} \quad \text{and} \quad n = \begin{cases} 2 & \text{for } \frac{b}{a} \leq \frac{1}{3} \\ 2 + 0.3 \left( \frac{b}{a} - \frac{1}{3} \right) & \text{for } \frac{b}{a} \geq \frac{1}{3} \end{cases}. \quad (15)$$

Subsequently, the steady  $x$ -component momentum equation can be approximated by:

$$-\frac{\partial p}{\partial x} + \mu \left( \frac{\partial^2 u}{\partial y^2} + \frac{\partial^2 u}{\partial z^2} \right) + J_y B = 0. \quad (16)$$

In the above,  $J_y$  is the  $y$ -component current density. The equation (16) represents a balance between the pressure force, the viscous force and the Lorentz force. Substituting (14) into (16), and taking volume integration of the equation (16), the average velocity becomes

$$\bar{U} = \frac{BIH - (P_2 - P_1)H^2}{4\mu L \left[ (n+1)\frac{H^2}{W^2} + (m+1) \right]}. \quad (17)$$

In the absence of the pressure difference between the conduit's inlet and exit (i.e.,  $P_1=P_2$ ), the average velocity is

$$\bar{U} = \frac{BIH}{4\mu L \left[ (n+1)\frac{H^2}{W^2} + (m+1) \right]}. \quad (18)$$

Using the predefined velocity profile (14), one can simplify the coupled full mathematical model without solving the continuity and Navier-Stokes equations. In the approximation model, one only needs to solve the mass transport equations (6)-(7) to determine the concentration field and the current density.

When the currents are predefined in the experiments, one can estimate the average velocity of the RedOx-based MHD flow with the close form approximation (18) which shows that the average velocity is linearly proportional to the magnetic flux density  $B$  and the current  $I$ , and is inversely proportional to the viscosity of the RedOx electrolyte. The average velocity also strongly depends on the dimensions of the conduit. Figure 2.3 depicts the average velocity as functions of the height and width of the conduit when its length  $L=18$  mm, the magnetic flux density  $B=0.44$  T, and the current  $I=0.15$  mA. When the channel is very shallow, the average velocity increases with the width of the channel. This, however, is not true for a wider channel. Once the width exceeds a certain value, the average velocity peaks and then declines with the increase of the width. For a deep channel, the average velocity increases with the width of the channel.



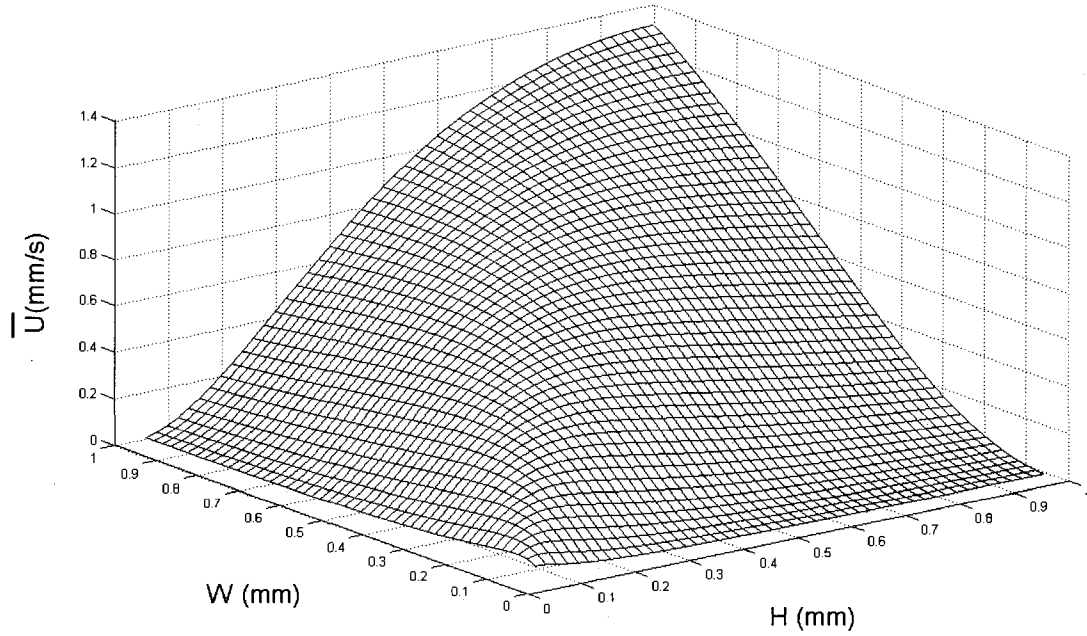


Figure 2.3: The average velocity as functions of the height and width of the microconduit

When the area of the  $yz$  cross-section and the total volume of the channel are fixed, there are optimal values for the height and width of the channel which corresponds to the maximum flow rate. The optimal height of the channel is governed by the solution of the equation,  $1.5H^6/A^3 + 5.7H^4/A^2 - 1.9A^{1.4}/H^{2.8} - 2.7 = 0$  in which  $A$  is the area of the  $yz$  cross-section of the channel. Figure 2.4 depicts the flow rate,  $Q = \bar{U}WH$ , as a function of the height of the channel when the area of the  $yz$  cross-section is  $0.2211 \text{ mm}^2$ , and other conditions are the same as those in Fig.2.3. The predefined cross-sectional area is the same as that of the channel used in the experiments by Aguilar et al. 2006. When the channel is shallow, the flow rate increases as the height increases. When the height of the channel is larger than a threshold value, the flow rate reaches the maximum and then

declines with the height. The maximum flow rate occurs in a channel with 410  $\mu\text{m}$  in height and 539.3  $\mu\text{m}$  in width under the above conditions.

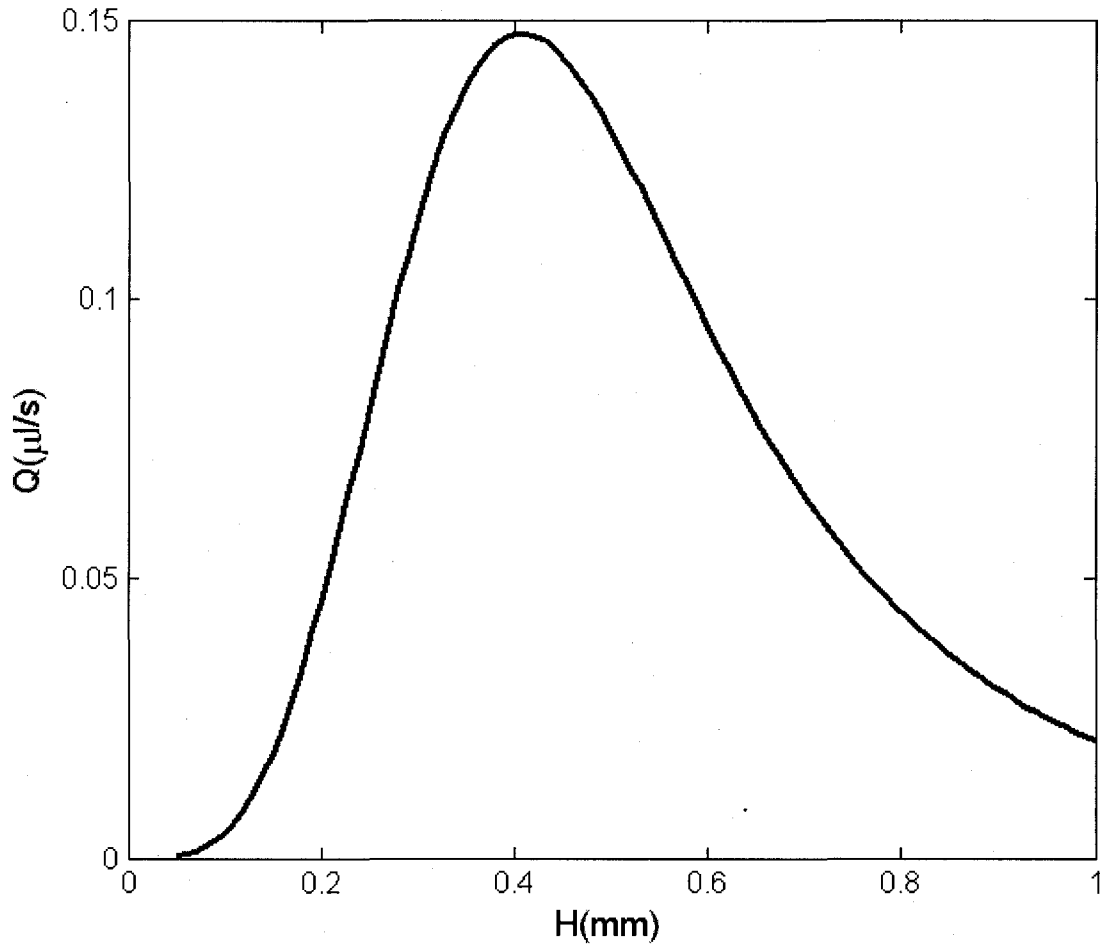


Figure 2.4: The flow rate as a function of the height of the microconduit

Figure 2.5 depicts the average velocity,  $\bar{U}$ , as a function of the applied potential difference for various bulk concentrations of the RedOx electrolyte when  $B=0.44$  T. The triangles ( $\blacktriangle$ ) and circles ( $\bullet$ ) represent the experimental data obtained from Aguilar et al. 2006, for the RedOx concentrations  $C_0=0.1$  M and  $C_0=0.25$  M, respectively.

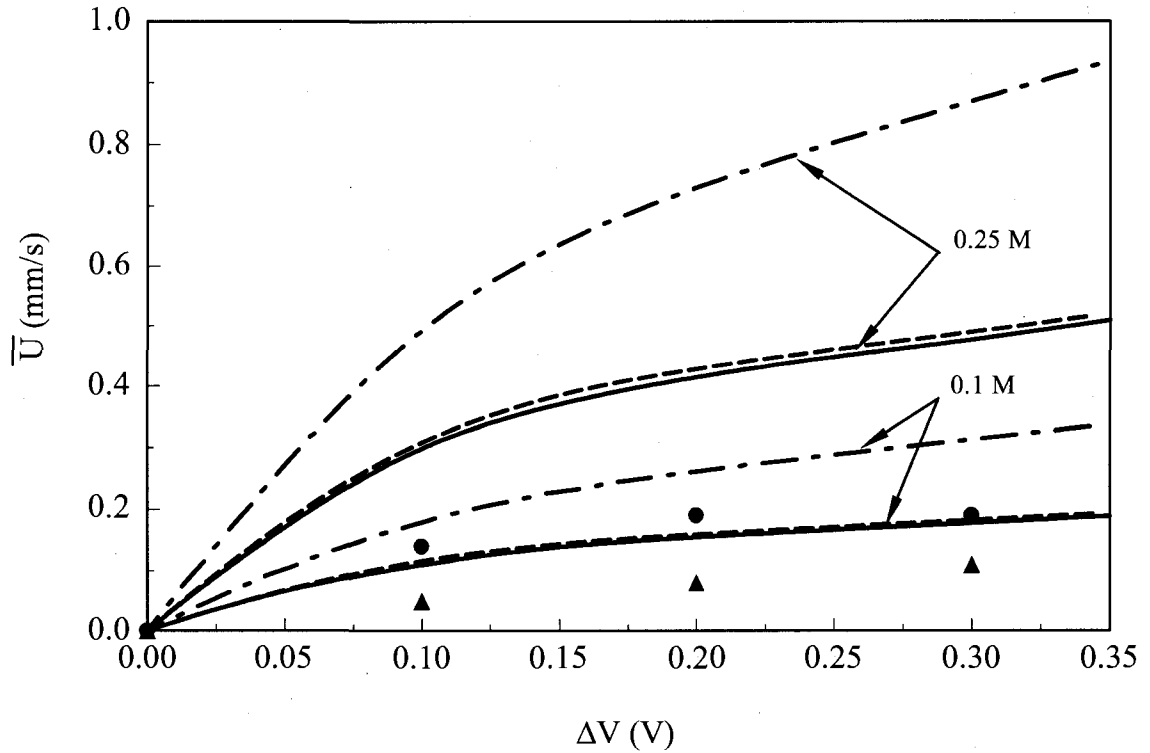


Figure 2.5: The average velocity as a function of the applied potential difference

The solid and dashed lines in Figure 2.5 represent, respectively, the predictions obtained from the full mathematical model described in section 2 and the approximation model using the velocity profile (14). The predictions obtained from the full mathematical model (solid line) and from the approximation model (dashed line) are in good agreement. The average velocity nonlinearly increases with the potential difference when the latter is relatively low. When the potential difference exceeds a critical value, the average velocity appears to be nearly independent of the potential difference. This behavior is attributed to the variations of the current as the potential difference increases (Fig.2.2) since the average velocity is proportional to the current as shown in the closed-form approximation (18). In order to maximize the flow rate, it is desirable to apply a

potential difference close to the critical value. The critical value in the RedOx-based MHD device is far below the threshold value for water electrolysis; therefore, there is no bubble formation in the RedOx-based MHD device even under DC electric field. The predictions obtained from the full mathematical model and from the approximation model are over predicting the experimental data. The experiments were conducted by tracing a dye placed on one end of the channel (i.e.,  $x=0$ ) which then was observed on the other end of the channel (i.e.,  $x=L$ ) after certain time interval  $\Delta t$ . The average velocity is estimated as the ratio  $L/\Delta t$ . I would suspect that the measured velocity would appear to be slower than they really are because the dye can be seen on the exit reservoir only when its concentration got high enough.

Figure 2.6 depicts the maximum velocity,  $U_{\max}$ , as a function of the current for  $C_0=0.1$  M (dashed line and circles) and 0.25 M (solid line and triangles) Nitrobenzene (NB) species in a planar conduit of 18 mm in length, 270  $\mu\text{m}$  in width, and 640  $\mu\text{m}$  in height. The magnetic flux density  $B= 0.41$  T. Using the measured currents from the experiments, I estimated the average velocity,  $\bar{U}$ , with the closed-form approximation (18). According to (14), the maximum velocity is  $U_{\max} = \frac{(m+1)(n+1)}{m n} \bar{U}$ . The lines and symbols in Fig.2.6 represent, respectively, the predictions of the closed-form approximation and the experimental data obtained from Arumugam et al. 2006.

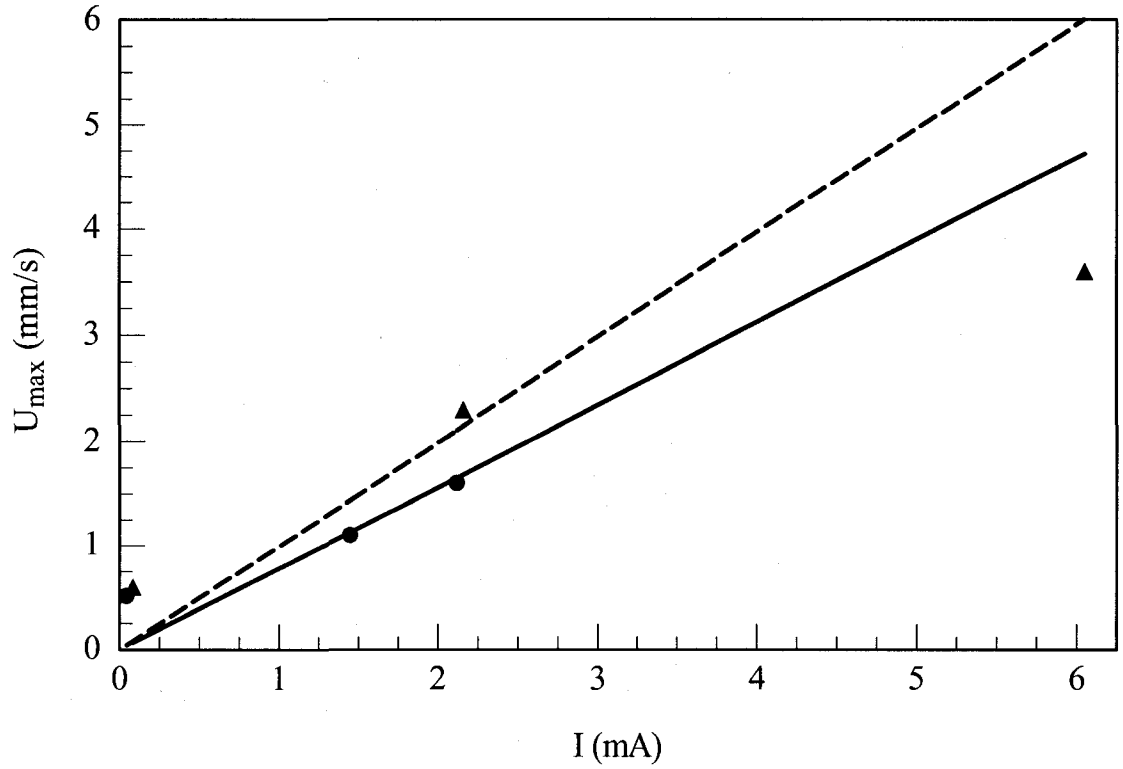


Figure 2.6: The maximum velocity as a function of the current

The predictions agree with the experimental observations. The deviation between the solid and dashed lines is basically due to the difference in the dynamic viscosities of 0.1 M and 0.25 M NB RedOx electrolyte. The dynamic viscosities for  $C_0=0.1$  M and 0.25 M NB electrolyte are, respectively, 0.00038 Pa·s and 0.00043 Pa·s (Arumugam et al 2006), which explains the slope for  $C_0=0.25$  M NB is smaller than that of  $C_0=0.1$  M NB electrolyte. Figure 2.7 depicts the average velocity as a function of the current for a saline solution when  $B=0.02$  T,  $L=80$  mm,  $W=2.88$  mm, and  $H=7$  mm. The line and symbols in Fig.7 represent, respectively, the prediction of the closed-form approximation and the experimental data obtained from Ho 2006.

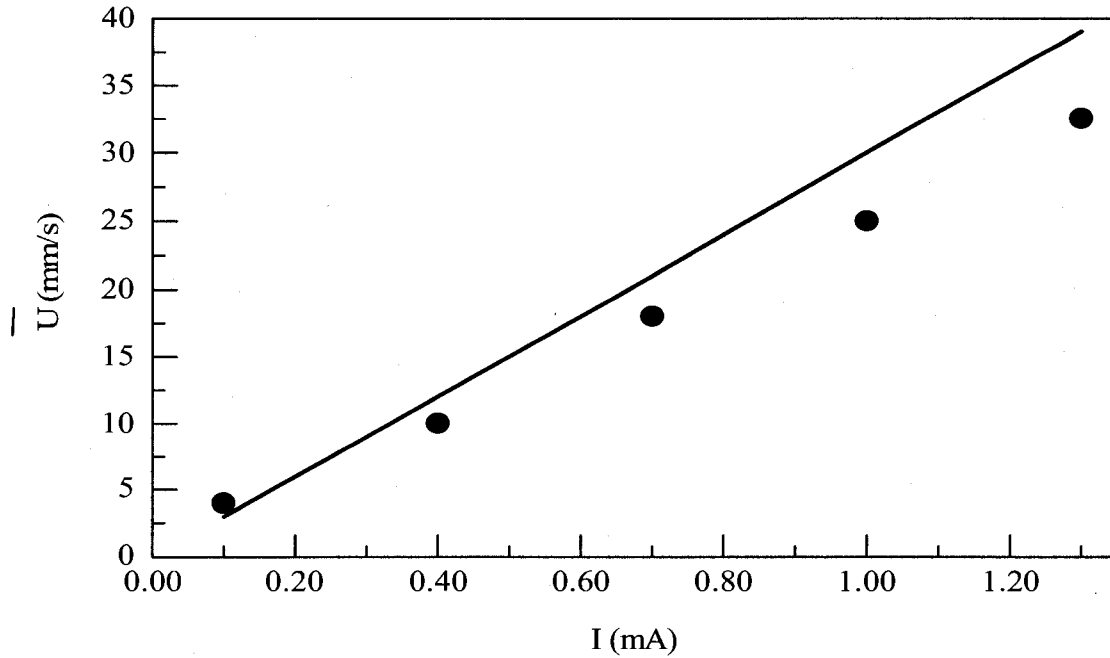


Figure 2.7: The average velocity as a function of the current

The predictions from my closed-form approximation favorably agree with the experimental data when the current is low. The deviation between the prediction and the experimental data increases as the current increases. In the experiments, since there is no RedOx species present in the solution, there were significant bubble formations under the high current conditions. The formed bubbles slow down the flow motion which explains my predictions are higher than the experimental data when the current is high. Figure 2.8 depicts the flow rate as a function of the width of the channel for a saline solution when  $B=0.02$  T,  $L=80$  mm,  $H=7$  mm, and the current  $I=0.7$  A. The line and symbols represent, respectively, the predictions of the closed-form approximation and the experimental data obtained from Ho 2006, and they are in agreement.

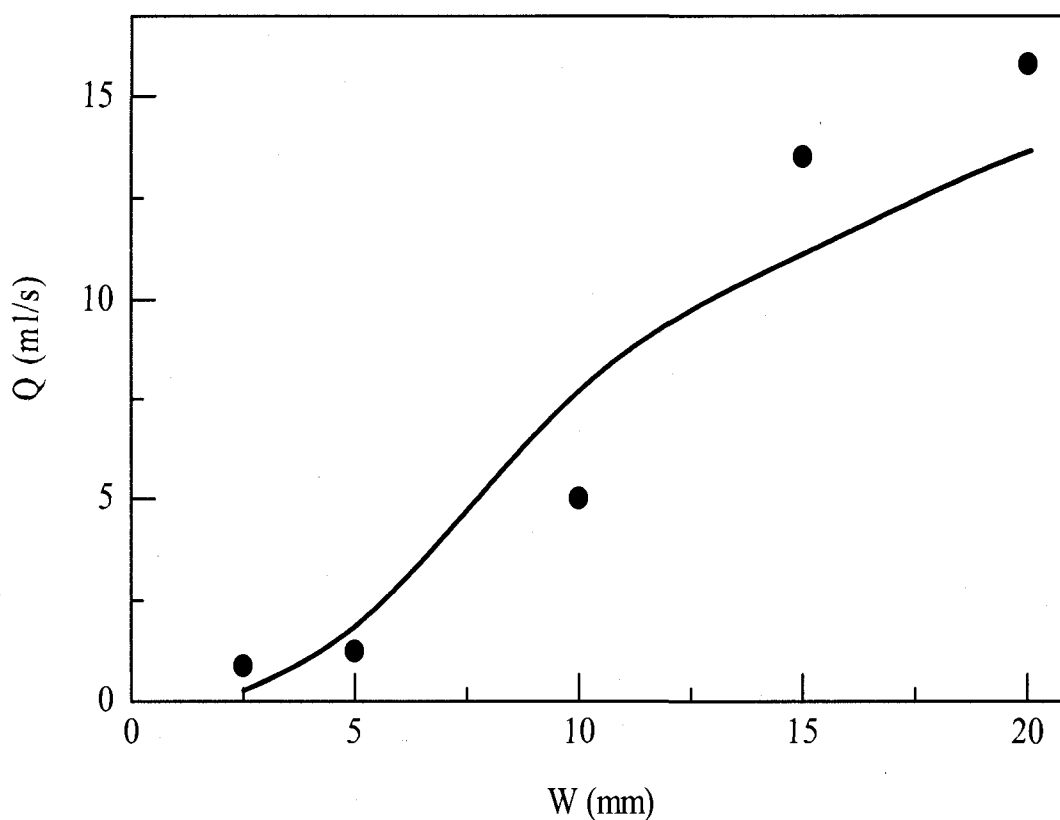


Figure 2.8: The flow rate as a function of the width of the channel

Figure 2.9 depicts the resulting current as a function of the applied potential difference across the two opposing electrodes for concentrations  $C_0=0.05$  M, 0.1 M, and 0.25 M of the RedOx species  $K_4[Fe(CN)_6]$  and  $K_3[Fe(CN)_6]$ . The lines and symbols represent, respectively, the solutions of the full mathematical model and the approximation model using the predefined velocity profile (14) without solving the continuity and Navier-Stokes equations. The other conditions are the same as those in Fig.2. The results from both models are in good agreement which makes us more confident in applying the approximation model. The resulting current increases as the bulk concentration of the RedOx species increases.

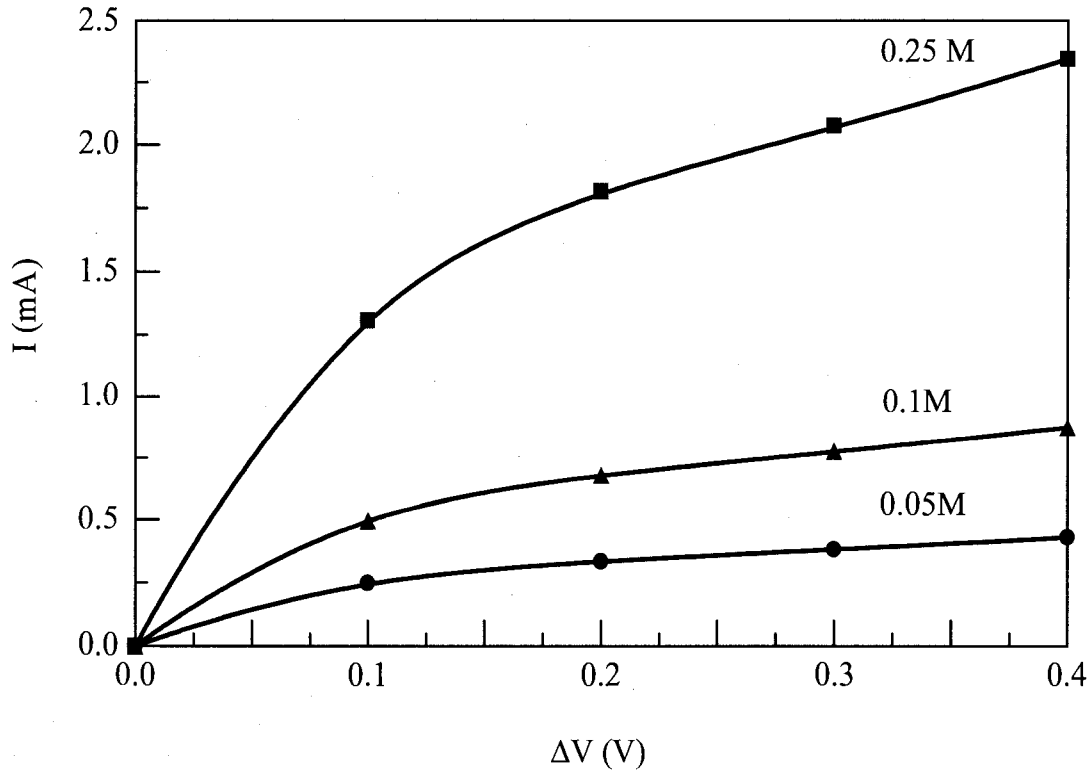


Figure 2.9: The resulting current as a function of the applied potential difference

Figure 2.10 depicts the average velocity,  $\bar{U}$ , as a function of the resulting current for various concentrations of the RedOx species. The symbols ( $\diamond$ ), ( $\blacktriangle$ ), and ( $\bullet$ ) represent the predictions of the full mathematical model for the concentrations  $C_0=0.05$  M, 0.1 M, and 0.25 M of the RedOx species  $K_4[Fe(CN)_6]$  and  $K_3[Fe(CN)_6]$ , respectively. Other conditions are the same as those in Fig. 2.9. The solid line in Fig.10 represents the prediction obtained from the closed-form approximation (18). It is clearly shown that  $\bar{U}$  is linearly proportional to the current  $I$  for various concentrations of the RedOx species. The predictions obtained from the full mathematical model (symbols in Fig.10) favorably agree with those obtained from the closed-form approximation. Therefore, one can use



the closed-form expression (18) to estimate the average velocity as long as the current is known.

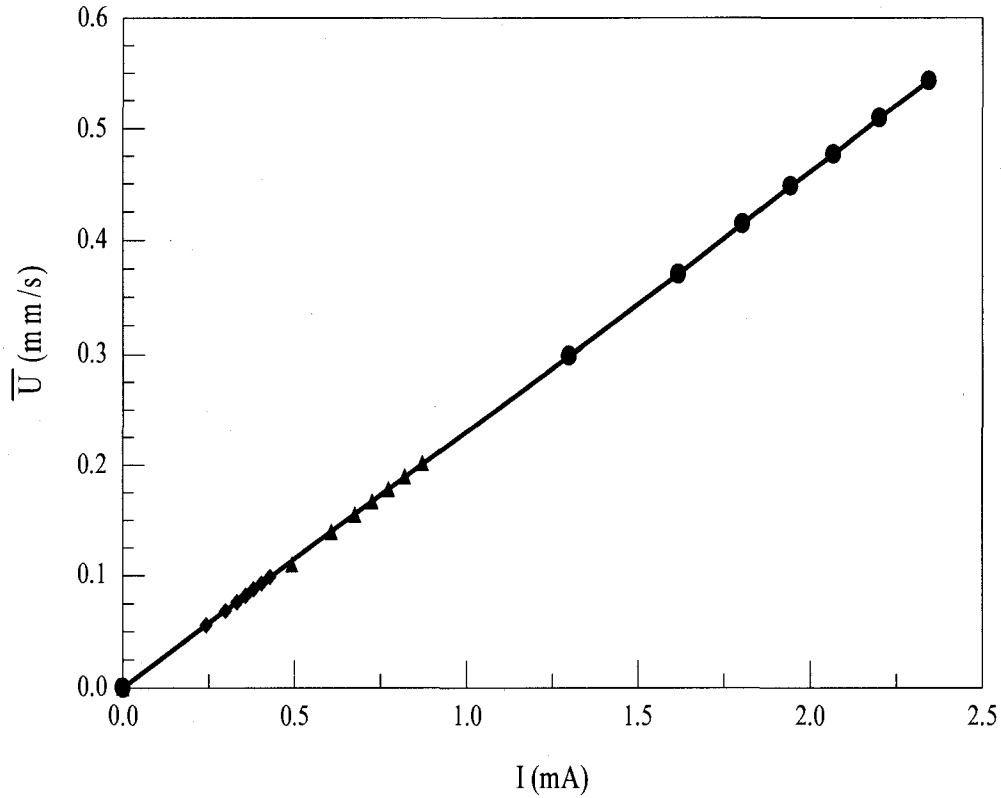


Figure 2.10: The average velocity as a function of the resulting current

Since the average velocity or flow rate is proportional to the resulting current, the average velocity or flow rate reaches the maximum for the limiting current. Figure 2.11 depicts the limiting current,  $I_{limiting}$ , as a function of the concentration of the RedOx species  $K_4[Fe(CN)_6]$  and  $K_3[Fe(CN)_6]$  for various magnetic flux densities. The dimensions of the channel are the same as those in Fig. 2.2. The predictions are obtained from the full mathematical model. The dash-dotted, dotted, dashed, and solid lines represent, respectively,  $B=0.2$  T, 0.44 T, 0.6 T, and 0.8 T.

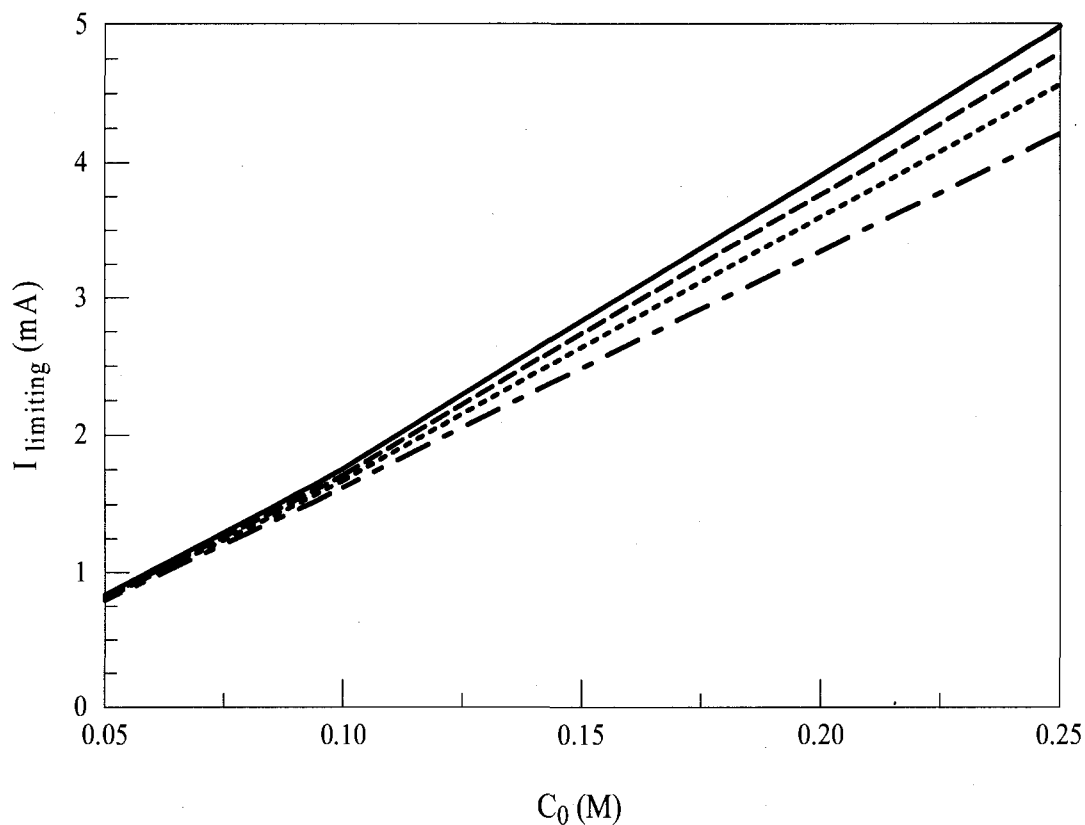


Figure 2.11: The limiting current as a function of the concentration of the RedOx species

The limiting current increases nearly linearly as the RedOx concentration increases for various magnetic flux densities. The linear relationship between the limiting current and the bulk concentration of the RedOx species agree with the experimental observations by Arumugam et al. 2006. Figure 2.12 depicts the maximum average velocity corresponding to the limiting current as a function of the bulk concentration of the RedOx species.

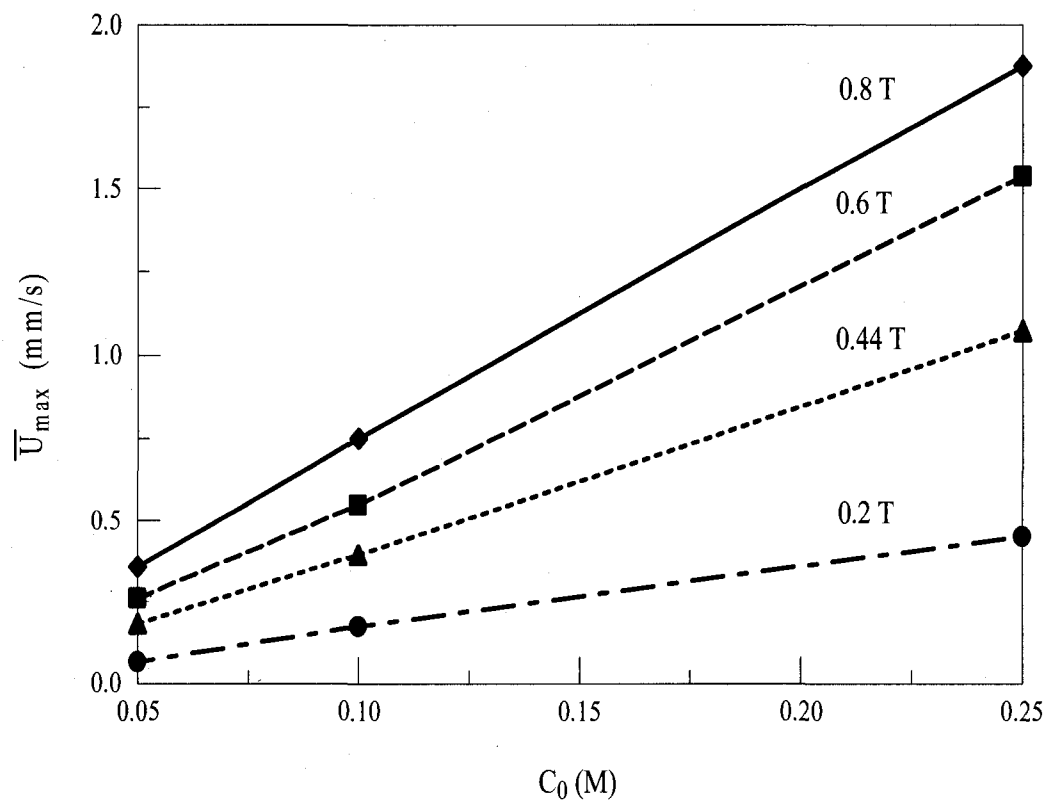


Figure 2.12: The average velocity as a function of the concentration of the RedOx species

The lines and symbols in Figure 2.12 represent, respectively, the predictions obtained from the full mathematical model and from the closed-form expression (18) using the obtained resulting current as depicted in Figure 2.11. Once again, the predictions from the closed-form approximation agree well with those obtained from the full mathematical model. Due to the linear relationship between the average velocity and the resulting current whose limiting value is linearly proportional to the bulk concentration of the RedOx species, the maximum average velocity,  $\bar{U}_{\max}$ , is also linearly proportional to the bulk concentration of the RedOx species present in the electrolyte solution. The results imply that one can enhance the flow by using higher concentration

of the RedOx species. However, the presence of concentrated RedOx species may damage some targets such as DNA and enzyme present in some biological applications.

Figure 2.13 depicts the limiting current as a function of the magnetic flux density for concentrations of the RedOx species  $C_0=0.05$  M (dotted line), 0.1 M (dashed line), and 0.25 M (solid line). When the concentration of the RedOx species is low, the limiting current is nearly independent of the magnetic flux density. As the concentration of the RedOx species increases, so does the effect of the magnetic flux density on the limiting current.

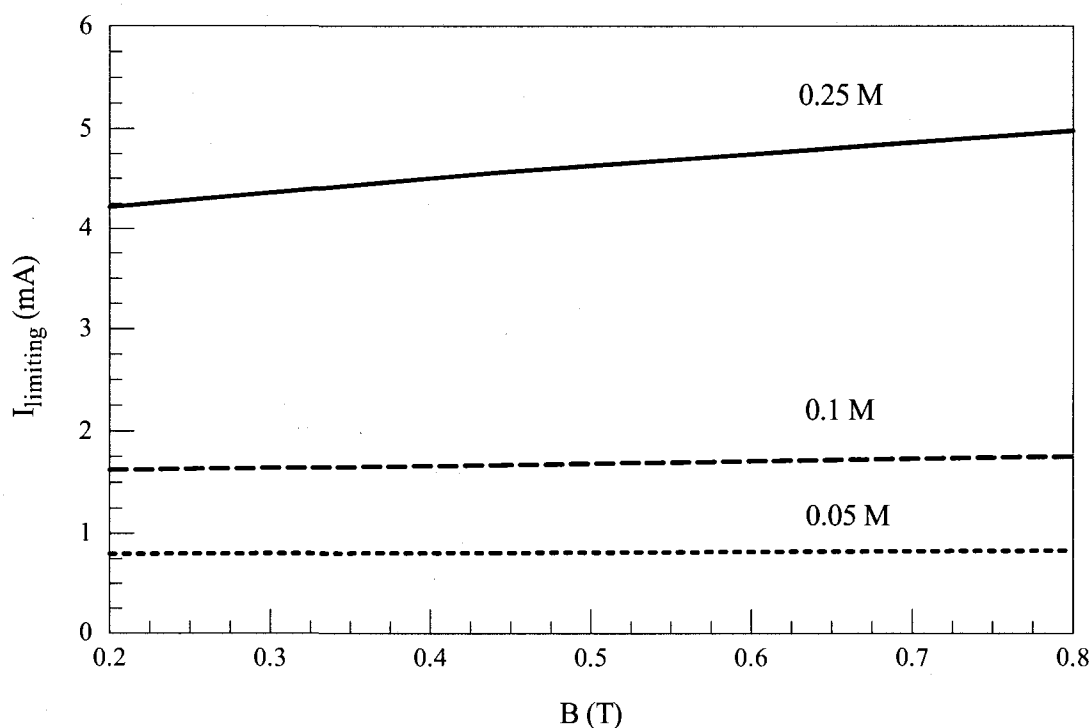


Figure 2.13: The limiting current as a function of the magnetic flux density

For higher concentration of the RedOx species, the limiting current nearly linearly increases with the magnetic flux density. As the magnetic flux density increases, the

induced MHD flow increases, the thickness of the concentration boundary layers next to the electrodes decrease, consequently, the current density and the total current increases. Figure 2.14 depicts the maximum average velocity corresponding to the limiting current condition as a function of the magnetic flux density under various concentrations of the RedOx species. The conditions are the same as those in Figure 2.13. According to (18), the effect of the magnetic flux density on the average velocity is due to the combined effects of  $B$  on the current and  $B$  itself. For low concentration of the RedOx species, since the effect of the magnetic flux density on the limiting current is insignificant (Figure 2.13), the average velocity corresponding to the limiting current linearly increases as the magnetic flux density increases. For higher concentration of the RedOx species, the average velocity nonlinearly increases with the magnetic flux density since the effect of the magnetic flux density on the limiting current becomes more pronounced. The theoretical predictions from the full mathematical model (lines) agree well with the predictions obtained from the closed-form approximation (symbols) using the obtained limiting current as depicted in Figure 2.13.

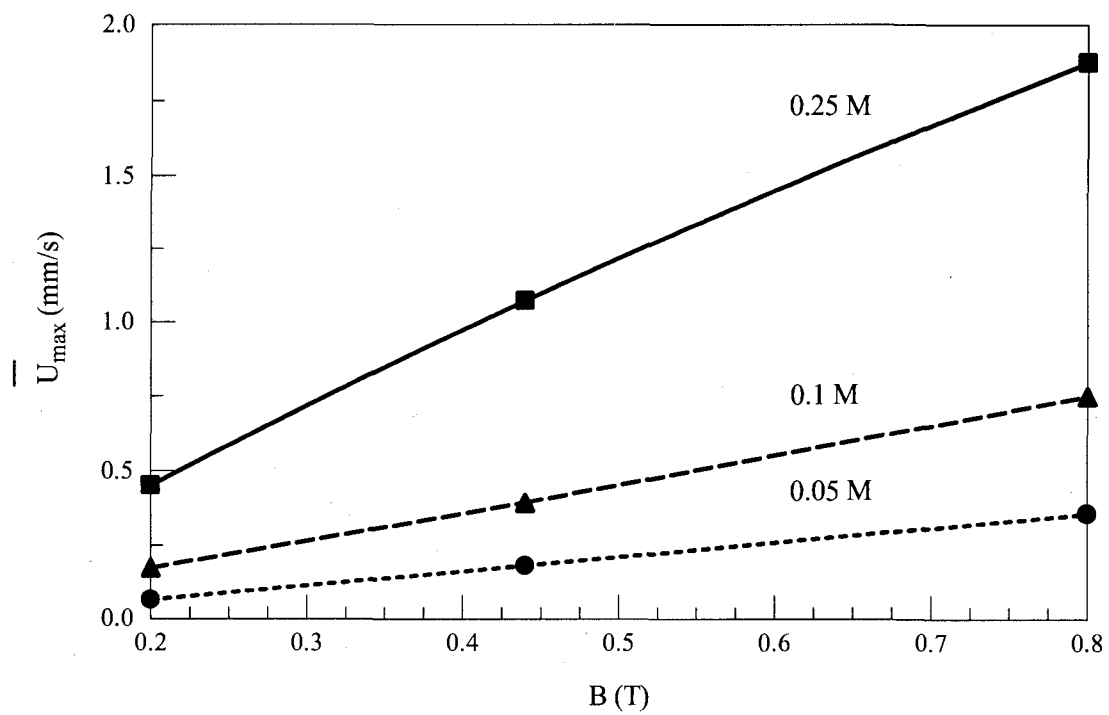


Figure 2.14: The average velocity as a function of the magnetic flux density.

## CHAPTER 3

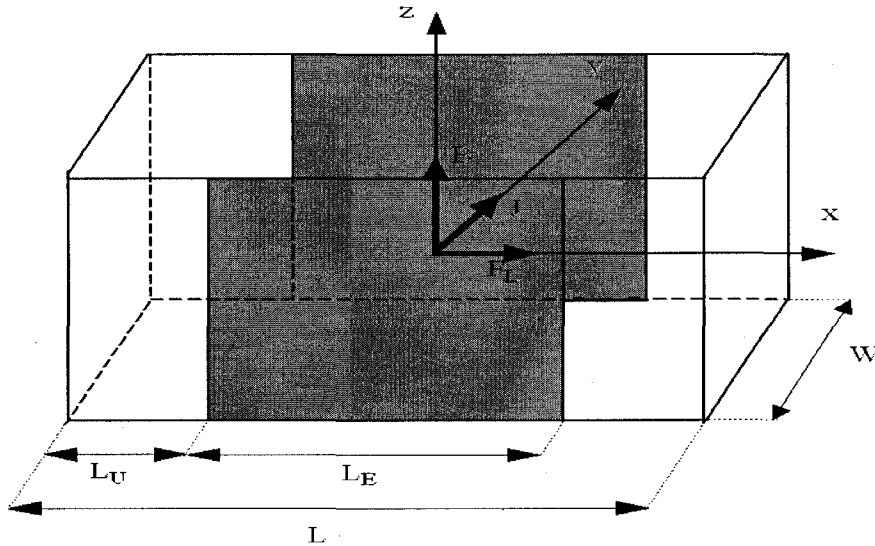
### ANALYSIS OF MAGNETOHYDRODYNAMIC MICROPUMPS AND NETWORKS

#### 3.1 Introduction

This work presents a new closed form solution for the velocity profile of Magnetohydrodynamic (MHD) flows in microchannels, which consists of a pair of electrodes deposited on opposite walls of the conduit and externally applied magnetic field. These electrodes produce an electric current whose interaction with the magnetic field creates Lorentz force which initiates and maintains the flow within the channel. Factors affecting Lorentz force include the dimensions of the conduit, the current applied on its opposite sides, the pressure drop across it, and the physical properties of the fluid. It can be applied to any channel having an aspect ratio (the ratio of the channel's depth to width) of meters to micrometers, and is valid for 3D fully developed, steady and incompressible flows. Moreover, it will be verified with both published and experimental data, where the current can be either alternating or direct. Then, some case studies shall be conducted, where the presented closed form solution will aid as an analytical tool to find the velocity profiles, mean velocity, maximum velocity, and even mass flow rate at any given point within the channel. It will act as a tool which will approximate the velocity profile for MHD flows (with little error) via neglecting the Navier Stokes equation, thus reducing the time needed to perform a computational fluid dynamics analysis.

### 3.2 Mathematical Model

A planar microchannel with a length of  $L$  and a rectangular cross-section of height  $2b$  and width  $2a$  is considered. A Cartesian coordinate system whose origin is at the center of the channel shall be adopted. The coordinates  $x$ ,  $y$ , and  $z$  are aligned, respectively, along the conduit's length, width, and depth ( $-L/2 \leq x \leq L/2$ ,  $-a \leq y \leq a$ , and  $-b \leq z \leq b$ ). It will be always assumed that  $b \geq a$  since this situation can always be realized through rotation. Two planar electrodes of length  $L_E$  are deposited along the two opposing walls, with the leading edge located at a distance  $L_U$  downstream of the conduit's entrance ( $L_U \leq x \leq L_U + L_E$ ), and  $W$  is the distance between the two walls. The parts of the conduit's walls that are free of electrodes are synthesized of dielectric material. Figure 3.1 schematizes the suggested three-dimensional, planar microchannel model.





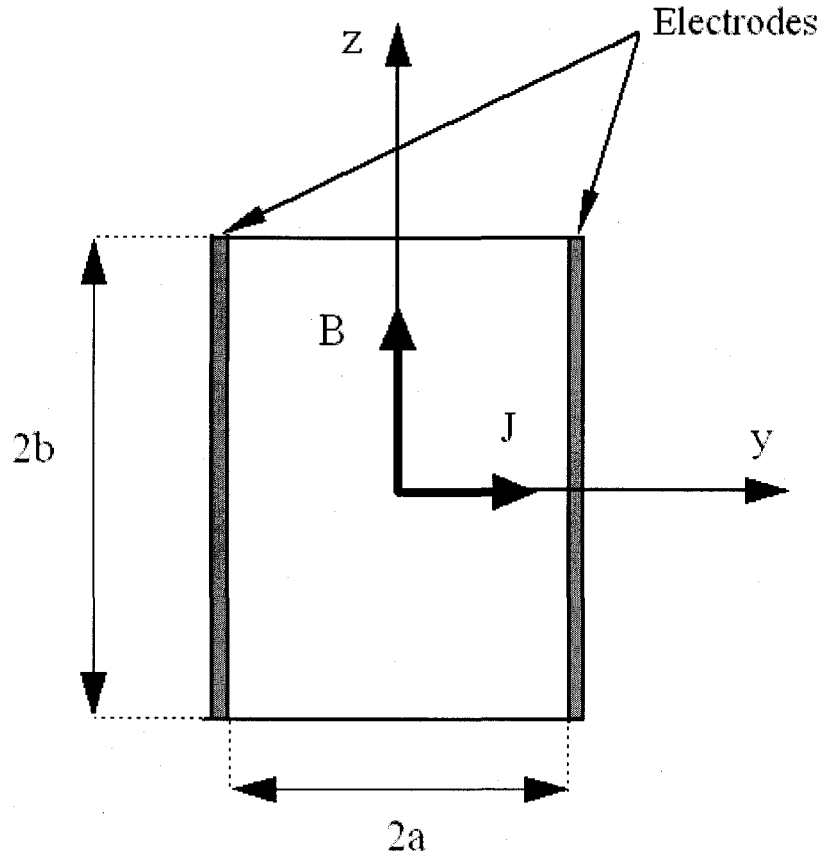


Figure 3.1-a and -b: Schematic diagram of the Model

An electrolyte solution, characterized with being a weak conductor fills the microchannel. When a potential difference is applied across the two planar electrodes (located along the opposing walls), an electric current of density  $\mathbf{J}$  transmits through the electrolyte solution. Bold letters shall denote vectors henceforward. If the microfluidic device is placed in a magnetic field with a magnetic flux density  $\mathbf{B}$  (supplied by a permanent magnet or an electromagnet), the interaction between the current density  $\mathbf{J}$  and the magnetic field  $\mathbf{B}$  induces a Lorentz force of density,  $\mathbf{J} \times \mathbf{B}$ . This force can be used to manipulate fluids for various microfluidic applications (Arumugam et al 2006). Both DC

and AC electric fields can be harnessed for MHD-based microfluidics. In the following sections, I shall first describe the DC MHD then the AC MHD model.

### 3.2.1 The Mathematical Model for the Fluid Motion in DC MHD

The electrolyte solution shall be considered incompressible. Under steady state, the flow driven by both the Lorentz force and the pressure gradient is governed by continuity and Navier-Stokes equations:

$$\nabla \cdot \mathbf{u} = 0 \quad (1)$$

and

$$\rho \mathbf{u} \cdot \nabla \mathbf{u} = -\nabla p + \mu \nabla^2 \mathbf{u} + \mathbf{J} \times \mathbf{B}. \quad (2)$$

In the above,  $p$  is the pressure;  $\rho$  and  $\mu$  denote, respectively, the electrolyte solution's density and dynamic viscosity;  $\mathbf{u} = u\mathbf{e}_x + v\mathbf{e}_y + w\mathbf{e}_z$  is the fluid's velocity in which  $u$ ,  $v$ , and  $w$  are, respectively, the velocity components in the  $x$ -,  $y$ -, and  $z$ - directions. The following shall be neglected: (i) the natural convection induced by the density variations due to electrochemical reactions taking place on the surface of the electrodes (Clark et al 2004), (ii) the paramagnetic forces induced by the concentration gradients of the paramagnetic species (Eijkel et al 2004), and (iii) the induced magnetic field due to small Reynolds numbers of the MHD flows in microchannels. Furthermore, it shall be assumed that the magnetic field is uniform in the  $z$ -direction, which is appropriate approximation since the size of the magnet is much larger than that of the microfluidic device.

In order to solve the equations (1) and (2), appropriate boundary conditions are needed. A non-slip boundary condition is used at the solid walls of the microchannel, whereas normal pressure boundary conditions are used at the entrance ( $x = -L/2$ ) and exit ( $x = L/2$ ) of the microchannel:

$$p(-\frac{L}{2}, y, z) = P_1, \quad (3)$$

$$\mathbf{t} \cdot \mathbf{u}(-\frac{L}{2}, y, z) = 0, \quad (4)$$

$$p(\frac{L}{2}, y, z) = P_2, \quad (5)$$

$$\mathbf{t} \cdot \mathbf{u}(\frac{L}{2}, y, z) = 0, \quad (6)$$

where  $\mathbf{t}$  is the unit vector tangent to the planes  $x = \pm \frac{L}{2}$ . The externally applied pressure gradient is  $\Delta p/L$  with  $\Delta p = P_1 - P_2$ . In the absence of the externally applied pressure gradient across the microchannel,  $P_1 = P_2 = 0$ .

The spatial distribution of the current density  $\mathbf{J}$  within the electrolyte solution is required to numerically solve the flow field from the equation (1) and the set of the equations (2) subjected to the appropriate boundary conditions. The current density is related to the ionic mass transport and the electrochemical reaction along the surface of the electrodes (Yi et al 2002).

Based on previous results by Gao et al (2007), the MHD flow is fully developed in most regions of the 3D planar microchannel and the  $x$ -component velocity can be approximated with that of a fully-developed duct flow having a rectangular cross-section (White 2006):

$$u(y, z) = A_1 \bar{U} \sum_{i=1,3,5,\dots}^{\infty} (-1)^{\frac{i-1}{2}} \left[ 1 - \frac{\cosh\left(\frac{i\pi z}{2a}\right)}{\cosh\left(\frac{i\pi b}{2a}\right)} \right] \frac{\cos\left(\frac{i\pi y}{2a}\right)}{i^3}, \quad (7)$$

$$\text{where } A_1 = \frac{48}{\pi^3 \left[ 1 - \frac{192a}{\pi^5 b} \sum_{j=1,3,5,\infty} \frac{\tanh(j\pi b/2a)}{j^5} \right]}. \quad (8)$$

In the above,  $\bar{U}$  is the cross-sectional average velocity. It is important to mention here that  $a=\min(H/2, W/2)$  and  $b=\max(H/2, W/2)$ . The above approximation of the MHD flow with a fully developed pressure-driven Poiseuille flow has been previously adopted by many groups (Bau et al 2003, Homsy et al 2005, Wang et al 2004).

$A_1$  can be modified to the following relationship:

$$A_1 = \frac{48}{\left[ \pi^3 - \frac{192a}{\pi^2 b} \left( \tanh\left(\frac{\pi b}{2a}\right) \right) \right]}, \quad (9)$$

The steady x-component momentum equation can be approximated by:

$$-\frac{\partial p}{\partial x} + \mu \left( \frac{\partial^2 u}{\partial y^2} + \frac{\partial^2 u}{\partial z^2} \right) + J_y B = 0 \quad (10)$$

with  $J_y$  is the y-component current density. Equation (10) represents a balance among the three forces: pressure force, viscous force, and Lorentz force. Substituting the expression (7) into (10), and taking volume integration of the equation (10) in the domain  $-L/2 \leq x \leq L/2$ ,  $-a \leq y \leq a$ , and  $-b \leq z \leq b$ , then

$$4\Delta p a b - 2A_1 \bar{U} \mu L \pi \frac{b}{a} \sum_{i=1,3,5,\infty} (-1)^{\frac{i-1}{2}} \frac{\sin\left(\frac{i\pi}{2}\right)}{i^2} + IBW = 0. \quad (11)$$

The series solution in equation (11) is:

$$\sum_{i=1,3,K}^{\infty} (-1)^{\frac{i-1}{2}} \frac{\sin\left(\frac{i\pi}{2}\right)}{i^2} = \sum_{j=1,2,K}^{\infty} (-1)^j \frac{\sin\left((2j+1)\frac{\pi}{2}\right)}{(2j+1)^2} = \frac{\pi^2}{8}. \quad (12)$$

So, I obtained a closed-form solution to the cross-sectional average velocity:

$$\bar{U} = \frac{16a^2}{\pi^3 A_1 \mu} \frac{\Delta p}{L} + \frac{4aWB}{\pi^3 b A_1 \mu L} I. \quad (13)$$

The volumetric flow rate  $Q$  is

$$Q = 4\bar{U}ab = \frac{64a^3b}{\pi^3 A_1 \mu} \frac{\Delta p}{L} + \frac{16a^2WB}{\pi^3 A_1 \mu L} I. \quad (14)$$

The resulting closed-form expressions for the average velocity and flow rate take into account the combined effects of pressure-driven force and Lorentz force. In the absence of the pressure difference between the conduit's inlet and exit (i.e.,  $\Delta p = 0$ ), the average velocity is

$$\bar{U} = \frac{4aWB}{\pi^3 b A_1 \mu L} I, \quad (15)$$

and the volumetric flow rate is

$$Q = \frac{16a^2WB}{\pi^3 A_1 \mu L} I. \quad (16)$$

Therefore, the performances of DC MHD micropumps and networks can be estimated by applying the obtained closed-form expression (14) without solving the 3D PDEs (1) and (2). Compared to the average velocity and flow rate (in terms of a series form) expressions obtained by many groups (Bau et al 2003, Homsy et al 2005, Wang et al 2004), the resulting closed-form expressions for the average velocity and flow rate are more practical as they can be applied for example for inverse problems, including the optimization of the channel's dimensions and the determination of the currents needed to

achieve the desired flow rates and flow patterns in MHD microfluidic networks (Ho 2007 and Homsy et al 2007). In addition, the series solutions for the average velocity and flow rate -obtained by other groups- are only valid when  $\Delta P=0$  i.e. when there is no externally applied or induced pressure gradient across the two ends of the channel. However, the fact is that in many MHD-based microfluidic applications such as MHD networks (Ho 2007, Homsy et al 2007, and Affanni et al 2006) and MHD switch circuitry (Lemoff and Lee, 2003), a pressure gradient will be induced across the branch even in the absence of the externally applied pressure gradient.

### 3.2.2 The Mathematical Model for the Fluid Motion in AC MHD

In AC MHD, AC electric and magnetic fields are used. The magnetic flux density is  $\mathbf{B} \sin(\omega t)$ , and the current density in solution is  $\mathbf{J} \sin(\omega t + \phi)$ , where  $\omega$  is the angular frequency of the fields and  $\phi$  is the phase angle between the electric and magnetic fields. The momentum equation of the fully developed AC MHD flow is the following:

$$\rho \frac{\partial u}{\partial t} = -\frac{\partial p}{\partial x} + \mu \left( \frac{\partial^2 u}{\partial y^2} + \frac{\partial^2 u}{\partial z^2} \right) + J_y B \sin(\omega t) \sin(\omega t + \phi). \quad (17)$$

The time-averaged velocity and pressure are, respectively,  $\langle u \rangle = \int_0^{2\pi} u d\omega t$  and

$$\langle p \rangle = \int_0^{2\pi} p d\omega t.$$

Integrating Eq. (17) with respect to  $\omega t$  from  $\omega t=0$  to  $2\pi$ , then

$$-\frac{\partial \langle p \rangle}{\partial x} + \mu \left( \frac{\partial^2 \langle u \rangle}{\partial y^2} + \frac{\partial^2 \langle u \rangle}{\partial z^2} \right) + J_y B \frac{\cos(\phi)}{2} = 0. \quad (18)$$

In comparing equation (18) with equation (10), I found that the only difference is that a

factor  $\frac{\cos(\phi)}{2}$  occurs in the 3<sup>rd</sup> term in the LHS.

Based on the solution of the equation (10), a closed-form solution of the cross-sectional average velocity in AC MHD is

$$\langle \bar{U} \rangle = \frac{16a^2}{\pi^3 A_1 \mu} \frac{\Delta p}{L} + \frac{2aWB}{\pi^3 b A_1 \mu L} I \cos(\phi). \quad (19)$$

The time-averaged volumetric flow rate  $\langle Q \rangle$  is

$$\langle Q \rangle = \frac{64a^3b}{\pi^3 A_1 \mu} \frac{\Delta p}{L} + \frac{8a^2WB}{\pi^3 A_1 \mu L} I \cos(\phi). \quad (20)$$

In the absence of the pressure difference across the two ends of the microchannel (i.e. when  $\Delta p = 0$ ), the cross-sectional average velocity and the time-averaged flow rate in AC MHD are, respectively,

$$\langle \bar{U} \rangle = \frac{2aWB}{\pi^3 b A_1 \mu L} I \cos(\phi), \quad (21)$$

and

$$\langle Q \rangle = \frac{8a^2WB}{\pi^3 A_2 \mu L} I \cos(\phi). \quad (22)$$

### 3.3 Results and Discussions

In this section, I will compare the results of the closed-form solutions of the cross-sectional average velocity in both DC MHD and AC MHD micropumps and networks with data obtained from literature. Literature data shall be divided into two parts: experimental data and numerical data. Those comparisons shall validate my closed form solution.

### 3.3.1 Validation of the Closed Form Solution for DC MHD

The current produced by the electrodes deposited at the opposite sides of the channel in DC MHD flows is independent of time i.e. has a fixed and constant magnitude.

First, the results of the closed form solution are compared to DC results obtained by Ho 2007. Ho presents a DC MHD flow in a channel of length 80 mm, depth 7 mm, width 3-20 mm and electrodes of length 35 mm. The magnetic field is fixed at 0.02 T. The viscosity of the fluid used is 0.0006 Pa.s while its density is 1058 kg/m<sup>3</sup>. The input current varies from 0.1 to 1.3 A. Two sets of experimental runs were done, where in the first, the flow rate was sought within the channel while varying its width. I compared such data to my closed form solution and represented this in Fig.2.2. The symbol (▲) represents experimental data, whereas the solid line represents my closed form solution. The magnetic field density is 0.02 T and the input current is 0.7 A. Other quantities remain as mentioned above. It is obvious that there is a good match between my closed form solution and the experimental data points, and it can be noticed that the error is very small for width less than 1.5 mm, increasing for higher values.



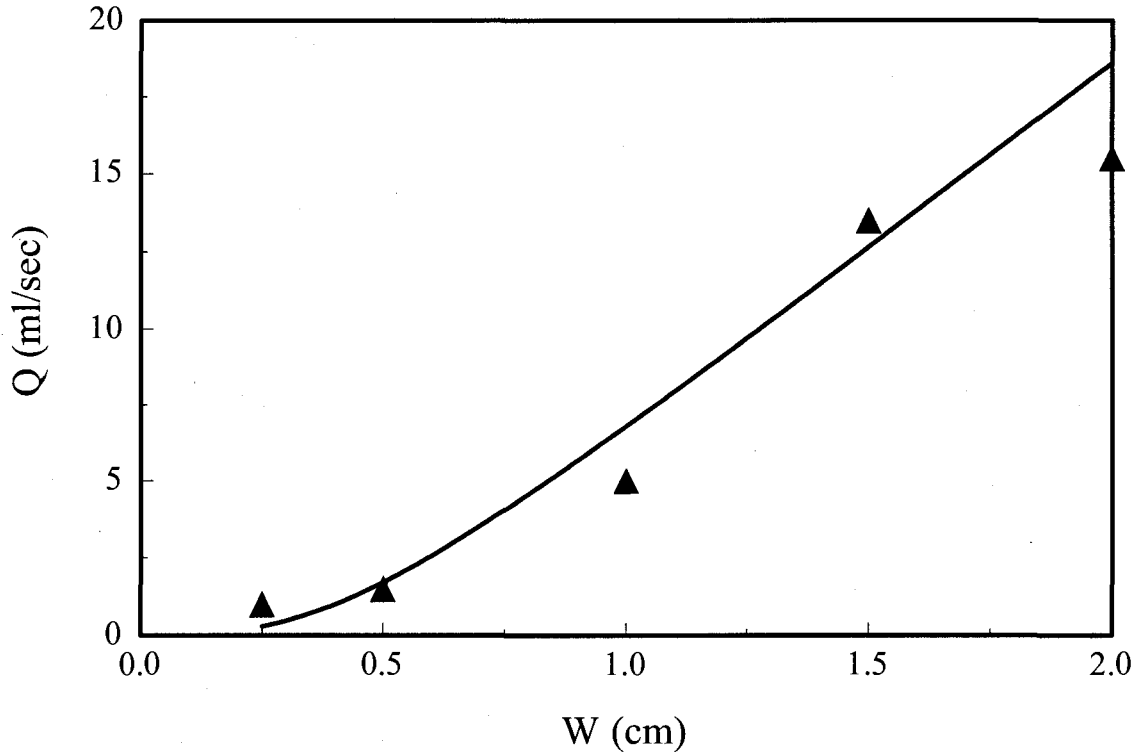


Figure 3.2: Comparisons with Ho's experimental data

This can be correlated to bubble formation, another physical phenomenon occurring in the channel due to traces of ions in the flowing solution flowing. In presence of charged electrodes, electrolysis may occur, where the produced bubbles retard the flow. Experimental results encountered this process, unlike my closed form solution.

The mean velocity in the duct is plotted in fig. 2.3. as a function of the current applied, and my closed form solution is compared to experimental data from the above-mentioned reference. In this plot, the channel has a length of 80 mm, a width of 3 mm, and a depth of 7 mm. Other physical quantities are as follows: magnetic field of 0.02 T, solution viscosity of 0.0006 Pa.s, and an applied current of 0 to 1.4 A. The symbol ( $\blacktriangle$ ) represents the experimental data and the solid line represents my closed form solution. Again, notice the good match between both results. At higher current values though, there

is a deviation due to the same physical phenomenon mentioned above i.e. bubble formation.

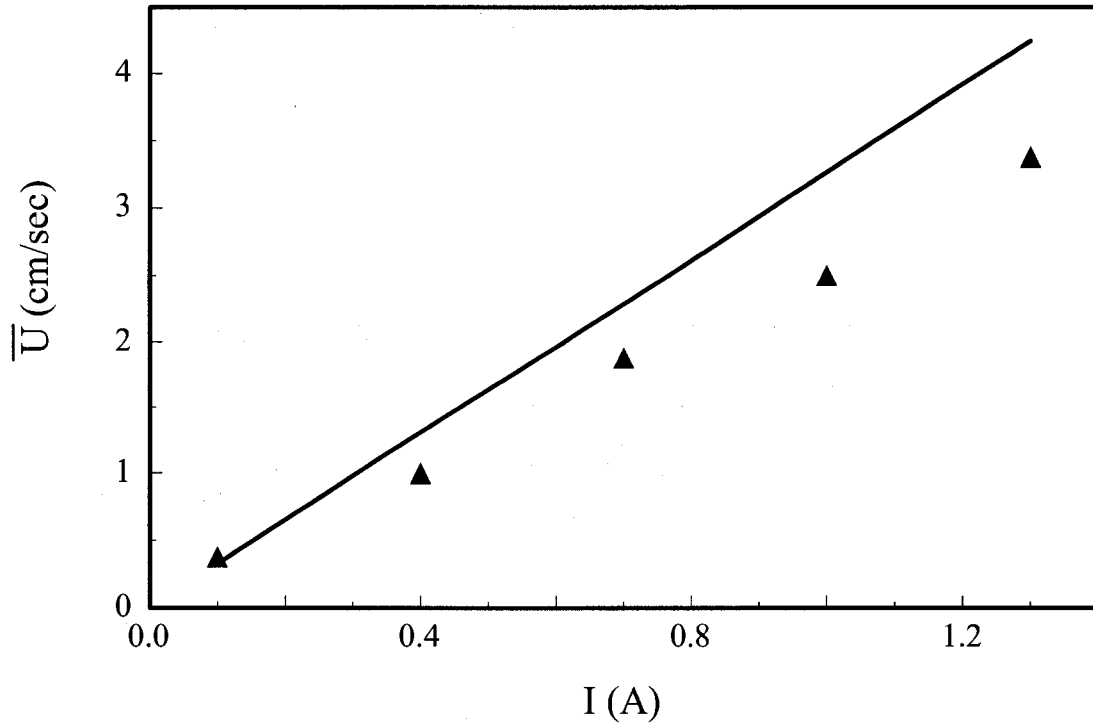


Figure 3.3: Comparisons with Ho's experimental data

As stated before, formed bubbles retard the flow within the channel, leading to the fact that numerical results will overestimate the experimental data. Notice, however, that at very high current values ( $>1$  A), this deviation increases due to the rapid electrolysis, but the relative error is still acceptable.

It can thus be concluded, that the closed form solution gives reliable results when the pressure drops are considered to be negligible.

The results of the closed form solution are compared with the experimental results produced by Bau et al 2003. In this paper, Bau designed a network of a circulating

solution which applies the principles of MHD. Figure 3.4 represents this network, whereas Figure 3.5. shows the equivalent grid network.

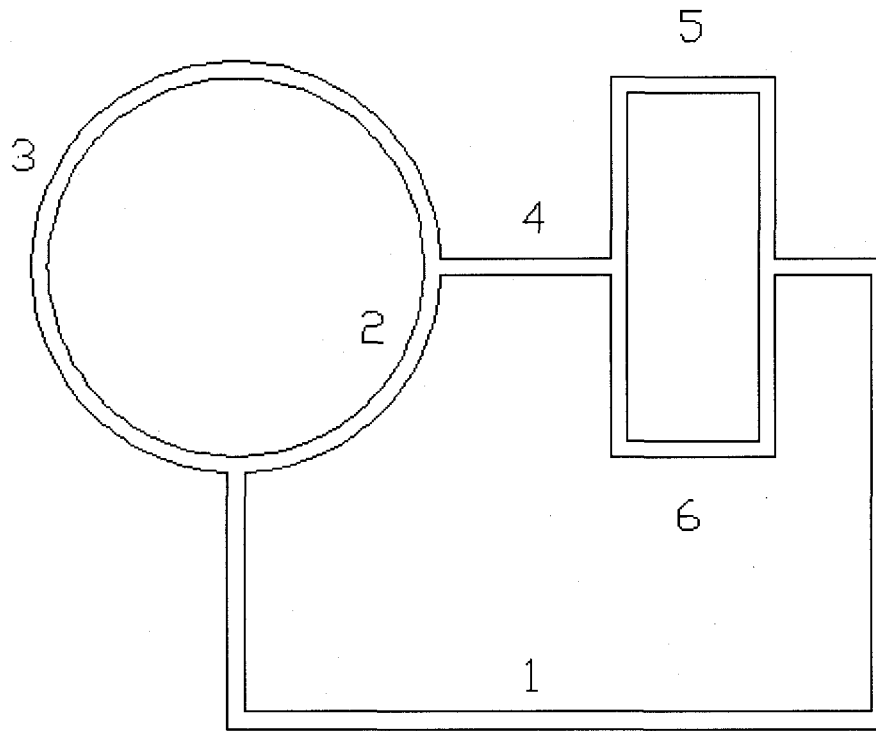


Figure 3.4: A schematic diagram of the network used in Bau's paper

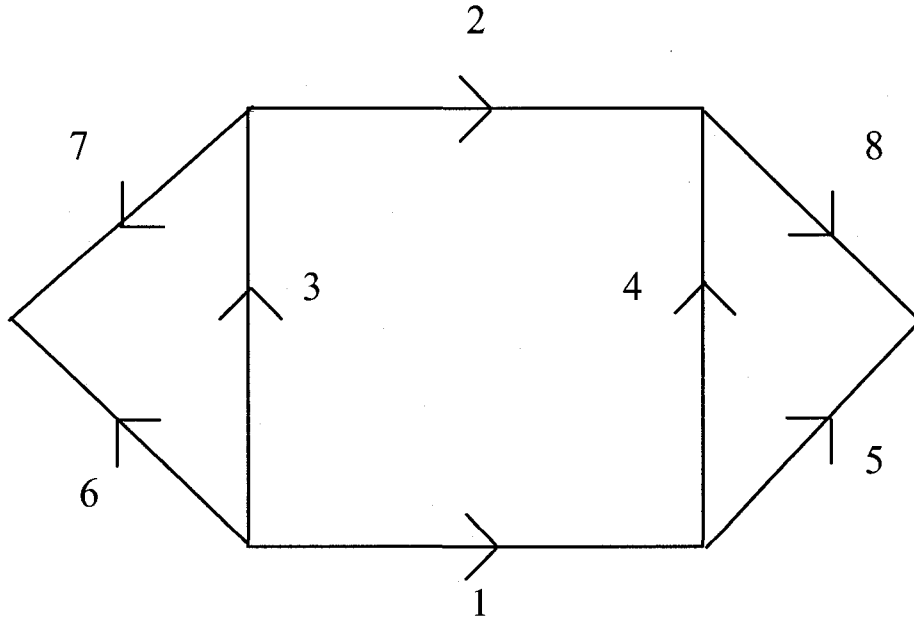


Figure 3.5: The equivalent network of the above presented network by Bau.

The lengths of the channels within the network are: 77.5 mm, 10 mm, 9.8 mm, 22.5 mm, 11.25 mm, 14.7 mm, 14.7 mm, and 11.25 mm corresponding to the branches 1, 2, 3, 4, 5, 7, and 8 respectively. The height and width of the channels are uniform, with values of 1.7 mm and 1.1 mm. It should be mentioned that in his paper, Bau stated that the current density within the channel is not uniform. Therefore, the uniform current density must be multiplied by a numerical coefficient,  $k$ , to give the actual value of current density. In his design, he stated a value of 0.16 for  $k$ . The current is given as 10.301 mA, 1.322 mA, 0.967 mA, 1.491 mA, 0.745 mA, 0.484 mA, 0.484 mA, and 0.745 mA corresponding to the branches 1, 2, 3, 4, 5, 7, and 8 respectively. The viscosity of the flow is given as 0.001 Pa.s. Finally, the pressure drop within each branch is negligible. Based on these quantities, the flow within each branch was measured experimentally and reported. I compared those values with those produced by my closed form solution,

where Table.3.1 shows this comparison. It can be clearly concluded that there is a perfect match between the values.

Table 3.1. Comparison between Bau et al and results predicted by my closed form

Chord No	Length (mm)	Current (mA)	Numerical Flow Rate ( $\mu\text{l/s}$ )	Experimental Flow Rate ( $\mu\text{l/s}$ )
1	77.5	10.301	0.75	0.752
2	10	1.322	0.75	0.748
3	9.8	0.967	0.563	0.558
4	22.5	0.491	0.375	0.375
5	11.25	0.745	0.375	0.375
6	14.7	0.484	0.188	0.186
7	14.7	0.484	0.188	0.186
8	11.25	0.745	0.375	0.375

Thus, the closed form solution is validated for the case where the pressure drop is neglected or taken to be zero, and remains to be validated when the pressure drop is taken into consideration. In a paper by Affanni et al (2006), a closed square loop was considered, which consists of four branches with a pair of electrode installed in one of the branches. Figure. 3.6. illustrates this square loop. The branch where the pair of electrodes is installed initiates the flow in the loop, whilst in the rest of the loop the flow is pressure driven. In other words, this branch acts as the pumping branch, and has the following dimensions: 1.3 mm in depth and 5 mm in depth. The length of the equivalent circuit is 93 mm.

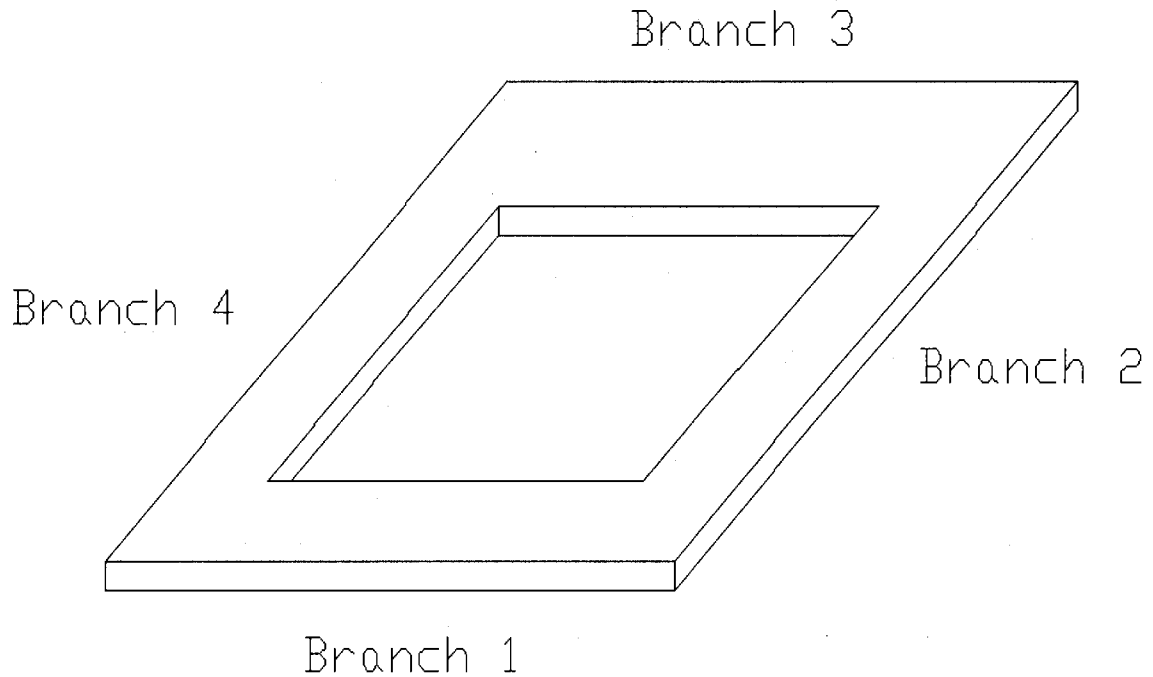


Figure 3.6: A schematic diagram of the micro loop used by Affani et al

By utilizing the “FEMLAB” software, Affani was able to find the pressure drop within each branch of the loop. Now, I will compare the values of those pressure drops with those calculated by the closed form solution and present the method adopted. There are five unknowns, namely the pressure drops at each branch, and the volumetric flow rate flowing through the loop. We have four equations for each branch relating the volumetric flow rate to other physical quantities, and one constraint that sets the summation of all pressure drops in the loop to zero. This system of equations can be solved by any numerical method, such as Gauss Elimination. Other physical quantities are as follows: the viscosity of the fluid is given as 0.0011 Pa.s, the magnetic field is 0.07 T, and finally the electric current is 0.2 A. Figure. 3.7 shows the comparison between the pressures at the inlet and outlet of each branch, where it can be clearly seen that there is a

good match between both results. The reason underlying the fact that my closed form overestimates there results is that there are bends in the loop. Consequently, the length should be modified, while in “FEMLAB” it is automatically modified.

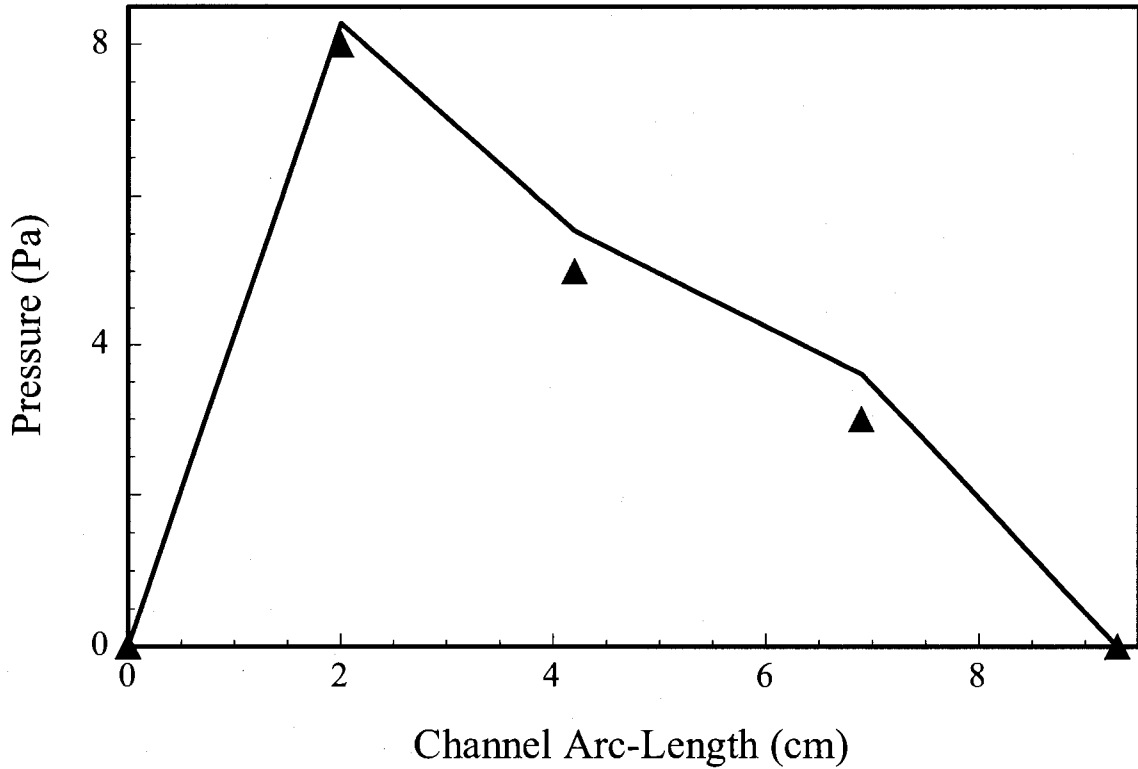


Figure 3.7: Comparison between the pressure of the micro loop presented in figure 3.6.

The closed form solution is compared here with the results produced by the 3D MHD model presented in Chapter 2. “FEMLAB” software is used to simulate the case of a channel of 45 mm in length and 35 mm length of electrodes. The height and width are kept variables, where the width can be 500  $\mu\text{m}$ , 800  $\mu\text{m}$ , or 1000  $\mu\text{m}$ , wheaeras the depth can vary from 0 to 1.5 mm. Other physical quantities are given as: electric current of 0.1 A; magnetic field of 0.018 T; and dynamic viscosity of 0.0006 Pa.s. Figure. 3.8 illustrates

this comparison, where the solid line presents the closed form approximation and the triangles present the 3D simulations. The variation of mean velocity with respect to channels depth at three different widths is displayed, and it is clear that there is a very good match between both results.

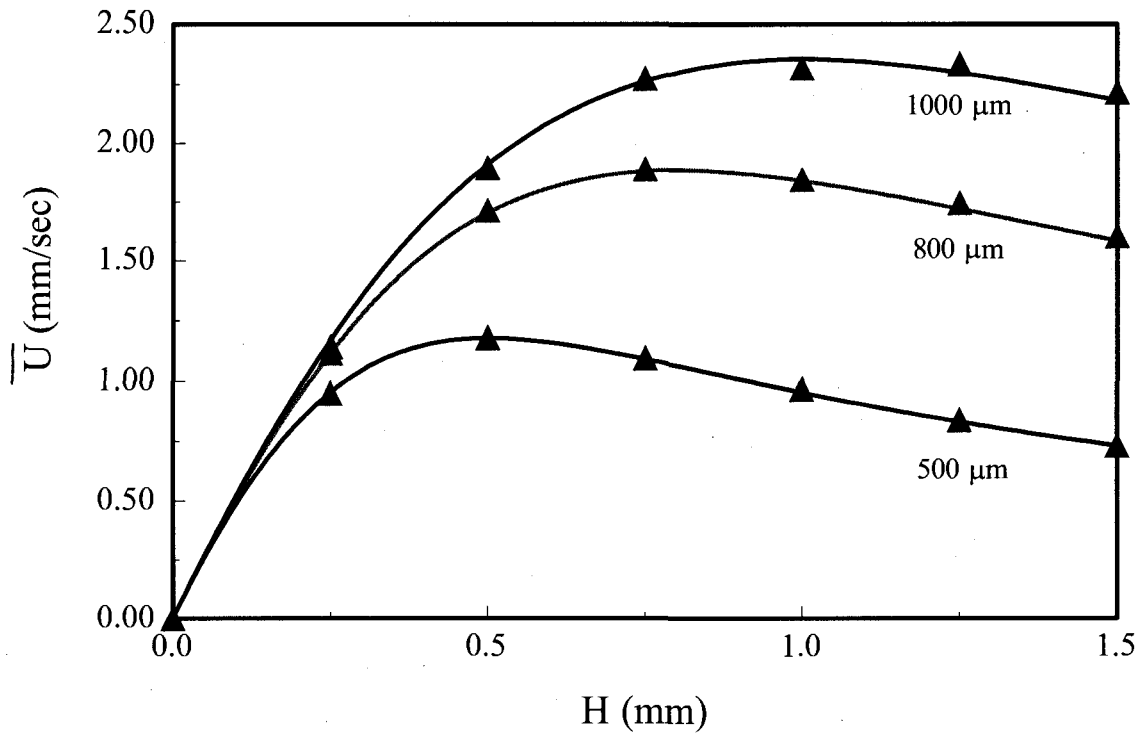


Figure 3.8: The mean velocity as a function of the channels height

Figure.3.9. illustrates the mean velocity as a function of both width and height. It is clear that for a small aspect ratio (less than one), the velocity increases rapidly as the aspect ratio increases.



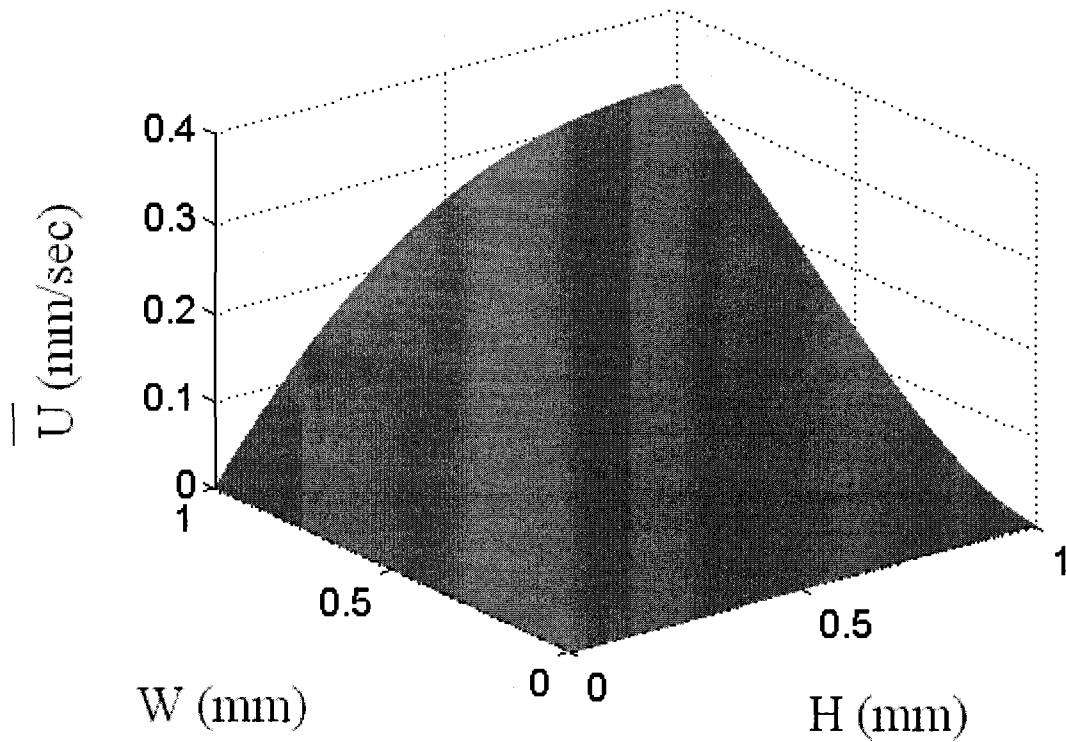


Figure 3.9: The mean velocity as a function of the channels height and width.

The peak is at the aspect ratio of one, after which the speed faces a gradual decline with increases in the aspect ratio. The physical conditions for this plot are as follows: the length of the channel is 45 mm, the magnetic field is 0.4 T, the electric current is 1 mA, and the dynamic viscosity is 0.001 Pa.s

Other crucial relations that demand attention are the effects of the physical quantities  $\Delta P$  (pressure drop) and  $I$  (electric current) on average velocity. Figure. 3.10 illustrates this plot. The square channel has dimensions of 500  $\mu\text{m}$  in height and width, and 45 mm in length. Other physical properties are given as: 0.44 T magnetic field and 0.001 Pa.s solution's viscosity.

It is clear from this plot that average velocity increases as a result of increases in  $\Delta P$  and  $I$ , and that the increase in the current gives a higher increase in the mean velocity than the increase in the  $\Delta P$ . Notice that the mean velocity drops to zero when both  $I$  and  $\Delta P$  are both zeros or when:

$$\Delta P = -\frac{I \times B}{H} \quad (23)$$

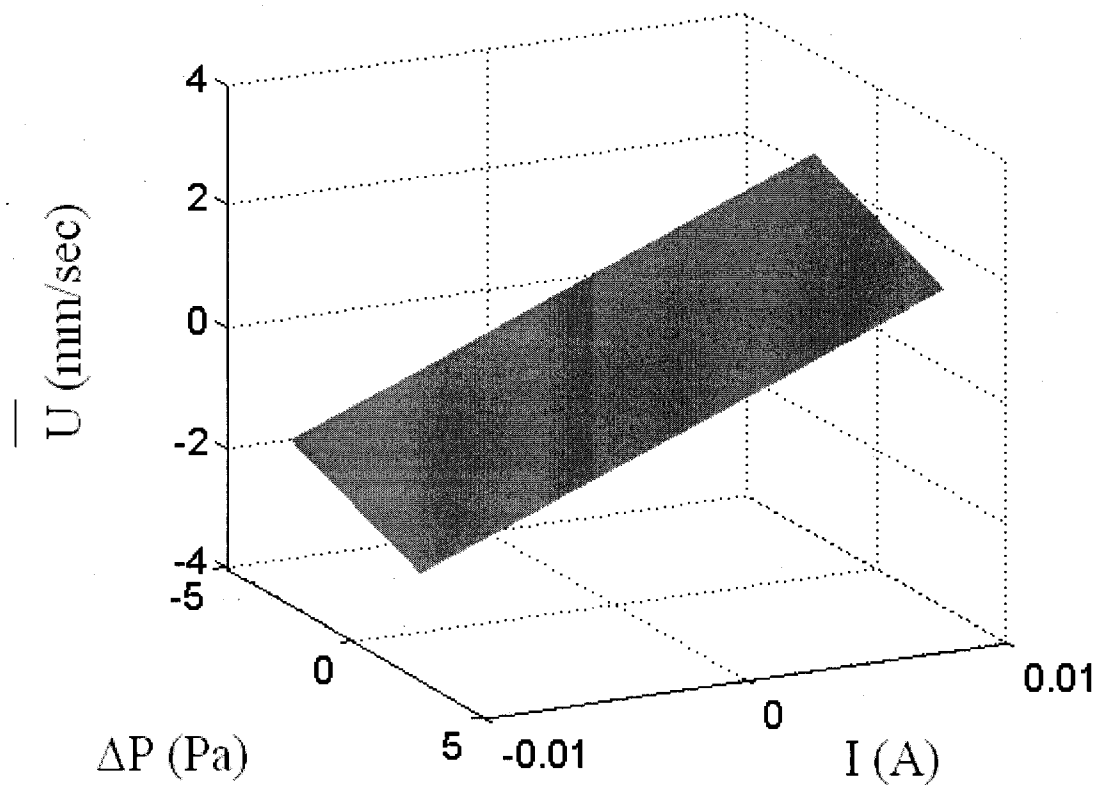


Figure 3.10: The mean velocity as function of applied current and the pressure drop

In the previous equation,  $I$  is the electric current,  $B$  is the magnetic field and  $H$  is the height of the channel. This means that the pressure drop is balanced by the Lorentz force per unit area of the electrode.

### 3.3.2 Validation of the Closed Form Solution for AC MHD

The current produced by the electrodes deposited at the opposite sides of the channel in AC MHD depends on time. The closed form solution has the same derivation, with the exception that I am going to find here the time-averaged velocity. Moreover, the form here depends on a new factor i.e. the phase angle, which represents the shift between the current density wave and that of the magnetic flux.

Lemoff et al (2000) experimental data are compared to the results produced by the closed form solution. Lemoff designed and tested an AC MHD-driven flow micro-channel of length 20 mm, width 800  $\mu\text{m}$ , and height 380  $\mu\text{m}$ . The length of the electrodes is 4mm, while other physical quantities are given as: solution viscosity of 0.0006 Pa.s, magnetic field of 13 mT, and an applied electric current varying with the following values: 140, 100, 36, 24, 12, and 10 mA. Solutions utilized in the experiments are: 1 M NaCl, 0.1 M NaCl, 0.01 M NaCl, 0.01 M NaOH, PBS (pH 7.2), and lambda DNA in 5mM NaCl. In addition to those data points, the results shall also be compared with the results of the numerical simulations for the same data done by Lemoff 2006 and Wang et al 2004. Figure.3.11 shows these comparisons, where time-averaged velocity is plotted against six different scenarios, namely 1 M NaCl and 140 mA, 0.1 M NaCl and 100 mA, 0.01 M NaCl and 36 mA, 0.01 M NaOH and 24 mA, PBS (pH 7.2) and 12 mA, and finally lambda DNA in 5mM NaCl and 10 mA. The solid line presents the prediction,

(▲) presents Lemoff experimental data, (●) presents Lemoff's numerical data, and (■) presents Wang's numerical data.

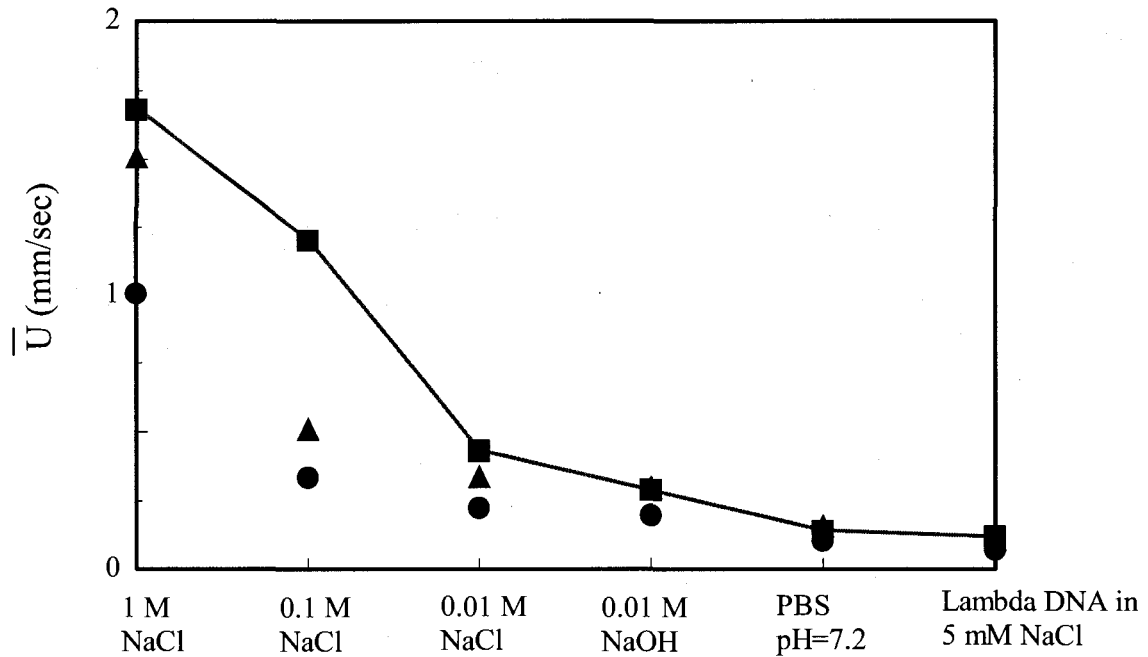


Figure 3.11: The time averaged velocity versus six different scenarios

The time-averaged velocity is plotted as a function of phase angle ( $\phi$ ). Data points from experiments performed by Lemoff shall be used for comparison with the closed form solution. Figure. 3.12 shows this comparison, in which the solid line represents the closed form solution while the symbol (▲) represents the experimental data from Wang et al 2004. The magnetic field is 2.51 mT and the applied current is 75 mA. The channel has the following dimensions: 380  $\mu\text{m}$  in height, 800  $\mu\text{m}$  in width, and 20 mm in length. The viscosity is 0.0006 Pa.s. It is clear that the mean velocity follows a sinusoidal wave, and that there is a good match between both results. It should be stated here that for Figures. 3.11 and 3.12, the pressure drop is considered negligible. These displayed

comparisons increase the confidence in my closed form solution for AC MHD flow in micro-channels.

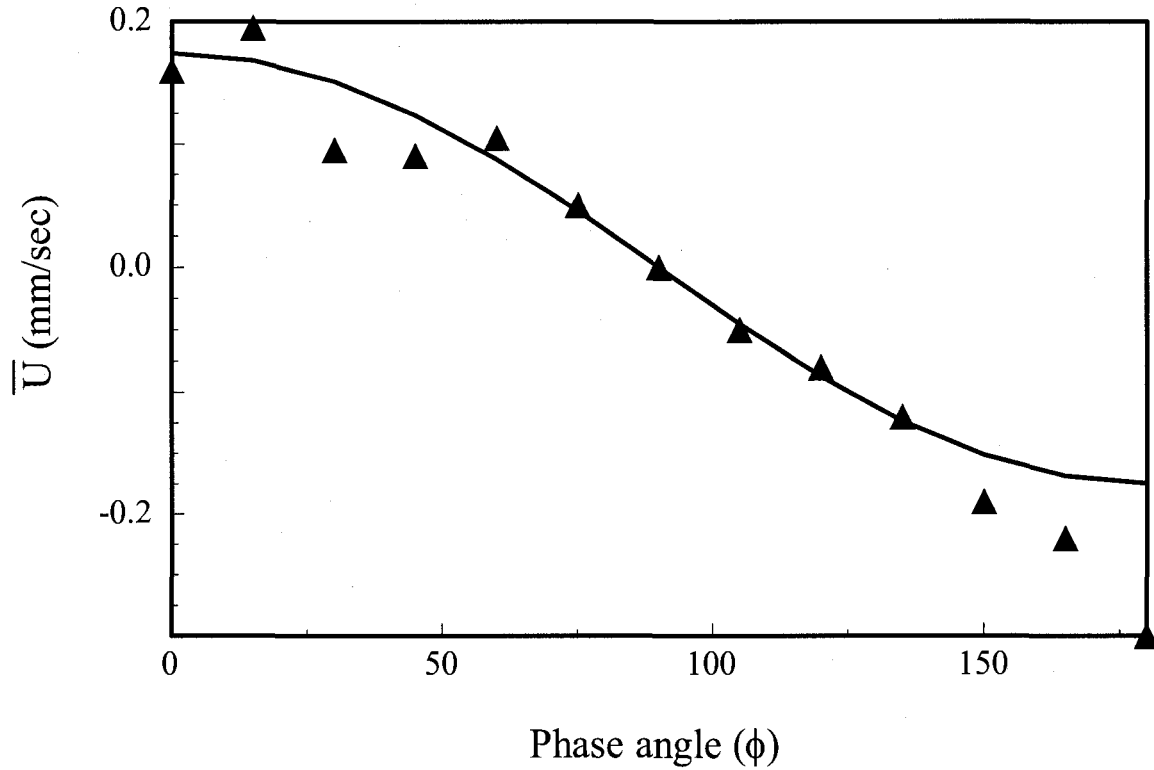


Figure 3.12: The mean velocity as a function of the phase angle.

In order to study the effect of the phase angle on the time averaged velocity, a 3D surface displaying the time-averaged velocity as a function of both phase angle and applied current shall be plotted. Figure. 3.13 shows this graph, where it can be clearly realized that the flow drops to zero at the angles -90 and 90 or when the current is zero.

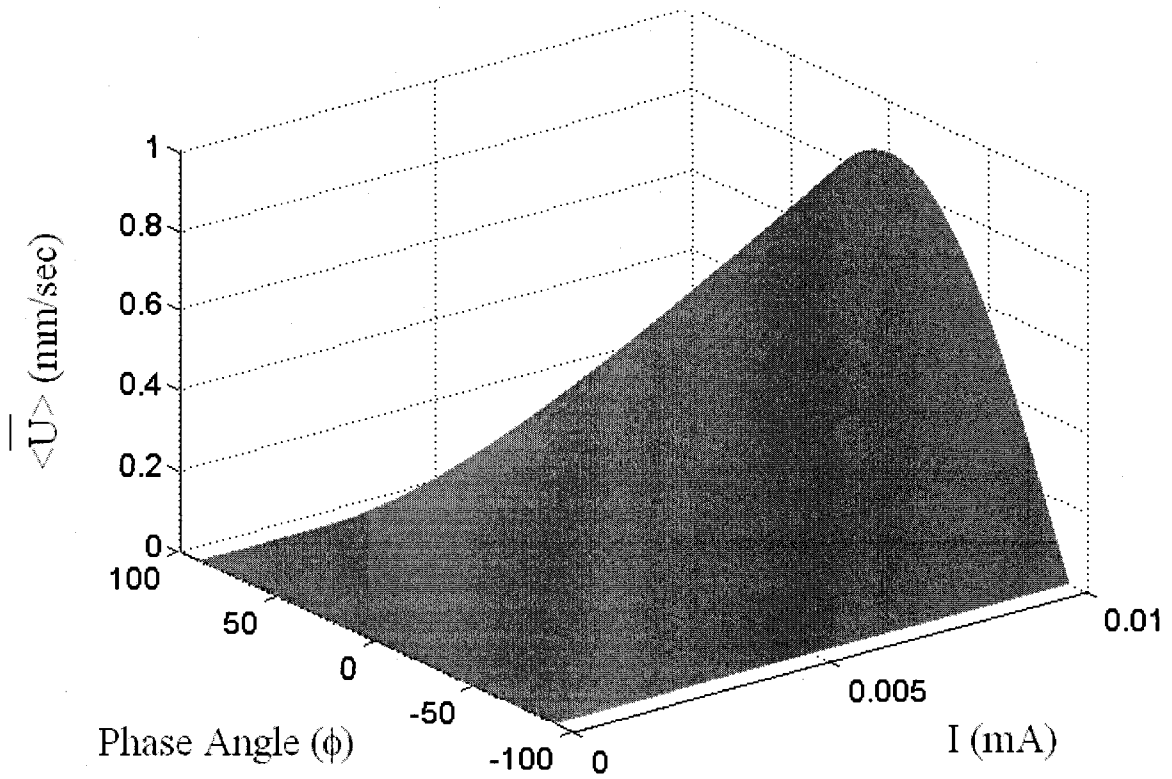


Figure 3.13: The time averaged velocity as function of phase angle and current

When the phase angle is fixed, the time-averaged velocity increases linearly with the applied current. On the other hand, when the current is fixed, it acquires a sinusoidal form as the phase angle changes. It is important to mention other physical quantities, which are given as: 0.44 T magnetic field and 0.001 Pa.s solution viscosity. The dimensions of the channel are: 500  $\mu\text{m}$  in width and height and 45 mm length.  $\Delta P$  is considered zero in this plot.

Another important plot to observe is the relationship between the  $\Delta P$  and the phase angle and their effect on the flow rate. In this scenario, those quantities are plot in a 3D surface, shown in figure 3.14. Dimensions and physical quantities are the same as above, with one addition i.e. the current is 10 mA. It is clear that the flow is equal to zero

when  $\Delta P$  and the phase angle are  $\pm 90$  or when  $\Delta P$  balances the Lorentz force per unit area of the electrode as shown in (24):

$$\Delta P = -\frac{I \times B}{H} \cos(\phi) \quad (24)$$

Notice that the time-averaged velocity increases with increase in the pressure drop.

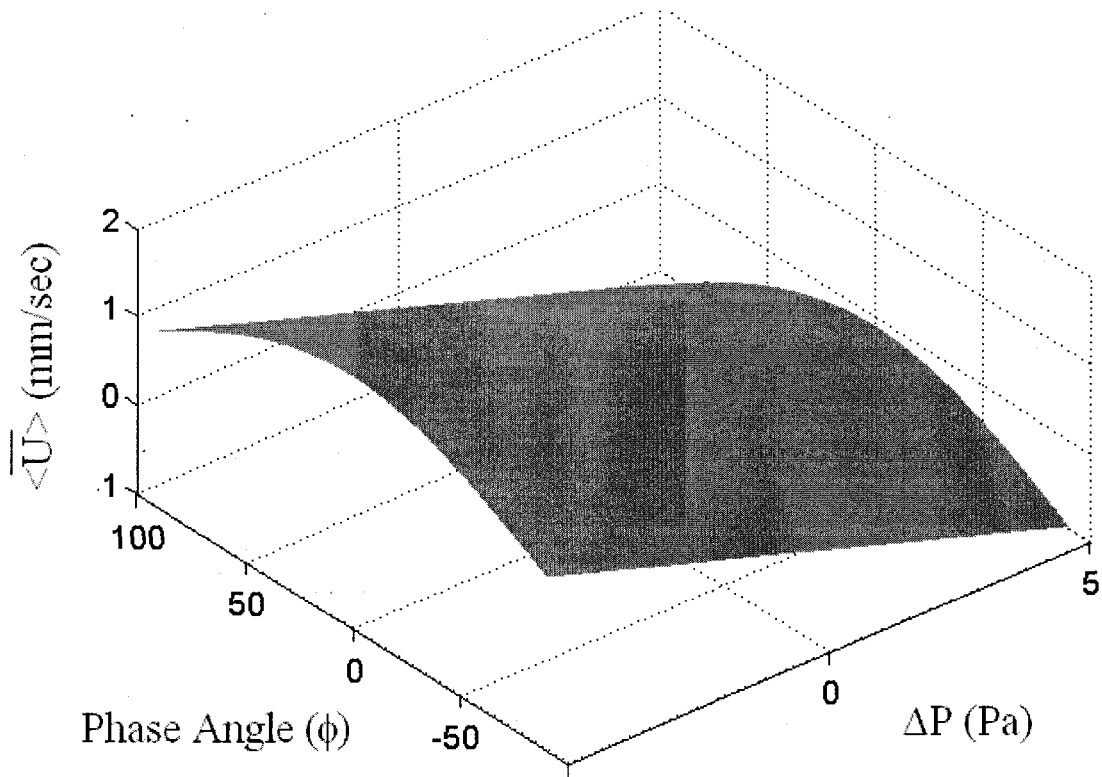


Figure 3.14: The time averaged velocity as function of phase angle and pressure drop

## CHAPTER 4

### ADHESION PROPERTIES OF NANOPOROUS ALUMINA FILMS

#### 4.1 Abstract

In this chapter, the adhesion properties of thin film nanoporous alumina substrates are investigated. Such substrates are important for the low-cost implementation of large arrays of semiconductor and metal nanostructures with applications ranging from electro-optic modulators to infrared detectors and mainly Lab on a Chip. For all such applications, an important requirement is good template/substrate adhesion.

As it was discussed in the previous chapters, I tried to implement the concepts deduced for micro channels on nano channels. I tried to initiate a MHD flow within a nanopore but as well known, there are no published method to create a single nanopore. So, I decided to use the AFM machine to create a single nanopore on AAO substrate. Gold layer was deposited over the substrate. The idea was to create a single punch in the substrate thus removing the gold layer and revealing only a single nanopore. Upon doing this, the substrate was not able to withstand the huge force exerted on it and it broke. I decided to study the adhesive properties of those substrates so I can manufacture a new substrate that can resist high normal and adhesive forces.



## 4.2 Introduction

Nanotechnology has become one of the most promising fields in modern technology. Its importance lies in the fact that it can handle applications that need high reliability and must be minute and small. Based on those facts the nanotechnology can deal with nanosized particles such as electrons, photons, DNA, and even RNA (Nielsch et al, 2000; Liu et al, 2003; Nishio et al, 2004).

Nanopores are the small pores that range between few to 500 nm in size. Those pores have electrically insulating membranes; thus, it can be used as a detector for small particles. If any electrolyte solution passes through those nanopores: the ionic current of any electrolyte solution passing through it is monitored as a voltage difference (Masuda et al, 1995, Masuda et al, 1997, Masuda et al, 1998). Different nanopores are fabricated on different substrates such as: silicon substrates, gallium oxide substrates, and alumina substrates.

Anodic alumina substrates have very good characteristics as both a template and host structures for the fabrication and manufacturing of different nanostructures and devices such as electronic, photonic, and magnetic nanosensors. Alumina substrates have hexagonal structures, in which the central pore is normal to the substrate. The advantages of alumina substrates over any other substrates are: they are easy to manufacture and prepare since the anodization setup isn't that complicated to build, the nanopores are distributed uniformly over the whole substrate, relatively inexpensive to manufacture, and different materials can be deposited into the nanopore.

Any aluminum substrate when electrochemically oxidized under constant potential difference, the surface of the aluminum layer will be covered by a fine nanoporous oxide layer. Fig.4.1 shows the alumina substrate after anodization.

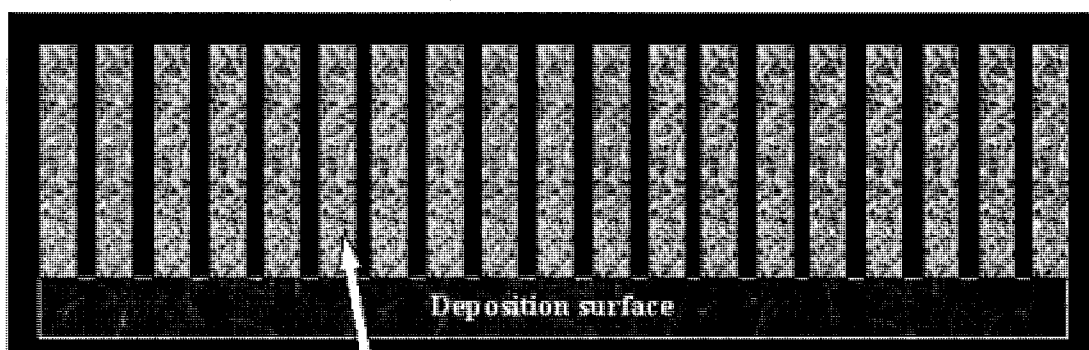


Figure 4.1: Alumina thin film after anodiation

Mild anodization (MA) was used to fabricate self ordered anodic aluminum oxide (AAO) (Martin et al, 1944 ; Masuada et al, 1995; Masuada et al, 1997; Li et al, 1998; Nicewarner-Pena et al, 2001; Lee et al; 2002). The draw back of MA is that it is relatively slow, expensive, and difficult to be built. A new and better alternative for MA is hard anodization (HA) (Lichtenberger-Bajza et al, 1960; Csokan et al, 1962). It is a very fast process that gives uniform distribution and dimensions for the nanopores and it increases some of the mechanical properties of the substrate under study. The HA process is performed under certain conditions: low temperature (chillers to cool the acid must be used), high potential difference applied across the electrodes, and the use of special acids (Murphy et al, 1961; Takahashi et al, 1973; Furneaux et al, 1989; Li et al, 2006).

The difference between MA and HA is that the nanopores in MA are self-ordered but it is slow and inconvenient process whilst in HA the nanopores are disordered but it is a fast and reliable process. Also, another important factor to take into consideration is the size of the nanopore. The importance of the size of the nanopore depends basically on the application itself. In HA the nanopores manufactured are relatively larger in diameter than those in MA.

To enhance the mechanical properties of AAO nanopores, new technique has been implemented (Parkhutik et al, 1992; Ostrowski et al, 1999; Xia et al, 2004; Habazaki et al, 2004; Zhu et al, 2005; Gras et al, 2006; Garcia-Vergara et al, 2007). It was found that changing the applied potential and the acid used will change the distribution and dimensions of the nanopores. Changing those two variables will lead to the change in the mechanical properties of the substrate under study and finally changing the mechanical property of any substrate will change the classification of each sample and its area of application.

In this work, an apparatus for anodizing alumina substrate will be presented and the effect of different contributing variables on the adhesive properties of the substrate will be further studied.

#### 4.3 Preliminary Work

The main idea behind this work was to create a single nanopore to detect the presence of DNA in any given solution. The idea was to use MHD to circulate the solution within this channel. AAO substrates were used. The substrate is covered with a thin layer of gold. Then, by the aid of atomic force microscope, a punch will be created

on the gold surface thus creating a single nanopore. The atomic force microscope used is PSIA XE100. This XE system is combination of atomic force microscope, scanning probe microscope, and scanning tunneling microscope. The resolution of the system is 1 micron. Figure 4.2 shows the PSIA XE100.

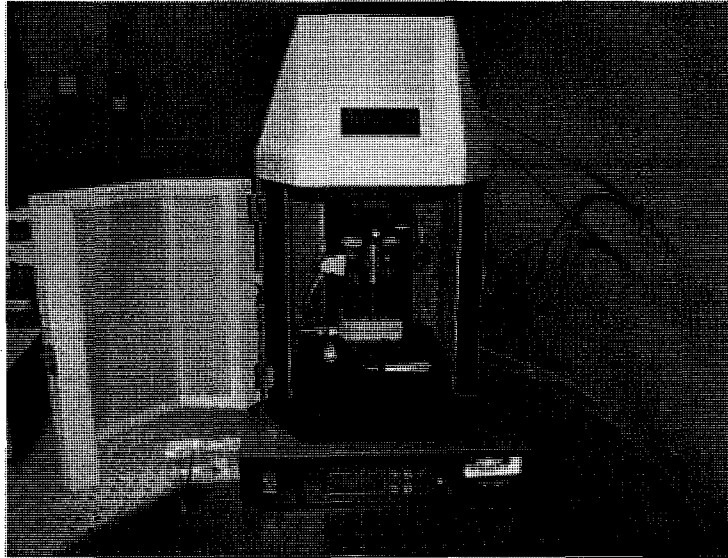


Figure 4.2: The PSIA XE100 system.

It was found out that the substrate used was not able to withstand the force exerted on it by the XE100 machine. Figure 4.3 shows the crack created over the substrate. Thus, I decided to do a study on the way to enhance the adhesive properties of AAO substrates so it can withstand forces created by the XE100. Figure 4.3 shows an example of the crack made by the XE100 on the samples.

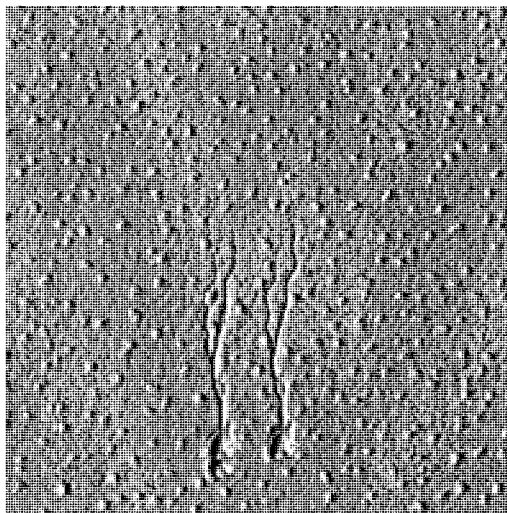


Figure 4.3: A cracked Substrate sample

#### 4.4 Experimental Procedure

First of all, the alumina substrate must be dipped in distilled water beaker as to make sure that all the impurities are washed away. The anodization apparatus is quiet easy and inexpensive to build. Figure 4.4. shows a schematic of the anodizing apparatus that has been built.

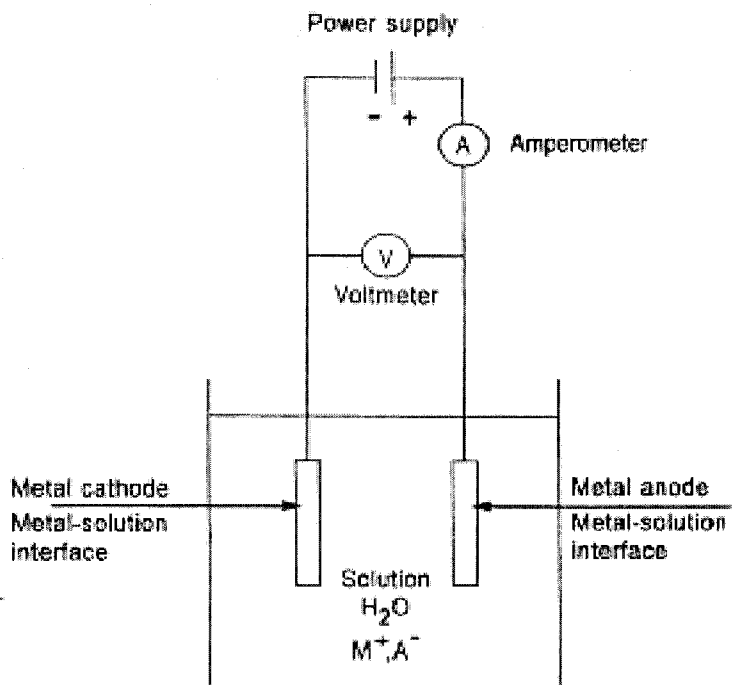


Figure 4.4: The anodization setup used

Fig. 4.5 shows the anodization apparatus used throughout this paper. A beaker filled with acidic solution is cooled by the aid of a chiller. Two pairs of electrode is dipped in this beaker. A platinum substrate is installed on the cathode and the substrate to be ionized on the anode. Both sides are connected to power supply. The current is monitored with the aid of the LabVIEW software.

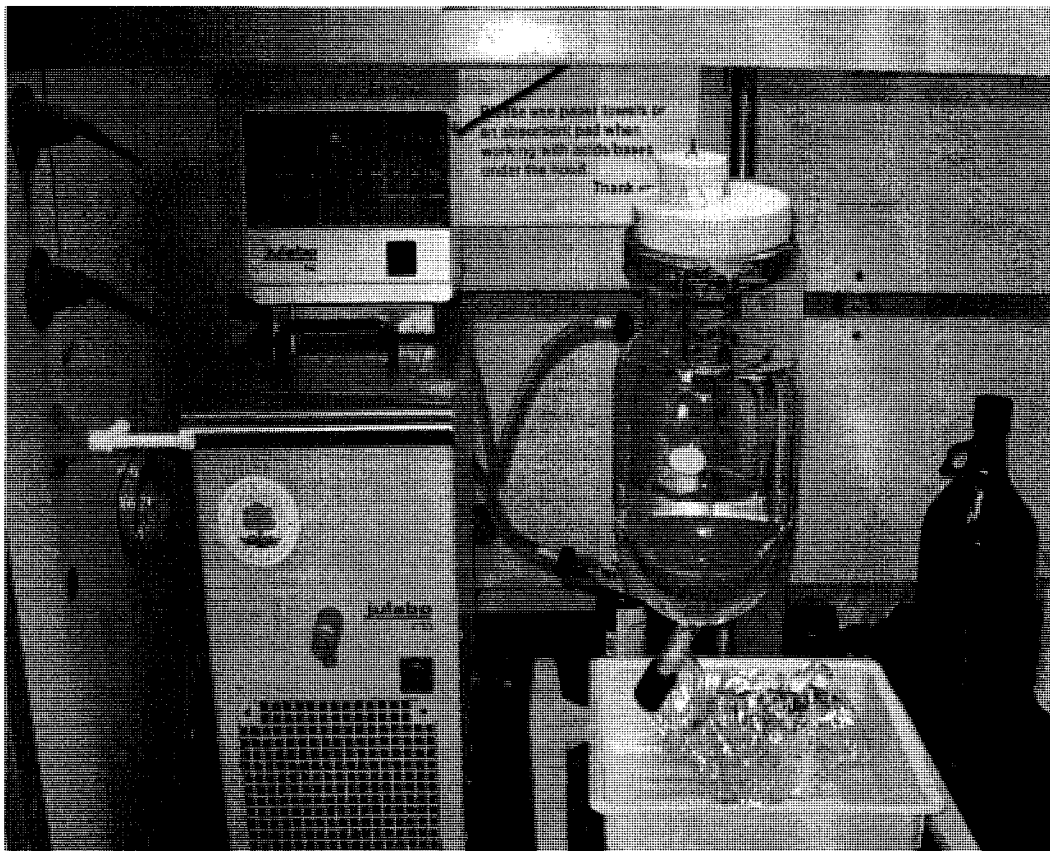


Figure 4.5: The anodization apparatus used throughout this paper

The power supply in use can give a voltage up to 180 V. The power supply is manufactured by Keithley and it is highly reliable power supply with a relative error in reading of 1%. Fig. 4.6 will show this power supply.



Figure 4.6: The power supply used to anodize the alumina substrate

An alumina sample must be placed on the anode and a platinum substrate is placed in the cathode. Both electrodes are depicted in a beaker filled with acid. The acid varies from oxalic to phosphoric to sulfuric, etc. The alumina substrate to be anodized is a square with a side length of 1 cm. Also, the platinum substrate is a square with same dimensions. The electrodes are connected to a power supply that will supply a constant voltage. This voltage varies from 30V to 120V based on the acid used. The acid must be maintained at room temperature so a chiller must be installed. The chiller will aid in cooling the acid within the apparatus by convection means (Jessenky et al 1998, Haruyama et al 2001, Zhou et al 2001, and Choi et al 2003).



#### 4.5 Scratch Test Procedure

To investigate the adhesive properties of the alumina thin films, scratch tests were performed using a nano-scratch tester instrument manufactured by Micro photonics Inc. The scratch test is carried out by the generation of scratches on the film surface using a spherical stylus (Rockwell C Diamond, tip radius 2  $\mu\text{m}$ ). The stylus is drawn at a constant speed across the sample under either constant or progressive loading at a fixed rate. For progressive loading, the smallest load at which appreciable failure occurs on the sample is called the critical load. For constant loading, the critical load corresponds to the load at which a regular occurrence of such failure is observed along the track. Scratch test is basically a comparison test and the critical load depends on the mechanical strength (adhesion and cohesion) of a coating to the substrate. The critical load depends on parameters that might be directly related to the test itself like the loading rate, scratching speed and indenter tip radius, indenter material. It also depends on the coating substrate parameters that include the substrate hardness and roughness, coating thickness and roughness, friction coefficient between coating and indenter and internal stresses in the coating. A scanning force microscopy is used to obtain high resolution images in three dimensions and the quantitative lateral and depth measurements can be obtained in the scratched portions. These images can be used to investigate the surface morphology and roughness before and after the tests. The tangential force recording enables the measurement of variations in force fluctuation along the scratch path. The pre-scan recording on the sample is done to include the effects of non-uniformity in sample flatness, where the penetration depth is measured during the test. The post scan reveals the elastic recovery of the coating-substrate residue by providing the scratch path profile.

#### 4.6 Results and Discussion

During anodization (while maintaining a constant current), the voltage across the electrodes will increase from zero to a peak. Then, it will drop slightly since the ions within the acidic solution are consuming this voltage to anodize the alumina layer. Then the process continues until the outer layer of alumina is completely anodized. After that a potential difference will be built between the opposite electrodes.

This phenomenon is studied in fig. 4.5. Three different samples are considered. We are going to use the same acid (phosphoric acid with 5% concentration). Three different current values are going to be considered: 10 mA (represented by the dotted line), 25 mA (represented by the dashed line), and 36 mA (represented by the solid line). The voltage change across the electrodes is plotted vs time. It is clear that as the current increases, the substrate will be anodized faster. The current flowing through the acidic solution will enhance its ionization. The more ions we have in the solution, the more efficient the anodization process will be. It is clear that as the current increases, the anodization process will be more rapid. Also, as the current increases, the peak of the voltage will be higher. This is due to Ohm's first law which states that the voltage and current are directly proportional. Thus, it is clear that as we decrease the current, the time to anodize the substrate will increase. Obviously, as time increases, the mechanical properties of the substrate will be enhanced. Based on this, it could be said that to enhance the substrate's resistivity to adhesive forces then we should use high current values.

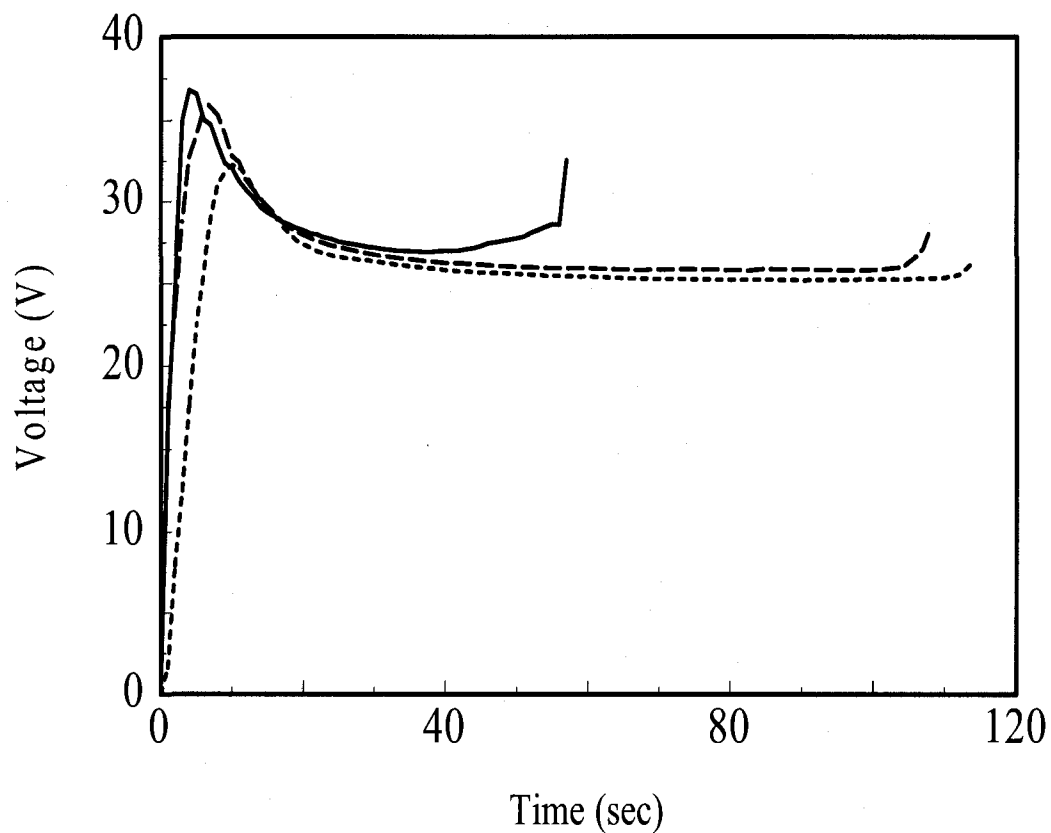


Figure 4.7: The potential difference across the electrodes

To further investigate the effect of both the current applied and the acid used in anodization and on the adhesive properties of the materials, I did nine different tests with nine different scenarios. Table 4.1 shows these scenarios, the numbers represent the scenario number.

Table 4.1: The nine different scenarios to be studied

	10 mA	25 mA	36 mA
Oxalic Acid	1	2	3
Phosphoric acid	4	5	6
Sulfuric Acid	7	8	9

After anodization, the samples were sent out to be tested. The test setup is described above. Figure 4.8 shows the principle behind the testing apparatus.

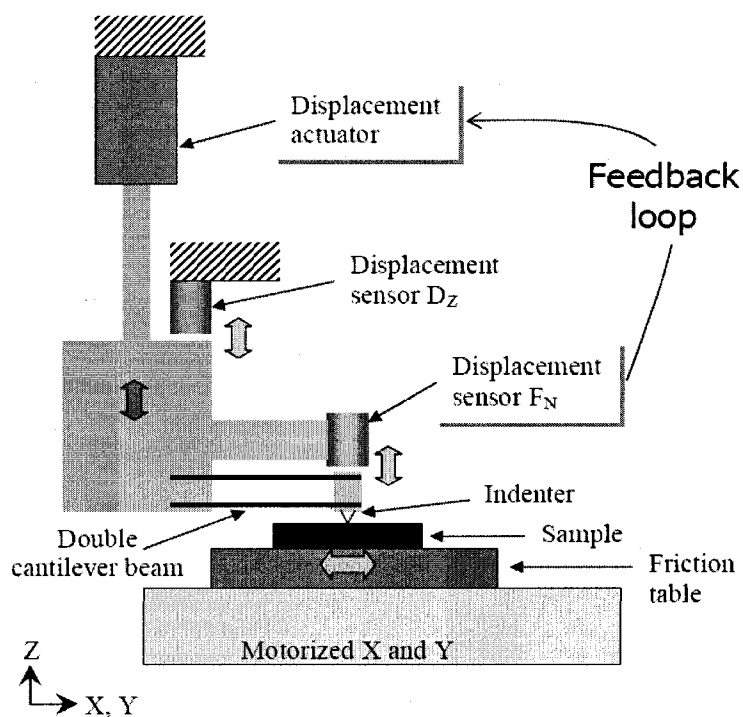


Figure 4.8: The principle behind the testing apparatus.

Table 4.2 shows the limiting force at which the sample failed. The numbers represents the average magnitude of the force and the standard deviation as well.

Table 4.2: The ultimate force corresponding to different scenarios

Sample	Failure (mN)
1	464.7
2	587.2
3	591.2
4	716.9
5	528.2
6	572.7
7	389.4
8	350.1
9	355.6

Figure 4.9 to figure 4.17 show the scratch test results for the first scenario. The normal force, frictional force, and penetration depth is plotted versus the scratch length and the force applied. The vertical line in the middle represents the length at which the failure occurs.

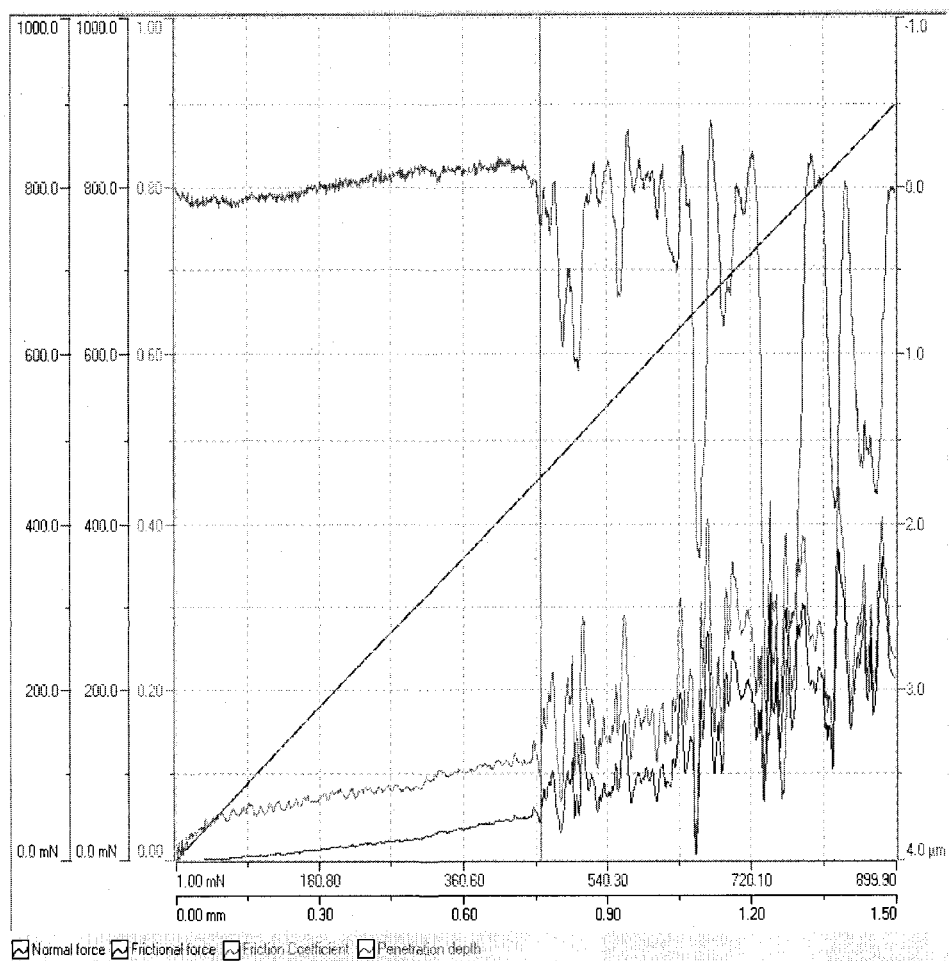


Fig 4.9: The first sample adhesive test results

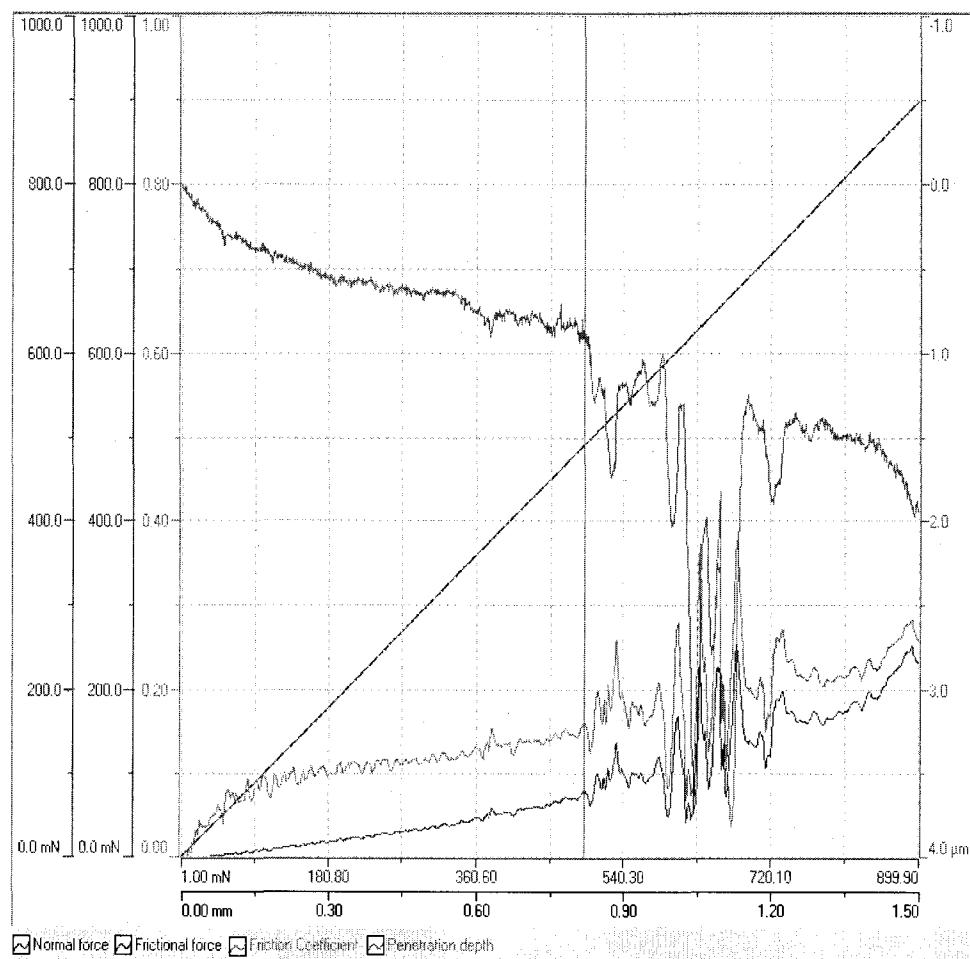


Fig 4.10: The second sample adhesive test results

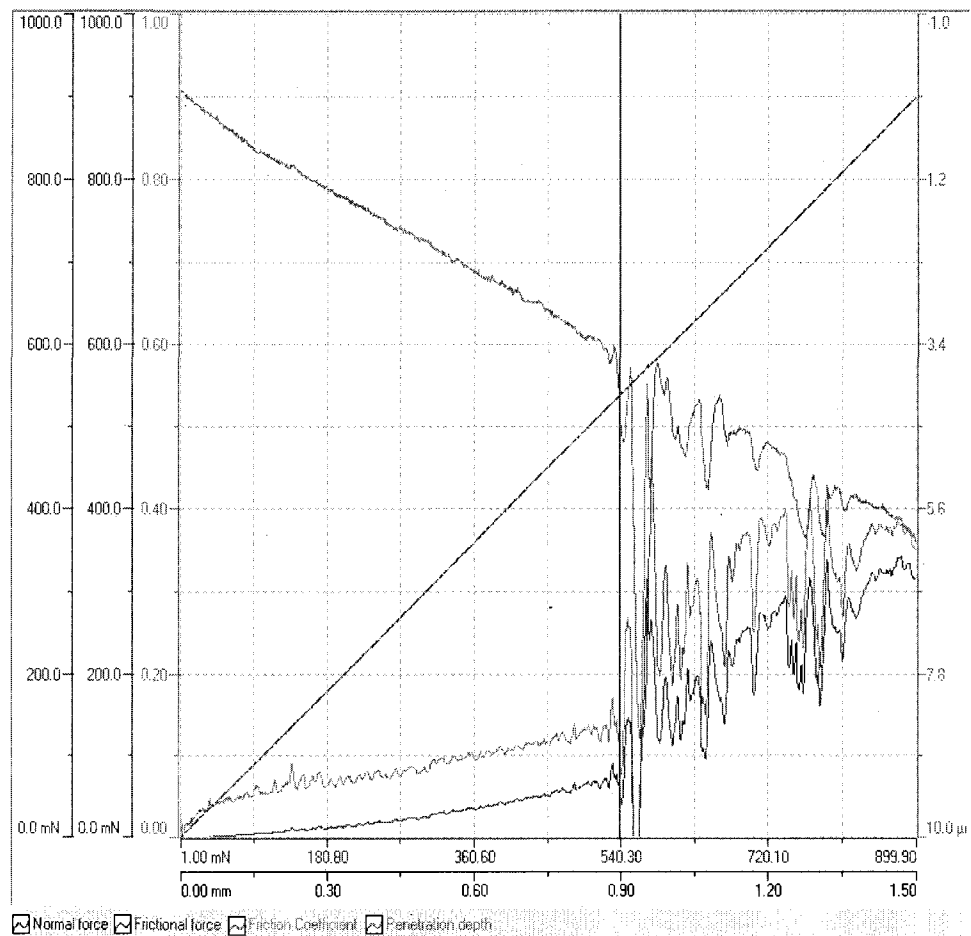


Fig 4.11: The third sample adhesive test results



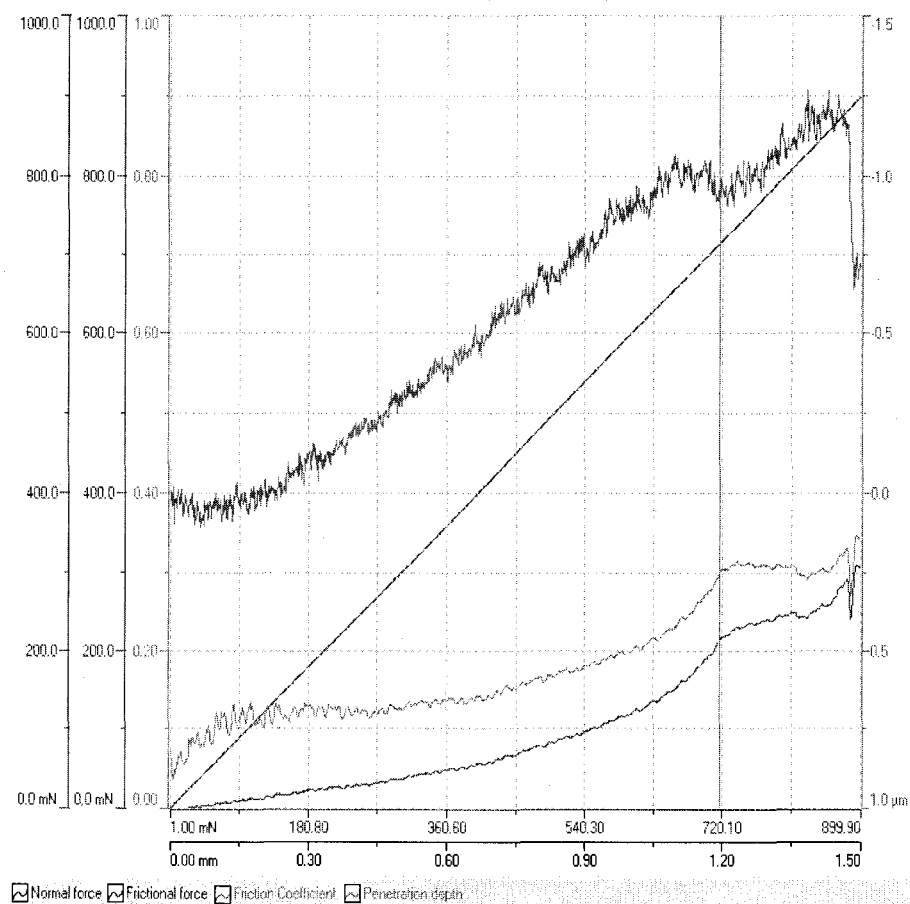


Fig 4.12: The fourth sample adhesive test results

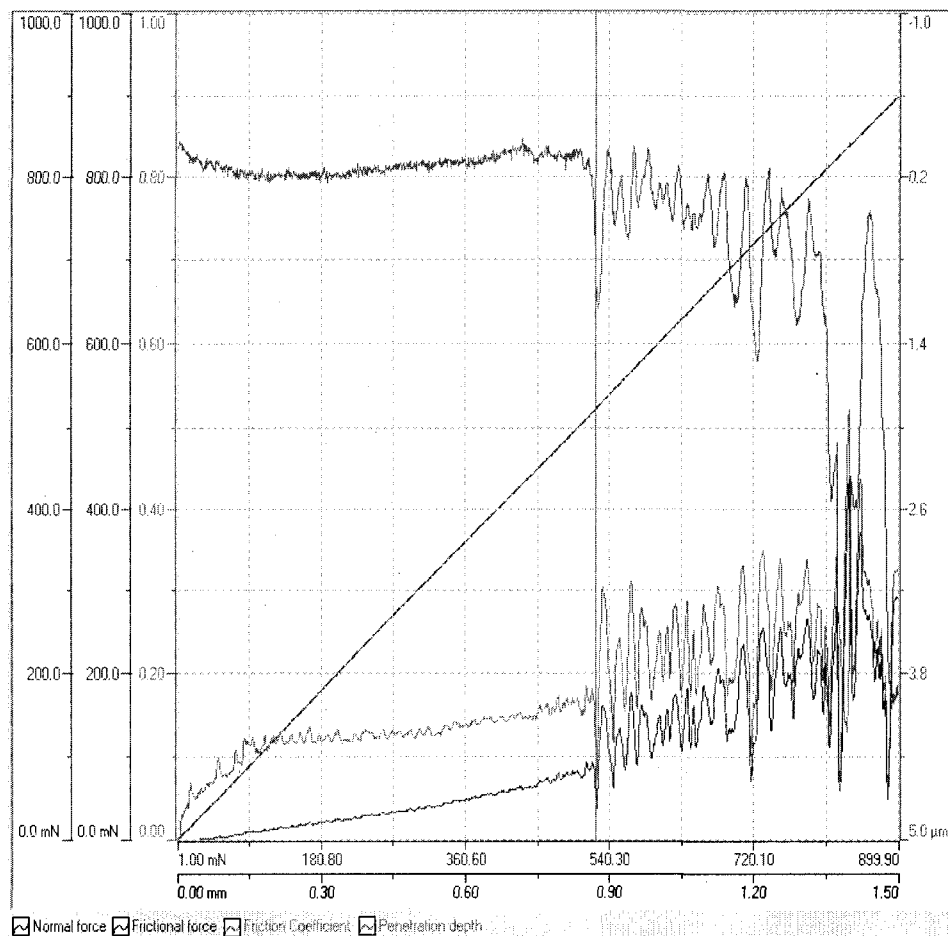


Fig 4.13: The fifth sample adhesive test results

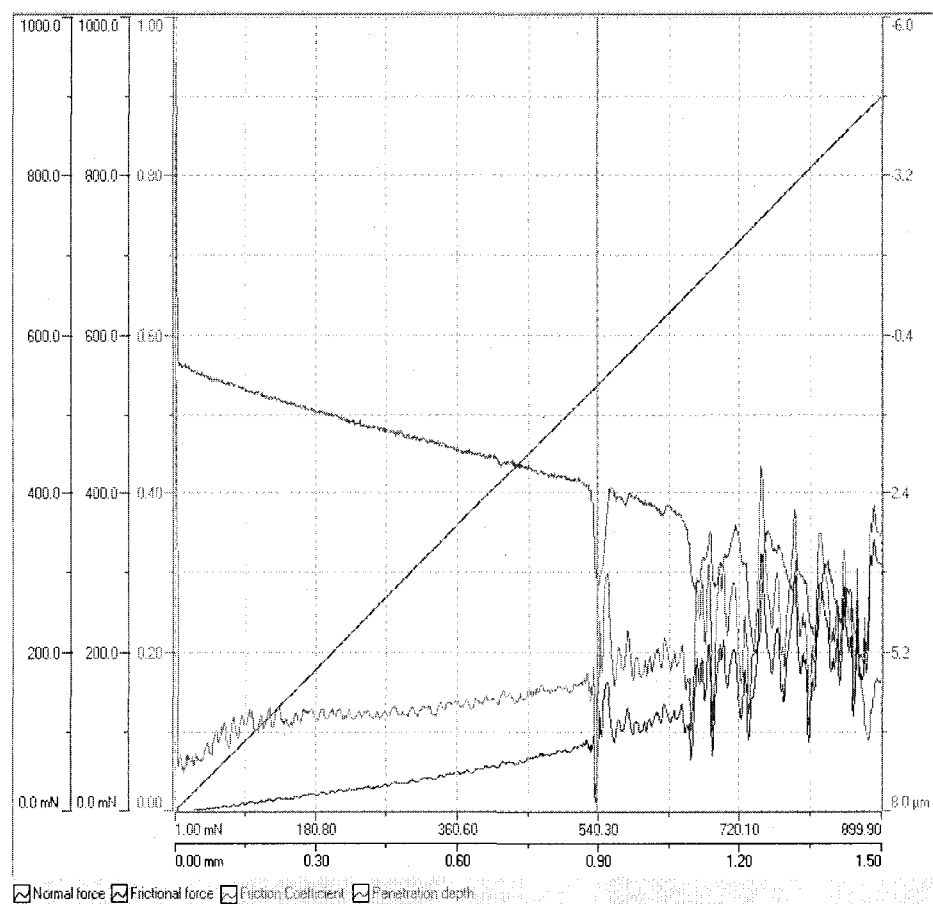


Fig 4.14: The sixth sample adhesive test results

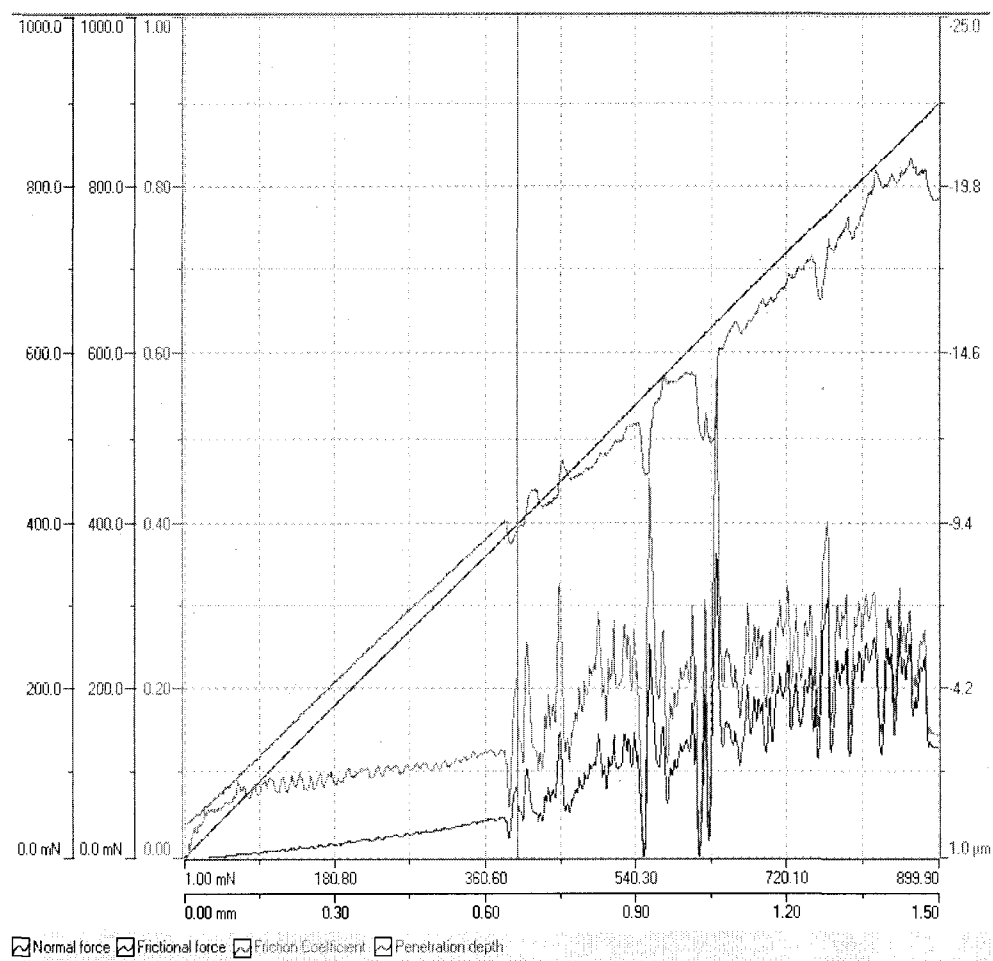


Fig 4.15: The seventh sample adhesive test results

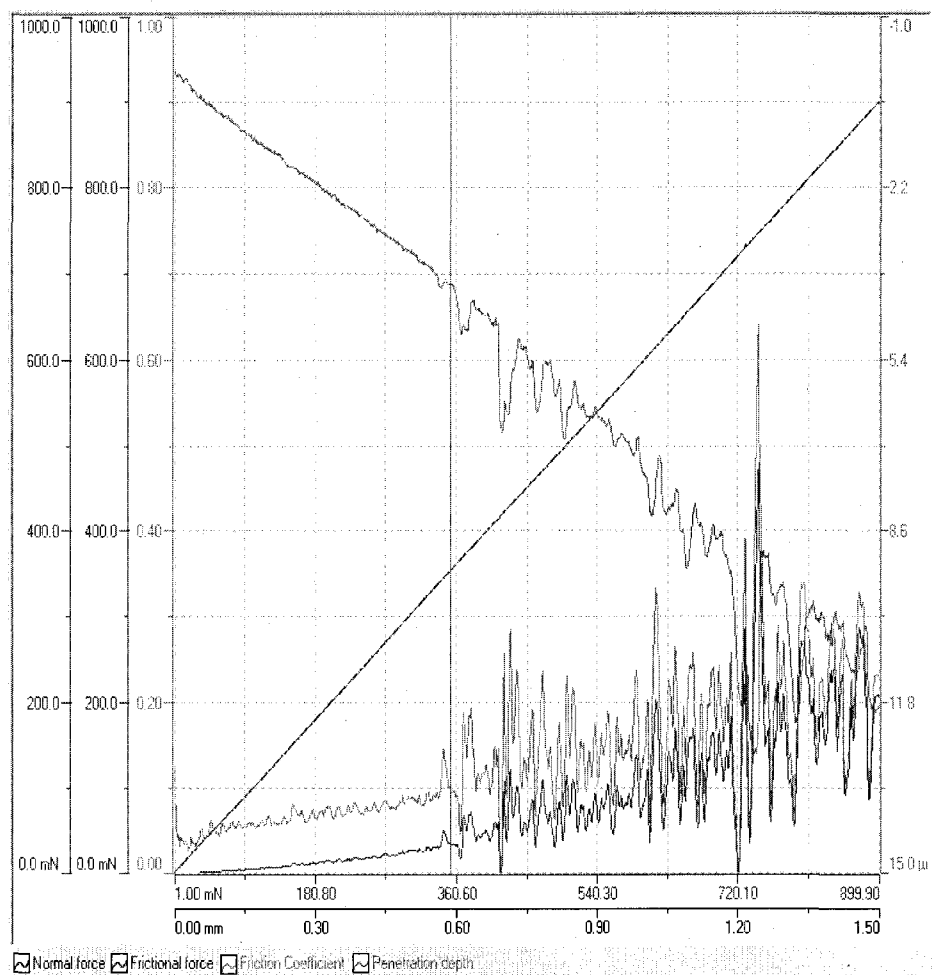


Fig 4.16: The eighth sample adhesive test results

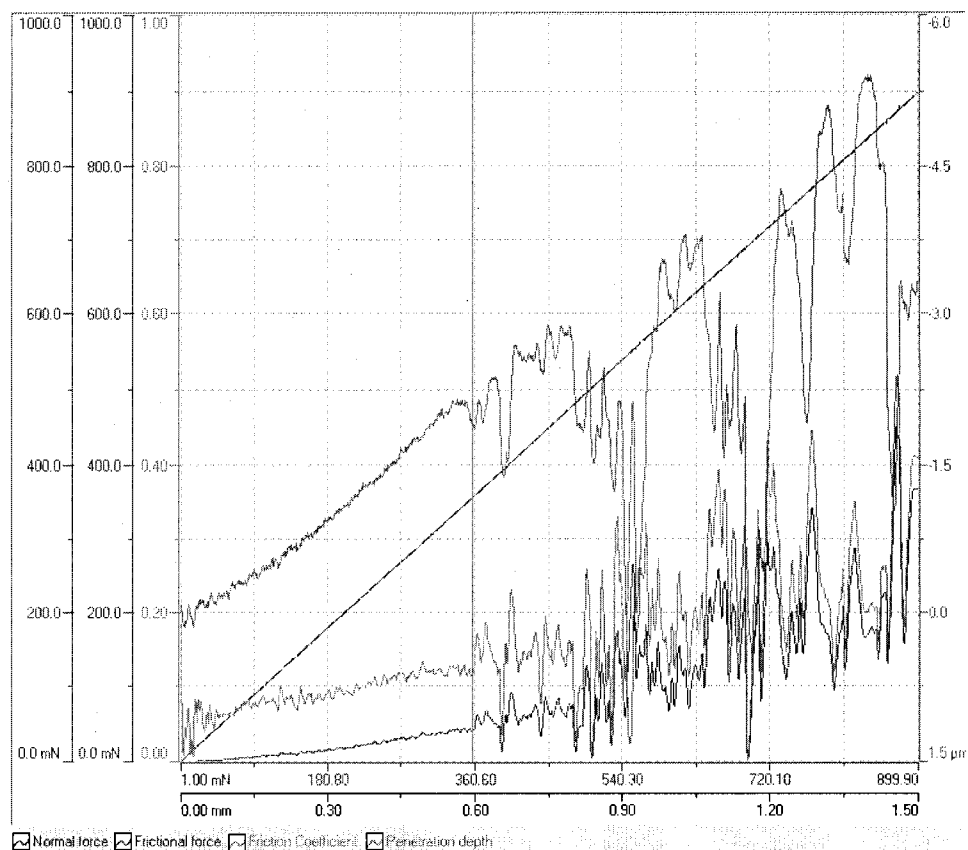


Fig 4.17: The ninth sample adhesive test results

It is clear from the above figures and from table 4.2 that for the same acid used, as the current increases then the substrate will have higher adhesive properties. This is because as the current increases, the electrons available to anodization are more.

Also, for the same applied current, it is clear that oxalic acid is the best choice for anodization as to improve the adhesive properties of AAO samples. This is because the chemical structure of oxalic acid allows the electrons to be transferred on higher rates. Scenario four doesn't seem to be a bad sample so no information can be deduced from it.

## CHAPTER 5

### CONCLUSIONS AND FUTURE WORK

LOC is a promising technology. Its applications are traced in different fields: chemical, mechanical, bioengineering, and sensor development. Its importance lies in the fact that: it is convenient, efficient, inexpensive, easily operated, and highly reliable.

Despite of these advantages, LOC technology faces two important drawbacks. These drawbacks could greatly retard any advancement in this field.

Initiating a flow in microchannels is one of these drawbacks since a massive pressure gradient is required. One of the means used to create such a pressure gradient is RedOx MHD. Many researches tried to model the RedOx MHD mathematically. In the presented research, the 3D RedOx model was discussed and analyzed. A full mathematical model was investigated and the inter relationship between different physical variables is studied. Also, a closed form solution that relates the mean velocity to the different physical quantities and to the dimensions of the channel was derived. This closed form solution will be a vital tool for designers in the future. In addition to the above, the material used in the fabrication of the LOC must be highly reliable and can resist huge forces especially in nano channels. Anodized nanoporous alumina substrate is one of these materials. In this dissertation, a study of its adhesive properties was



performed. The different variables that contribute in the fabrication and anodizing process are further investigated. The contribution of these materials to the adhesive forces is mentioned.

## 5.1 Conclusions

In this dissertation, many important conclusions were drawn. Those conclusions are mentioned below:

When the applied potential difference is low, the resulting current transmitted through the electrolyte nonlinearly increases with the potential difference. Once the potential difference exceeds a certain value, the current reaches the value of the limiting current and becomes saturated. The magnitude of the limiting current is, among other things, a function of the concentration of the RedOx species, strength of the magnetic flux density, the dimensions of the electrodes and the channel, and the diffusion coefficients of the electroactive species. The theoretical predictions of the full mathematical model agree with the experimental data obtained from the literature.

Similar to the relationship between the current and the potential difference, the averaged velocity of the induced MHD flow nonlinearly increases with the applied potential difference when the latter is low. Above a critical value, the fluid's motion is independent of the applied potential difference. It is desirable to maintain a potential difference close to the critical value so as to maximize the flow rate.

Also, the average velocity linearly increases with the increase of the current for different concentrations of the RedOx species, various magnetic flux densities, and dimensions of the channel.

When the concentration of the RedOx species is low, the effect of the magnetic flux density on the limiting current is insignificant. For higher concentration of the RedOx species, the limiting current increases with the magnetic flux density.

As the magnetic flux density increases, the induced flow increases due to the enhancement of both the Lorentz force and the resulting current. For low concentration of the RedOx species, the average velocity corresponding to the limiting current linearly increases with the magnetic flux density. For higher concentration of the RedOx species, the maximum average velocity nonlinearly increases with the magnetic flux density.

For the same physical conditions and for negligible pressure drops, the mean velocity will increase aggressively as the aspect ratio increase until it reaches the maximum corresponding to aspect ratio of one then it will decline slowly as the aspect ratio increases.

When there is a pressure drop, the flow will increase as  $I$  and  $\Delta P$  increases. The increase wrt  $I$  is more rapid than the increase wrt to  $\Delta P$ . The flow will be zero subjected to the relation presented in (23).

In AC MHD flows, the time averaged velocity will increase as the pressure drop increase whilst it will have a sinusoidal form when the phase angle changes. The flow will drop to zero when correlation (24) is valid.

It is important to mention that the closed form solution presented will be useful for the design and optimization of both AC and DC MHD microfluidic devices. Moreover, the model allows one to test quickly and cheaply the effects of all contributing parameters and operating conditions on device's performance. Also, it will reduce the time for numerical analysis since there will be no need to solve for the

differential Navier Stoke's equation.

AAO nano channels were studied thoroughly as well. Those conclusions about its adhesive properties were drawn:

It was found out that as the anodizing current increases the AAO will tend to have higher adhesive properties. Also, it was found out that oxalic acid is the best acid to enhance the strength of the AAO substrate.

## 5.2 Future Work

Despite all the advantages of RedOx MHD, there are still some problems in it. One of them is the bubble creation under high current flows. This occurs due to the fact that the electrolyte solution within the channel will go through intensive electrolysis process and thus bubbles will be created. Bubble creation will retard the flow within the channel. The other one is the corrosion of the electrodes installed within the channel.

Also, in some LOC applications two phase flow will be encountered such as circulating a blood sample within a microchannel. Knowing that the physical properties of blood are different from that of the electrolyte solution, it will be of great importance to study the effect of RedOx MHD on two phase flow. A 3D RedOx MHD mathematical model must be developed for this kind of flow. The flow must be studied in depth and different contributing parameters should be investigated. In addition to that, an intensive design procedure for RedOx MHD micropumps must be developed. The new design must take into consideration the results presented previously.

The adhesive properties of Anodized alumina substrate play an important role in the manufacturing of any LOC. After studying those properties and their relationship with the contributing variables in the anodization setup, a highly reliable LOC with strong adhesion properties must be designed. A single nanopore should be manufactured on a strong substrate that can resist adhesive and normal forces.

This single nanopore must be charged and it must be used as a DNA detection sensor. DNA samples will be circulated through those substrates and since both the substrate and the DNA are charged, any increase in current flow between opposite sides of the channel will be detected. As a result DNA presence will be detected.

## REFERENCES

1. Affani A. and Chiorboli G., 2006, Numerical Modeling and Experimental Study of an ac Magnetohydrodynamic Micropump, 2006 Instrumentation and Measurement Technology Conference, Sorrento, Italy
2. Aguilar Z., Arumugam P., and Fritsch I., 2006, Study of magnetohydrodynamic driven flow through LTCC channel with self-contained electrodes, J. Electroanalytical Chemistry, 591, 201
3. Anderson E. C. and Fritsch I., 2006, Factors Influencing RedOx magnetohydrodynamics-induced convection for enhancement of stripping analysis, Analytical Chemistry 78, 3745
4. Arrowsmith, D.J., Clifford, A.W., Moth, D.A., 1986, Fracture of anodic oxide formed on aluminium in sulphuric acid, Journal of Materials Science Letters, 5 (9), pp. 921-922
5. Arumugam P. U., Belle A. J., and Fritsch I., 2004, Inducing convection in solutions on a small scale: Electrochemistry at microelectrodes embedded in permanent magnets, IEEE Transactions on Magnetics, 40, 3063
6. Arumugam P. U., Clark E.A., and Fritsch I., 2005, Use of paired, bonded NdFeBmagnets in RedOx magnetohydrodynamics, Analytical Chemistry 77, 1167
7. Arumugam P. U., Fakunle E.S., Anderson E.C., Evans S.R., King K.G., Aguilar Z.P., Carter C.S., and Fritsch I., 2006, RedOx magnetohydrodynamics in Microfluidic Channel: Characterization and Pumping, J. Electrochem. Soc., 153, pp. E 185

8. Bard A. J. and Faulkner L. R., 2000, *Electrochemical Methods, Fundamentals and Applications*, 2nd ed. (John Wiley and Sons, Englewood Cliffs, NJ)
9. Bau H.H., Zhong J., and Yi M., 2001, A minute magneto hydro dynamic (MHD) mixer, *Sens. Actuators B* 79, 205
10. Bau H.H., Zhu J., Qian S., and Xiang Y., 2002, A magneto-hydrodynamic micro fluidic network, in *Proceedings ASME International Mechanical Engineering Congress & Exposition* (New Orleans, Louisiana, 2002), 33559.
11. Bau H. H., 2001, A case for magneto-hydrodynamics (MHD), in *IMECE Symposium Proceedings* (New York), 23884.
12. Bau H.H., Zhu J., Qian S., and Xiang Y., 2003, A magneto-hydrodynamically controlled fluidic network, *Sensors and Actuators B* 88, 207
13. Boedicker J. Q., Li L., Kline T. R. and Ismagilov R. F., 2008, Detecting bacteria and determining their susceptibility to antibiotics by stochastic confinement in nanoliter droplets using plug-based microfluidics, *Lab Chip*, 8, 1265
14. Bortels L., Van den Bossche B., Deconinck J., Vandeputte S., and Hubin A., 1997, Analytical solution for the steady-state diffusion and migration involving multiple reacting ions: Application to the identification of Butler-Volmer kinetic parameters for the ferri-/ferrocyanide redox couple, *J. Electroanalytical Chemistry* 429, 139
15. Boum G.B. and Alemany A., 1999, Numerical simulations of electrochemical mass transfer in electromagnetically forced channel flows, *Electrochimica Acta*, Volume 44, pp. 1749-1760(12)
16. Cabrera, N., Mott, N.F., 1949, Theory of the oxidation of metals, *Reports on Progress in Physics*, 12 (1), art. no. 308, pp. 163-184

17. Carlo D.D., Jeong K.H. and Lee L.K., 2003, Reagentless mechanical cell lysis by nanoscale barbs in microchannels for sample preparation, *Lab Chip*, **3**, 287
18. Chen J. Z., Darhuber A.A., Troian S.M. and Wagner S., 2004, Capacitive sensing of droplets for microfluidic devices based on thermocapillary actuation, *Lab Chip*, **4**, 473
19. Clark E. A. and Fritsch I., 2004, "Anodic stripping voltammetry enhancement by redox magnetohydrodynamics," *Anal. Chem.* **76**, 2415
20. Cheng, W., Wang, J., Jonas, U., Fytas, G., Stefanou, N., 2006, Observation and tuning of hypersonic bandgaps in colloidal crystals, *Nature Materials*, **5** (10), pp. 830-836
21. Chu, S.-Z., Wada, K., Inoue, S., Isogai, M., Yasumori, A., 2005, Fabrication of ideally ordered nanoporous alumina films and integrated alumina nanotubule arrays by high-field anodization, *Advanced Materials*, **17** (17), pp. 2115-2119
22. Csokán, P., Sc, C.C., 1962, Hard anodizing: Studies of the relation between anodizing conditions and the growth and properties of hard anodic oxide coatings, *Electroplat. Metal Finishing*, **15**, pp. 75-82
23. Davidson P. A., 2001, *An Introduction to Magnetohydrodynamics*, (Cambridge University Press, Cambridge).
24. Davidsson R., Genin F., Bengtsson M., Laurell T. and Emnéus J., 2004, Microfluidic biosensing systems Part I. Development and optimisation of enzymatic chemiluminescent  $\mu$ -biosensors based on silicon microchips *Lab Chip*, **4**, 481

25. Davidsson R., Johansson B., Passoth V., Bengtsson M., Laurell T. and Emnéus J., 2004, Microfluidic biosensing systems Part II. Monitoring the dynamic production of glucose and ethanol from microchip-immobilised yeast cells using enzymatic chemiluminescent  $\mu$ -biosensors, *Lab Chip*, 4, 488
26. Ebihara, K., Takahashi, H., Nagayama, M., 1983, Structure and density of anodic oxide films formed on aluminium in oxalic acid solutions, *J. Met. Finish. Soc. Jpn*, 34, pp. 548-554
27. Eijkel J.C.T., Dalton C., Hayden C.J., Burt J.P.H., and Manz A., 2003, A circular ac magnetohydrodynamic micropump for chromatographic application, *Sensors and Actuators B*, 92, 215-221
28. Eijkel J.C.T., Van den Berg A., and Manz A., 2004, Cyclic electrophoretic and chromatographic separation methods, *Electrophoresis* 25, 243
29. Furneaux, R.C., Rigby, W.R., Davidson, A.P., 1989, The formation of controlled-porosity membranes from anodically oxidized aluminium, *Nature*, 337 (6203), pp. 147-149
30. Galanina O. E., Mecklenburg M., Nifantiev N. E., Pazynina G. V. and Bovin N. V., 2003, GlycoChip: multiarray for the study of carbohydrate-binding proteins, *Lab Chip*, 3, 260
31. Gao Y.P., Wei W.Z., Gao X.H., Zhai X.R., Zeng J.X., and Yin J., 2007, A Novel Sensitive Method for the Determination of Cadmium and Lead Based on Magneto-Voltammetry, *Anal. Lett.*, 40, pp. 561



32. Garcia-Vergara, S.J., Skeldon, P., Thompson, G.E., Hashimoto, T., Habazaki, H., 2007, Compositional evidence for flow in anodic films on aluminum under high electric fields, *Journal of the Electrochemical Society*, 154 (9), pp. C540-C545
33. Georgiadou M., 2003, Modeling current density distribution in electrochemical systems, *Electrochimical Acta* 48, 4089
34. Ghaddar N. and Sawaya E., 2003, Testing and modeling thermosyphonic closed-loop magnetohydrodynamic electrolyte flow, *J. Thermophysics and Heat transfer*, 17, 129
35. Gleeson J.P., Roche O.M., West J., and Gelb A., 2004, Modeling annular micromixers, *SIAM J. Appl. Math.* 64, 1294
36. Gras R., Duvail J.L., Minea T., Dubose M., Tessier P.Y., Cagnon L., Coronel P., Tories J., 2006, Template Synthesis of Carbon Nanotubes from porous Alumina Matrix on Silicon, *Microelectronic Engineering* 83, 2432-2436
37. Habazaki, H., Konno, H., Shimizu, K., Nagata, S., Skeldon, P., Thompson, G.E., 2004, Incorporation of transition metal ions and oxygen generation during anodizing of aluminium alloys, *Corrosion Science*, 46 (8), pp. 2041-2053
38. Heule M. and Manz A., 2004, Sequential DNA hybridisation assays by fast micromixing, *Lab Chip*, 4, 506
39. Hofmann O., Niedermann P. and Manz A., 2001, Modular approach to fabrication of three-dimensional microchannel systems in PDMS—application to sheath flow microchips, *Lab Chip*, 1, 108
40. Ho J., 2006, Study the performance of MHD pump with the dimension of duct channel, Submitted to *Journal of Marine Science and Technology*

41. Ho J., 2007, Characteristic Study of MHD pump with Channel in Rectangular Ducts, J. Mar. Technol., 15, p. 466
42. Homsy A., Koster S., Eijkel J. C. T., Van Den Berg A., Lucklum F., Verpoorte E., and de Rooij N. F., 2005, A high current density DC magnetohydrodynamic (MHD) micropump, Lab on a Chip 5, 466
43. Homsy A., Linder V., Lucklum F., de Rooij N.F., 2007, Magnetohydrodynamic Pumping in Nuclear Magnetic Resonance Environments, Sens. Actuators B, 123, pp. 636
44. Hsu C.H., Chen C. and Folch A., 2004, "Microcanals" for micropipette access to single cells in microfluidic environments, Lab Chip, 4, 420
45. Hulme J. P., Mohr S., Goddard N. J. and Fielden P.R., 2002, Rapid prototyping for injection moulded integrated microfluidic devices and diffractive element arrays Lab Chip, 2, 203
46. Jang J. and Lee S.S., 2000, Theoretical and experimental study of MHD (Magnetohydrodynamic) micropump, Sens. Actuators A 80, 84
47. Jeong Y., Kim S., Chun K., Chang J. and Chung D.S., 2001, Methodology for miniaturized CE and insulation on a silicon substrate, Lab Chip, 1, 143
48. Jessensky, O., Müller, F., Gösele, U., 1998, Self-organized formation of hexagonal pore arrays in anodic alumina, Applied Physics Letters, 72 (10), pp. 1173-1175
49. Keller, F., Hunter, M.S., Robinson, D.L., 1953, Structural features of oxide coatings on aluminum, J. Electrochem. Soc, 100, pp. 411-419

50. Kikutani Y., Horiuchi T., Uchiyama K., Hisamoto H., Tokeshi M. and Kitamori T., 2002, Glass microchip with three-dimensional microchannel network for  $2 \times 2$  parallel synthesis, *Lab Chip*, 2, 188
51. Kikutani Y., Horiuchi T., Uchiyama K., Hisamoto H., Tokeshi M. and Kitamori T., 2002, Pile-up glass microreactor, *Lab Chip*, 2, 193
52. Kim J., Jang S.H., Jia G., Zoval J.V., Da Silva N. A. and Madou M.J., 2004, Cell lysis on a microfluidic CD (compact disc) *Lab Chip*, 4, 516
53. Khademhosseini A., Yeh J., Jon S., Eng G., Suh K.Y., Burdick J.A. and Langer R., 2004, Molded polyethylene glycol microstructures for capturing cells within microfluidic channels, *Lab Chip*, 4, 425
54. Lagally E.T., Emrich C.A. and Mathies R.A., 2001, Fully integrated PCR-capillary electrophoresis microsystem for DNA analysis, *Lab Chip*, 1, 102
55. Lee, S.B., Mitchell, D.T., Trofin, L., Nevanen, T.K., Söderlund, H., Martin, C.R., 2002, Antibody-based bio-nanotube membranes for enantiomeric drug separations, *Science*, 296 (5576), pp. 2198-2200
56. Lee, W., Jin, M.-K., Yoo, W.-C., Lee, J.-K., 2004, Nanostructuring of a polymeric substrate with well-defined nanometer-scale topography and tailored surface wettability, *Langmuir*, 20 (18), pp. 7665-7669.
57. Lee, W., Ji, R., Gösele, U., Nielsch, K., 2006, Fast fabrication of long-range ordered porous alumina membranes by hard anodization, *Nature Materials*, 5 (9), pp. 741-747

58. Lee, W., Nielsch, K., Gösele, U., 2007, Self-ordering behavior of nanoporous anodic aluminum oxide (AAO) in malonic acid anodization, *Nanotech*, 18 (47), art. no. 475713
59. Lee W. Schwirn K. Steinhart M. Pippel E. Scholz R. Gosele U., 2008, Structural engineering of nanoporous anodic aluminium oxide by pulse anodization of aluminium, *Nature Nanotechnology*. 3(4):234-239
60. Li, A.P., Müller, F., Birner, A., Nielsch, K., Gösele, U., 1998, Hexagonal pore arrays with a 50-420 nm interpore distance formed by self-organization in anodic alumina, *Journal of Applied Physics*, 84 (11), pp. 6023-6026
61. Li, A.-P., Müller, F., Birner, A., Nielsch, K., Gösele, U., 1999, Fabrication and microstructuring of hexagonally ordered two-dimensional nanopore arrays in anodic alumina, *Advanced Materials*, 11 (6), pp. 483-487
62. Li, Y., Zheng, M., Ma, L., Shen, W., 2006, Fabrication of highly ordered nanoporous alumina films by stable high-field anodization, *Nanotechnology*, 17 (20), art. no. 010, pp. 5101-5105
63. Lichtenberger-Bajza, E., Domony, A., Csokán, P., 1960, Untersuchung der Struktur und anderer Eigenschaften von durch anodische Oxydation auf Aluminium erzeugten Hartoxydschichten., *Werkst. u. Korros.*, 11, pp. 701-707
64. Lemoff A.V. and Lee A. P., 2000, An AC magnetohydrodynamic micropump, *Sens. Actuators B* 63, 178
65. Lemoff A.V. and Lee A. P., 2003, An AC Magnetohydrodynamic Microfluidic Switch for Micro Total Analysis Systems, *Biomed. Microdevices*, 5, pp. 55

66. Leventis N. and Gao X. R., 1999, Steady-state voltammetry with stationary disk millielectrodes in magnetic fields: Nonlinear dependence of the mass-transfer limited current on the electron balance of the Faradaic process, *J. Phys. Chem. B*, 103, 5832
67. Macdonald, D.D., 1993, On the formation of voids in anodic oxide films on aluminum, *J. Electrochem. Soc.*, 140, pp. L27-L30
68. Malgorzata A.W., Suying W., Bikas V., Andre A., Li Z., Wieslaw S., Robin L. M. and Soper S. A., 2004, Cell transport via electromigration in polymer-based microfluidic devices, *Lab Chip*, 2004, 4, 464
69. Marcus Y., 1997, Ion properties, (Marcel Dekker Inc., New York)
70. Martin, C.R., 1994, Nanomaterials: A membrane-based synthetic approach, *Science*, 266 (5193), pp. 1961-1966.
71. Masuda, H., Yada, K., Osaka, A., 1998, Self-ordering of cell configuration of anodic porous alumina with large-size pores in phosphoric acid solution, *Japanese Journal of Applied Physics, Part 2: Letters*, 37 (11 PART A), pp. L1340-L1342
72. Masuda, H., Fukuda, K., 1995, Ordered metal nanohole arrays made by a two-step replication of honeycomb structures of anodic alumina, *Science*, 268 (5216), pp. 1466-1468
73. Masuda, H., Hasegawa, F., Ono, S., 1997, Self-ordering of cell arrangement of anodic porous alumina formed in sulfuric acid solution, *Journal of the Electrochemical Society*, 144 (5), pp. L127-L130
74. Mathaba T., Mpholo M., Sebitia S., Bau H.H., 2006, Magnetohydrodynamic Fluid Flow Simulation Tool, 2006 International Conference on Micro and Nano Technologies, ICMNT06, Tizi-Ouzou, Algeria

75. Mei, Y.F., Wu, X.L., Shao, X.F., Huang, G.S., Siu, G.G., 2003, Formation mechanism of alumina nanotube array, *Physics Letters, Section A: General, Atomic and Solid State Physics*, 309 (1-2), pp. 109-113
76. Murphy, J.F., Michelson, C.E., 1961, *Anodizing Aluminum Proceedings*, 83. Aluminum Development Association, Nottingham
77. Natarajan N. and Lakshmanan S.M., 1972, Laminar flow in rectangular ducts: prediction of velocity profiles and friction factor," *Indian J. Technology*, 10, 435
78. Newman J., 1991, *Electrochemical Systems*, 2nd ed. (Prentice-Hall, Englewood Cliffs, NJ)
79. Nicewarner-Peña, S.R., Freeman, R.G., Reiss, B.D., He, L., Peña, D.J., Walton, I.D., Cromer, R., Natan, M.J., 2001, Submicrometer metallic barcodes *Science*, 294 (5540), pp. 137-141
80. Nittis V., Fortt R. , Legge C. H. and de Mello A. J., 2001, A high-pressure interconnect for chemical microsystem applications, *Lab Chip*, 1, 148
81. Ono, Sachiko, Ichinose, Hideki, Masuko, Noboru, 1991, Defects in porous anodic films formed on high purity aluminum, *Journal of the Electrochemical Society*, 138 (12), pp. 3705-3710
82. Ono, Sachiko, Ichinose, Hideki, Masuko, Noboru, 1992, Lattice images of crystalline anodic alumina formed on a ridged aluminum substrate, *Journal of the Electrochemical Society*, 139 (9), pp. 80-81
83. Ono, S., Masuko, N., 1992, The duplex structure of cell walls of porous anodic films formed on aluminum, *Corrosion Science*, 33 (3), pp. 503-505, 507

84. O'Sullivan J.P., Wood G.C., 1970, Morphology and mechanism of formation of porous anodic films on aluminum, *Proc Roy Soc Ser A Math Phys Sci*, 317 (1731), pp. 511-543, 6
85. Ostrowski T. and Rodel J., 1999, Evolution of Mechanical Properties of Porous Alumina during Free Sintering and Hot Processing, *J. Am. Ceram*, 82 [11] 3080-86
86. Parkhutik, V.P., Shershulsky, V.I., 1992, Theoretical modeling of porous oxide growth on aluminum, *J. Phys. D*, 25, pp. 1258-1263
87. Prinz C., Tegenfeldt J. O., Austin R. H., Cox E.C. and Sturm J. C., 2002, Bacterial chromosome extraction and isolation, *Lab Chip*, 2, 207
88. Qian S., Zhu J., and Bau H. H., 2002, A stirrer for magnetohydrodynamically controlled minute fluidic networks, *Phys. Fluids* 14, 3584
89. Qian S. and Bau H. H., 2005, Magnetohydrodynamic stirrer for stationary and moving fluids, *Sens. Actuators B* 106, 859
90. Qian S. and Bau H. H., 2005, Magneto-hydrodynamic flow of RedOx electrolyte, *Phys.Fluids*, 17, 067105
91. Qian S., Chen Z., Wang J., and Bau H. H., 2006, Electrochemical reaction with RedOx electrolyte in toroidal conduits in the presence of natural convection, *Int. J. Heat and Mass Transfer*, 49, 3968
92. Qian S. and Duval J. F. L., 2006, Modulation of electroosmotic flows in electron-conducting microchannels by coupled quasi-reversible faradaic and adsorption-mediated depolarization, *J. Colloid Interface Sci.*, 300, 413

93. Ragsdale S. R., Grant K. M., and White H. S., 1998, Electrochemically generated magnetic forces. Enhanced transport of a paramagnetic redox species in large, nonuniform magnetic fields, *J. Am. Chem. Soc.* 120, 13461
94. Rühle, M.R., Staiger, S., Katerbau, K.H., Wilkens, M., 1976, Electron microscopical contrast of small cavities in metals, 6th European Congress on Electron Microscopy, p. 538
95. Sawaya E., Ghaddar N., and Chaaban F., 2002, Evaluation of the hall parameter of electrolyte solutions in thermosyphonic MHD flow, *Int. J. Eng. Sci.* 40, 2041
96. Schwirn, K., Lee, W., Hillebrand, R., Steinhart, M., Nielsch, K., Gösele, U., 2008, Self-ordered anodic aluminum oxide formed by HSO hard anodization, *ACS Nano*, 2 (2), pp. 302-310
97. Stange M., Dreyer M.E., and Rath H.J., 2003, Capillary driven flow in circular cylindrical tubes, *Physics of Fluids*, 15(9), 2587-2601.
98. Stobbs, W.M., 1979, Electron microscopical techniques for the observation of cavities, *J. Microscopy*, 116, pp. 3-13
99. Stone H.A., Kim S., 2001, Microfluidics: basic issues, applications, and challenges, *AICHE Journal*, 47 (6), 1250-1254
100. Suzuki H., Tabata K., Kato-Yamada Y., Noji H. and Takeuchi S., 2004, Planar lipid bilayer reconstitution with a micro-fluidic system, *Lab Chip*, 4, 502
101. Taylor G., 1953, Dispersion of a soluble matter in solvent flowing slowly through a tube, in *Proceedings of the Royal Society of London Series A — Mathematical and Physical Sciences* 219, 186



102. Terao K., Washizu M. and Oana H., 2008, On-site manipulation of single chromosomal DNA molecules by using optically driven microstructures, *Lab Chip*, 8, 1280
103. Terray A., Oakey J., and Marr D.W.M., 2002, Microfluidic control using colloidal devices, *Science*, 296, 1841-1844
104. Thompson, G.E., Wood, G.C., 1981, Porous anodic film formation on aluminium, *Nature*, 290 (5803), pp. 230-232
105. Tuomikoski S., Huikko K., Grigoras K., Östman P., Kostiainen R., Baumann M., Abian J., Kotiaho T. and Franssila S., Preparation of porous n-type silicon sample plates for desorption/ionization on silicon mass spectrometry (DIOS-MS), *Lab Chip*, 2002, 2, 247
106. Wada, K., Shimohira, T., Yamada, M., Baba, N., 1986, Microstructure of porous anodic oxide films on aluminium, *Journal of Materials Science*, 21 (11), pp. 3810-3816
107. Wang P. J., Chang C. Y., Chang M. L., 2004, Simulation of Two Dimensional Fully Developed Laminar Flow for a Magneto-Hydrodynamic (MHD) Pump, *Biosens. Bioelectron.*, 20, pp. 115
108. West J., Karamata B., Lillis B., Gleeson J.P., Alderman J., Collins J.K., Lane W., Mathewson A., Berney H., 2002, Application of magnetohydrodynamic actuation to continuous flow chemistry, *Lab on a Chip*, 2 (4), 224-230
109. West J., Gleeson J. P., Alderman J., Collins J. K., and Berney H., 2003, Structuring laminar flows using annular magnetohydrodynamic actuation, *Sens. Actuators B* 96, 190

110. Wheeler A.R., Thronset W.R., Whelan R.J., Leach A.M., Zare R.N., Liao Y.H., Farrell K., Manger I.D., Daridon A., 2003, Microfluidic device for single-cell analysis, *Analytical Chemistry*, 75 (14), 3581-3586.
111. White F.M., *Viscous Fluid Flow*, 3rd ed, (McGraw-Hill Companies, Inc., New York, 2006).
112. Woodson H. H. and Melcher J.R., 1969, *Electromechanical Dynamics*, Vol. III (John Wiley, New York)
113. Whitesides G. M., and Stroock A. D., 1998, *Microfluidics*, *Physics Today*, 54, 42-48.
114. Wu Z., Jensen H., Gamby J., Bai X. and Girault H.H., 2004, A flexible sample introduction method for polymer microfluidic chips using a push/pull pressure pump, *Lab Chip*, 4, 512
115. Verpoorte E., 2002, Microfluidic chips for clinical and forensic analysis, *Electrophoresis*, 23 (5), 677-712.
116. Vladimirova N., Malagoli A., Mauri R., 1999, Diffusiophoresis of two-dimensional liquid droplets in a phase-separating system, *Physical Review E*, 60 (2), 2037-2044.
117. Xia Z., Riester L., Sheldon B.W., Curtin W.A., Liang J., Yin A., Xu J.M., 2004, Mechanical Properties of Highly Ordered Nanoporous Anodic Alumina Membranes, *Rev. Mater. Sci*, 131-139
118. Xiang Y. and Bau H. H., 2003, Complex magnetohydrodynamic low-Reynolds-number flows, *Phys. Rev. E* 68, 016312

119. Xie J., Shih J., Lin Q., Yang B. and Tai Y.C. 2004, Surface micromachined electrostatically actuated micro peristaltic pump , Lab Chip, 2004, 4, 495
120. Yamamoto T., Fujii T., and Nojima T., 2002, PDMS-glass hybrid microreactor array with embedded temperature control device. Application to cell-free protein synthesis, Lab Chip, 2, 197
121. Yang J., Liu Y., Rauch C.B. , Stevens R.L., Liu R.H., Lenigk R., and Grodzinski P, 2002, High sensitivity PCR assay in plastic micro reactors, Lab Chip, 2, 179
122. Yi M., Qian S., and Bau H. H., 2002, A magnetohydrodynamic chaotic stirrer, J. Fluid Mech. 468, 153
123. Zhao B., Moore J.S., and Beebe D.J., 2001, Surface-directed liquid flow inside microchannels, Science, 291, 1023-1026.
124. Zhong J.H., Yi M.Q., Bau HH, 2002, Magneto hydrodynamic (MHD) pump fabricated with ceramic tapes, Sensors and Actuators A, 96 (1), 59-66.
125. Zhu X., and Kim E.S., 1998, Microfluidic motion generation with acoustic waves, Sensors and Actuators: A. Physical, 66(1-3), 355-360.
126. Zhu, X.F., Li, D.D., Song, Y., Xiao, Y.H., 2005, The study on oxygen bubbles of anodic alumina based on high purity aluminum, Materials Letters, 59 (24-25), pp. 3160-316

## **VITA**

Graduate College  
University of Nevada, Las Vegas

Hussameddine Kabbani

Local Address:  
POBOX 72102  
Las Vegas, Nevada 89170

Degrees:  
BS, Mechanical Engineering, 2003.  
Beirut Arab University, Beirut, Lebanon.

MS, Mechanical Engineering, 2005.  
American University of Beirut, Beirut, Lebanon.

Thesis Title:  
Magnetohydrodynamics in Microchannels and Adhesion Properties of Nanoporous Alumina Films

Thesis Examination Committee:  
Chairperson, Brendan O'Toole and Dr. Biswajit Das  
Committee Member, Dr. Darrell Pepper  
Committee Member, Dr. William Culbreth  
Graduate Faculty Representative, Dr. Aly Said